Collisions entre électrons et molécules: Mécanismes réactionnels, modèles théoriques et applications aux plasmas hors-équilibre

Vincenzo Laporta

Normandie Université

MÉMOIRE

pour obtenir
l'Habilitation à Diriger les Recherches

Spécialité: Physique moléculaire, physique des plasmas

COLLISIONS ENTRE ÉLECTRONS ET MOLÉCULES: MÉCANISMES RÉACTIONNELS, MODÈLES THÉORIQUES ET APPLICATIONS AUX PLASMAS HORS-ÉQUILIBRE

Présentée et soutenue par
Vincenzo LAPORTA

Thèse soutenue publiquement le 11/12/2017 devant le jury composé de		
M. Arnaud BULTEL	Maître de Conférences HDR, Université de Rouen (France)	Rapporteur
M. Olivier DULIEU	Directeur de Recherche, Université Paris-Sud 11 (France)	Rapporteur
M. Xavier URBAIN	Professeur, Université Catholique de Louvain (Belgique)	Rapporteur
M. Philippe TEULET	Professeur, Université Paul Sabatier Toulouse 3 (France)	Examinateur
M. Stéphane PELLERIN	Professeur, Université d'Orléans (France)	Examinateur
M. Jonathan TENNYSON	Professeur, University College London (Royaume-uni)	Examinateur
M. Roberto CELIBERTO	Professeur, Politecnico di Bari (Italie)	Examinateur
M. Ioan F. SCHNEIDER	Professeur, Université du Havre (France)	Examinateur

UNIVERSITÉ LE HAVRE

LABORATOIRE ONDES et MILIEUX COMPLEXES

Labex
Laboratoire d'Excellence
EMC³
ENERGY MATERIALS & CLEAN COMBUSTION CENTER

CNRS

UCL

Contents

Avant-propos

Le "fil rouge" qui a caractérisé la plupart de ma carrière scientifique a été la détermination des sections efficaces. Le calcul et la mesure d'une section efficace permettent de connaitre en détail la dynamique d'un processus de collision ou de désintégration (dans ce cas on parle, plus proprement, de vitesse de désintégration qui, en fait, est un cas particulier de section efficace) et, en même temps, d'analyser les forces qui gouvernent le processus, et donc tester une théorie physique. C'est pour cela que le concept de section efficaces est central dans toute la physique des processus microscopiques.

Ma première activité scientifique, correspondant au doctorat et à la première position post-doc, a été consacrée à la phénoménologie de la physique des particules élémentaires. Mon travail a été le calcul des sections efficaces pour les collisions et les désintégrations des mésons lourds, en particulier du méson B et de la résonance J/ψ, dans le cadre des théories des champs efficaces quantiques de la Chromo-Dynamique Quantique (QCD) en utilisant la théorie des perturbations chirales (χPT) et la Théorie Effective des Quarks Lourds (HQET). Le but de ces recherches a été la validation des prédictions du Modèle Standard pour les désintégrations du méson B en deux mésons légers et pour la suppression de la J/ψ dans le plasma des quarks et gluons (QGP). J'ai menée ces recherchers au Dipartimento di Fisica de l'Université de Bari (Italie) en collaboration avec l'Istituto Nazionale di Fisica Nucleare (INFN, Italie), l'Institut de Physique Nucléaire de Lyon de l'Université Claude Bernard Lyon-1 (France), la division théorique du CERN (Genève, Suisse) et le Centre de PHysique Théorique (CPHT) de l'Ecole Polytechnique (Palaiseau, France).

J'ai fait ensuite "un petit saut" dans la physique de la matière condensée. Au Département de physique de l'Université de Bari (Italie), j'ai étudié les propriétés électriques d'un détecteur de rayonnement ultraviolet basé sur un film mince de diamant artificiel, créé en utilisant la technique du Chemical-Vapor-Deposition (CVD). Ma tâche principale a été le développement d'un code Monte Carlo 0-D et 1-D pour la simulation de la cascade d'électrons-trous par absorption de photons dans le réseau du diamant et pour la détermination de l'efficacité quantique du capteur. La simulation a fourni le nombre moyen de paires électron-trou et le nombre de phonons en fonction de l'énergie photonique incidente. En outre, le code a été formulé afin d'obtenir le signal électrique de sortie du capteur qui tient compte de la dérive, de la diffusion et de la taille finie des grains du film de diamant.

Lors des dernières années je me suis dédié à la physique des plasmas moléculaire hors-équilibre, qui sera le principal object du présent mémoire. Mon apport dans les recherches sur les plasmas hors-équilibre peut être divisé en deux branches. Dans la première, je me suis concentré sur les études théoriques des processus élémentaires résolus état-à-état pour les collisions à impact électronique impliquant des molécules et des ions excités vibrationnellement et rotationellement. En particulier, mon travail consiste à calculer les sections efficaces et les coefficients de vitesse correspondants pour l'excitation vibrationnelle, l'attachement dissociatif électronique, la recombinaison dissociative et les processus d'excitation dissociative. On appelle cela communément la caractérisation dynamique des plasmas, qui consiste à étudier les interactions entre les constituants du plasma. Les résultats sont obtenus en utilisant les codes de chimie quantique *ab initio* MOLPRO et UK-R-Matrix, dans les approches théoriques du modèle de potentiel complexe local de Bardsley, l'approximation nucléaire adiabatique et la théorie du défaut quantique. J'ai conduit ces recherches auprès du DICATECh du Politecnico di Bari (Italie) où j'ai travaillé avec le Prof. R. Celiberto, du Département de physique et d'astronomie de University College London (Royaume-Uni) où j'ai collaboré avec le Prof. J. Tennyson et au Laboratoire Ondes et Milieux Complexes, Université du Havre (France) avec le Prof. I. Schneider. Cette partie concerne les Chapitres 2 et 3.

Le deuxième aspect concerne l'étude des modèles cinétiques collisionnels-radiatifs où les propriétés thermiques des plasmas hors-équilibre sont étudiées dans le cadre de l'approche dite "état-par-état" (state-to-state, StS). Ces contributions sont contenues dans le Chapitre 4. L'approche StS prend en compte, pour chaque espèce chimique, les degrés internes de liberté (vibrations, rotation, mouvement électronique ...) et sont considérés comme décrivant des espèces indépendantes. Pour cette raison, les approches de StS sont les seuls modèles qui offrent la possibilité d'accéder à l'échange d'énergie entre les degrés de liberté interne du système et d'obtenir des informations détaillées, y compris des fonctions de distribution affectant la thermodynamique, les coefficients de transport, les temps de relaxation et la cinétique. Dans la dynamique collisionnelle, l'équation de Boltzmann est résolue pour les électrons constamment auto-couplés aux espèces chimiques (atomes, ions, molécules) reproduisant des caractéristiques très intéressantes de distributions internes fortement hors-équilibre caractérisant les plasmas. Dans ce contexte, les sections efficaces que j'ai calculées pour la dynamique moléculaire représentent les données d'entrée pour les modèles cinétiques. Pour cet aspect j'ai profité de la collaboration, en Italie, avec l'equipe du Prof. M. Capitelli au sein du CNR-Nanotec (Bari, Italie) en particulier avec le Dr. G. Colonna. Aux États-Unis, j'ai collaboré avec Prof. R. Jaffe du Centre de recherche AMES de la NASA (Moffett Field (CA)) et avec le Dr. M. Panesi du Département d'ingénièrie aérospatiale de l'Université d'Illinois (Champaign (IL)) où j'ai étudié les modèles d'échange d'énergie électron-rovibration dans le cadre StS pour les flux contenant de l'azote et de l'oxygène pour le problème de la rentrée des navettes spatiales dans l'atmosphère des planètes.

Sur cet aspect à Ohio Aerospace Institute et Wright-Patterson Air Force Base (Dayton (OH)), en collaboration avec Dr. E. Josyula, j'ai étudié des modèles cinétiques zéro- et uni-dimensionnels pour les flux hypersoniques contenant de l'oxygène dans les applications aérospatiales.

Le présente mémoire recueille la plupart de travaux que j'ai publié et des notes que j'ai pris pendant ces années d'une façon le plus possible homogène.

V.L.
Le Havre, 2017

Remerciements

Mes sincères remerciements vont aux personnes qui m'ont suivi pendant ma carrière scientifique et qui ont permis l'avancement de mes études. Merci pour le support scientifique et humaine à Gianpiero Colonna, Jonathan Tennyson, Marco Panesi, Alessandro Munafò et Ioan Schneider. Un remerciement particulier va à Mario Capitelli et Roberto Celiberto qui m'ont introduit dans la physique des plasmas moléculaires en 2010. Une pensée va à Beppe Nardulli qui a été mon directeur de thèse de doctorat et auquel je dois plusieurs enseignements.

Enfin, des remerciements vont à ma famille et en particulier à ma mère.

Chapter 1

Introduction

My present researches are concentred in modelling of non-equilibrium molecular plasmas physics, the so-called 'cold plasmas' [1, 2, 3]. Generally speaking, plasmas are made of ionized gases which contain equal amounts of positive and negative electric charges so that the global charge is null. As a matter of the fact plasmas have their own characteristics, they are often considered the fourth state of matter. Positive charges are carried by positive ions. Negative charges are usually supplied by electrons but in some cases negative ions can have a non-negligible contribution. Plasmas are broadly classified into two classes. One is high-temperature, fully ionized plasma. The other is low-temperature and weakly ionized one. Most regions of the Universe are in a state of plasma. Stellar atmosphere, for example, is a kind of high-density and high-temperature plasmas (> 1000 K). On the opposite side, interstellar space is filled with very-low density matter ($10^2 - 10^4$ particles cm^{-3}) and low temperature ($10 - 100$ K). The degree of ionization is very low ($\sim 10^{-8}$), but the charged particles still play a significant role.

Looking for molecular plasmas, one of the typical examples existing in Nature is the ionosphere on the Earth [4] and other planets. In the ionosphere, atoms and molecules are ionized mainly by the UV or X-ray solar radiation. Early Universe was made of molecular plasma [5]. On the other hand, in recent decades, the interest in molecular plasmas for a wide range of industrial and technological applications is growing up. They range goes from the chemistry for the hypersonic flows in aerospace [6, 7, 8] to plasma assistant combustion [9], controlled fusion [10, 11], and medical diagnostic techniques [12, 13] just to name a few.

From thermodynamics point of view plasmas are distinguished between 'thermal' and 'cold plasmas'. The first class is characterized by local-thermodynamic-equilibrium, the second class by non-equilibrium between the different degrees of freedom of the system, including the internal (*e.g.* vibration and rotation for molecules; electronic excited states for atoms and molecules) and chemical (*i.e.* reactions between different of same species take place) ones. The characterization of non-equilibrium plasmas is very difficult and it can be
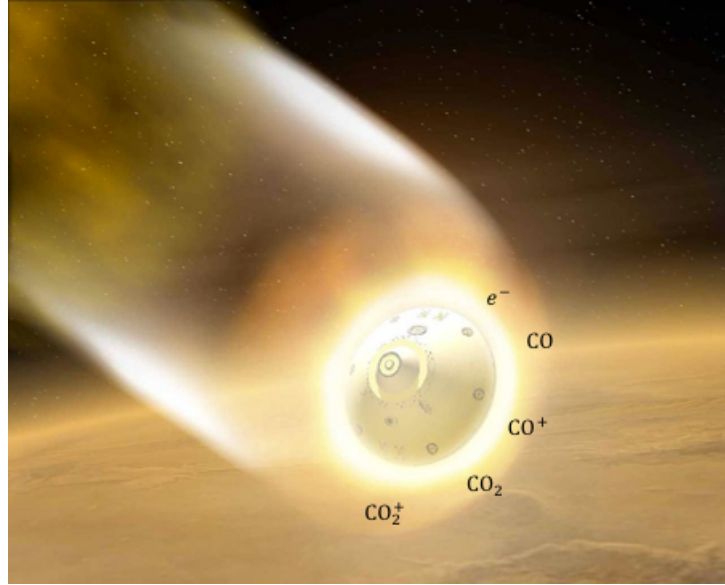
Figure 1.1: Artistic representation of a shuttle, surrounded by a plasma shock wave, entering a planetary atmosphere.

performed using more or less sophisticated approaches, depending on the particular process under investigation, commonly based on statistical thermodynamics, fluid-dynamics, kinetic theory and quantum chemistry. In order to clarify how these disciplines enter in the modelling, an example concerning the atmospheric plasma for re-entry shuttles is discussed. A subject I worked on, in the last years.

When a spacecraft enters the atmosphere of a planet at speeds exceeding the local speed of sound, a shock wave is formed behind it and its kinetic energy is transformed into heat (Fig. 1.1). The ablation effects, caused by the energy transfer on the side walls of the shuttle, are shown in Fig. 1.2. The energy delivered to the gas in this process promotes excitation of the molecular internal degrees of freedom (rotational, vibrational, electronic) and chemical reactions (including dissociation and ionization). The hot reacting (and radiating) gas is often in thermal and chemical non-equilibrium conditions and it is this complex system that interacts with the vehicle surface.

Advanced models mean the description of the non-equilibrium chemical kinetics of the high temperature medium on the basis of a state-to-state (StS) approach, a methodology originally developed to explain chemical reactions in low-temperature, non-equilibrium plasmas [14]. The StS approach decomposes any degree of freedom of the molecule in internal levels (vibrational, rotational, electronic) and each level is considered as an independent species described by an appropriate continuity equation and its own cross sections and
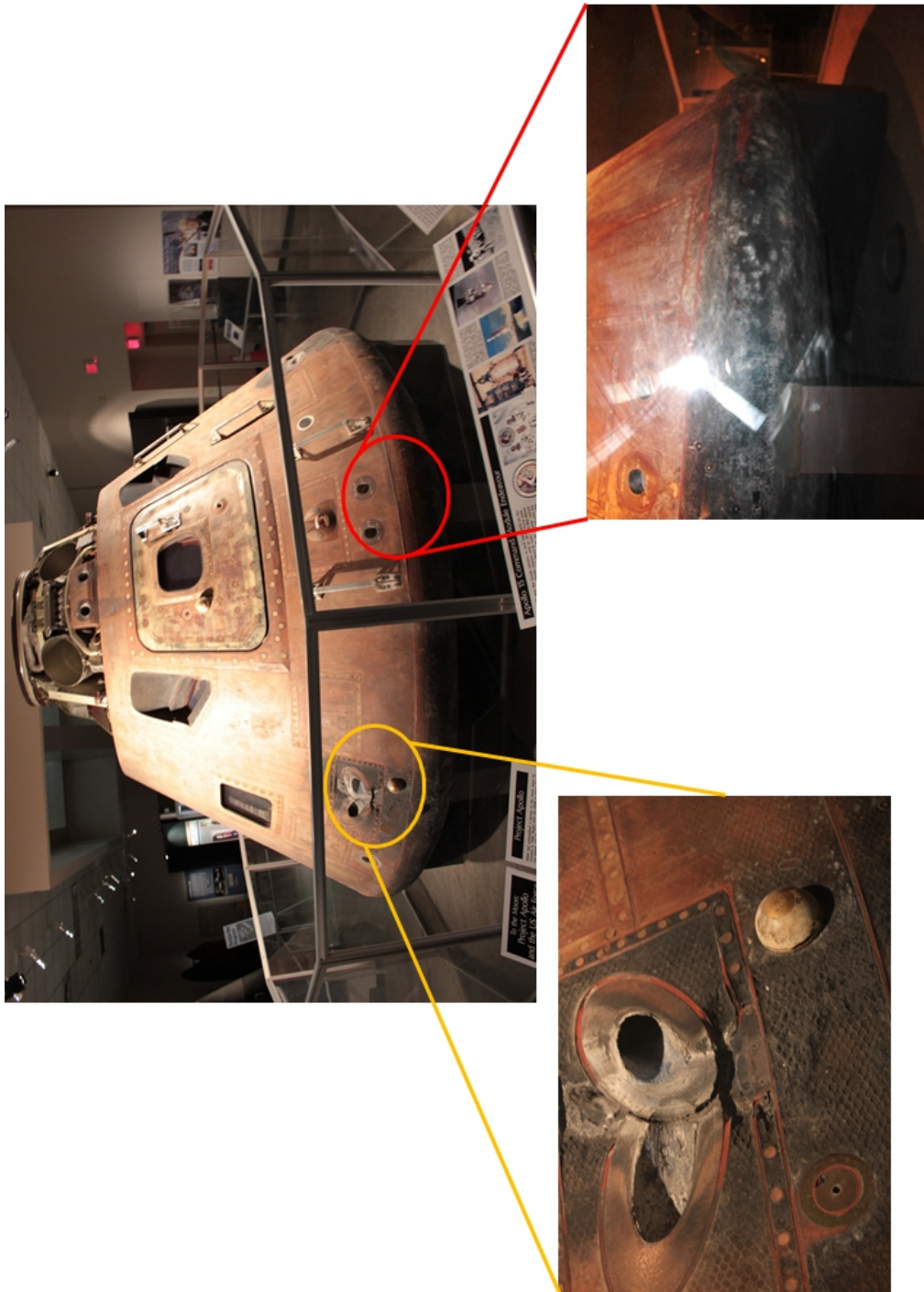
9

Figure 1.2: Effect of atmospheric re-entry plasma ablation on a real shuttle. National Museum of the United States Air Force (Wright-Patterson AFB and NASA, Dayton (OH), 2015).

rate constants. From the level distributions, the thermal properties of the gas and global rate coefficients can be calculated and they can be very different from those obtained by a thermal equilibrium or weak non-equilibrium (linear response) analysis.

Therefore, any serious modeling attempt should start from a reliable database of state-selected cross sections for the elementary processes involved. This set of data will then be used in the development of theoretically sound kinetic models to be validated through dedicated experiments. Only then, the models can be used reliably in Computational Fluid Dynamics (CFD) simulations of realistic systems [15].

The first objective of the study is to assess the status of the cross section databases for use in hypersonics and to update, revise or complete it with the help of *ab initio* molecular dynamic calculations. It is worth recalling at this stage that existing databases refer to processes involving ground state species. In this context instead, we are explicitly interested in processes involving excited (mainly vibrational and rotational) states. In particular, free electrons are very active radicals so that also very small concentrations ($\sim 10^{-6}$) can promote energy exchanges, dissociation and ionization reactions.

Chapter 2

Theoretical methods for electron-molecule scattering

The phenomenology of molecule and molecular ion scattering by electron-impact is very rich and include a large class of processes. In this work, we will take into account the following processes:

$$e + AB(v) \rightarrow AB(w) + e \qquad \text{VIBRATIONAL EXCITATION (VE/VdE)} \qquad (2.1)$$
$$e + AB^+(v) \rightarrow AB^+(w) + e$$

$$e + AB(v) \rightarrow A + B^- \qquad \text{DISSOCIATIVE ATTACHMENT (DA)} \qquad (2.2)$$
$$\rightarrow A^- + B$$

$$e + AB^+(v) \rightarrow A + B \qquad \text{DISSOCIATIVE RECOMBINATION (DR)} \qquad (2.3)$$

$$e + AB(v) \rightarrow A + B + e \qquad \text{DISSOCIATIVE EXCITATION (DE)} \qquad (2.4)$$
$$e + AB^+(v) \rightarrow A + B^+ + e$$
$$\rightarrow A^+ + B + e$$
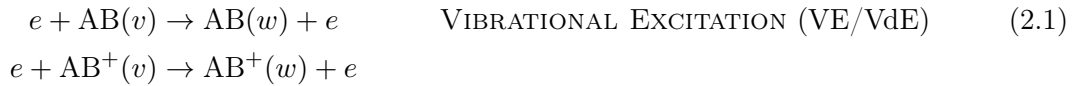
where v and w represent vibrational levels belonging to the same molecular electronic state. Direct processes are, in general, an inefficient processes because of the small electron-to-molecule mass ratio as well as the lack, particulary for homonuclear molecules, of electric dipole moment for interaction. However, it has been well established that in the energy range in which the incident electron can attach to form a temporary intermediate state, cross section can be enhanced by orders of magnitude [16]. These processes are called

resonant collisions, and schematically can be represent as:

$$e + \mathrm{AB} \rightarrow \mathrm{AB}^* \rightarrow \text{final state} \ldots, \tag{2.5}$$

where AB^* represents the resonant stare. Theoretical and experimental reviews on this subject can be found in the Refs. [17, 18, 19] and references therein. The processes involving neutral molecules $\mathrm{AB}(v)$ proceed through the resonant state $\mathrm{AB}^{-(*)}$ and through the resonant states AB^{**} and excited Rydberg states for the case of positive ions $\mathrm{AB}^+(v)$.

VE processes or 'inelastic' collisions occur for $w > v$ and, in this kind of collisions, energetically speaking, some of the incident electron energy is transferred to the internal degree of freedom of the molecule or ion. The inverse process, that is for $w < v$, is called vibrational de-excitation (VdE) or 'super-elastic' scattering and, in this case, energy is released from the internal energy of molecule to the environment. The pure elastic scattering take place when $v = w$ with no energy exchange. As a matter of the fact VE and VdE processes allow transitions between states belonging to the discrete part of molecular spectra they are of fundamental importance in studying energy transfer balance in non-equilibrium plasmas and, in particular, in understanding how the energy is stocked in internal degree of freedoms of molecules. The effect of Electron-vibration coupling will be considered in Chapter 4 for nitrogen-containing plasmas.

Processes of DA, with his inverse associative detachment (AD), and DR, with his inverse associative ionization (AI), allow conversion of molecules into atomic species with a global change in the number of free electrons of a unit. On the other hand, the processes of DE, which are particular case of excitation processes from the discrete part involving the continuum part of spectrum the of the molecule, are able to convert molecular species into atomic species without changing the global number of the free electrons.

In the following sections the theoretical methods used in the Chapter 3 to calculate molecular cross sections for the processes in (2.1)–(2.4) are discussed.

2.1   Projection-operators formalism for resonant scattering

In this section some mathematical details about the theoretical formalism for the resonant scattering of molecules by electron-impact at low energy are revisited. In particular, we will consider neutral molecules but the framework is still valid, with some extensions, also for cations. In Section 2.2 the Multichannel Quantum Defect Theory for molecular ions will be introduced.

Here we focus on basic features of the projection-operators formalism (POF). This approach is needs to build up the *nonlocal-complex-potential* theory for the electron–molecule scattering, in its full formulation and *local* approximation. Some more theoretical details on this topic can be found in the papers [16, 20, 21, 22] and references therein. At low energies the cross section is dominated by negative ion resonances [23, 24] contributions, that is the
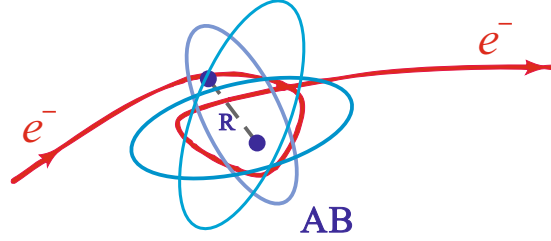
Figure 2.1: Electron–molecule resonant collision.

incident electron is temporarily captured by the molecule and a negative intermediate state occurs, then the resonant state decays into a new state, in general different with respect to the initial one. Schematically the process is shown in Fig. 2.1.

Mathematically, in POF the electron–molecule resonance scattering process is described by two type of vector states: the discrete electronic state $|d\rangle$, that describe the 'bound' resonant state, *embedded-in* and *interacting-with* an electronic continuum states $|\vec{k}\rangle$, that describe the non-resonant background, the interaction of electron and neutral molecule. Although resonant states are temporary, their lifetimes are often long on the atomic scale. In these cases the resonant wave function will be very nearly that of a bound state. We can define the projectors operators within the Hilbert space according to:

$$P = \int d\vec{k}\, |\vec{k}\rangle\langle\vec{k}|\,, \qquad\qquad Q = |d\rangle\langle d|\,, \qquad\qquad (2.6)$$

with the standard properties of completeness and orthogonality:

$$P + Q = 1\,, \qquad P^2 = P\,, \qquad Q^2 = Q\,, \qquad PQ = QP = 0\,. \qquad (2.7)$$

The total effective Hamiltonian $\mathcal{H}$ for resonant electron–molecule interaction can be written as:

$$\mathcal{H} = \mathcal{H}_0 + \mathcal{V}\,, \qquad (2.8)$$

with $\mathcal{H}_0$ describing the 'free' bound and continuum states, $\mathcal{V}$ their mutual interaction:

$$\mathcal{H}_0 = |d\rangle\,(T_N + V_0 + \epsilon_d)\,\langle d| + \int d\vec{k}\, |\vec{k}\rangle\,(T_N + V_0 + \epsilon)\,\langle\vec{k}|\,, \qquad (2.9)$$

$$\mathcal{V} = \int d\vec{k}\,|d\rangle V_{dk}\langle\vec{k}| + \text{h.c.}\,. \qquad (2.10)$$

In the previous equations: $T_N(R)$ represents the nuclear kinetic energy operator,

$$T_N = -\frac{\hbar^2}{2\,\mu}\frac{d^2}{dR^2}\,, \qquad (2.11)$$

14

where μ the reduced mass of target molecule; $V_0(R)$ the potential electronic energy of the neutral target state of the molecule including the centrifugal barrier potential,

$$V_J = \frac{J(J+1)\hbar^2}{2\mu R^2}\,,\tag{2.12}$$

with J the angular momentum; $\epsilon_d(R)$ is the resonance position respect to the neutral molecule; $\epsilon = \hbar^2 k^2/(2m_e)$ is the (continuum) electron energy and V_{dk} the matrix element which mixes the discrete electronic state $|d\rangle$ with the continuum state $|\vec{k}\rangle$, namely:

$$V_{dk} = \langle d|\mathcal{H}|\vec{k}\rangle\,.\tag{2.13}$$

R represents the molecular internuclear distance. Assuming that the Born-Oppenheimer approximation is valid, the electronic wave function is a slowly varying quantity with the parameter R and this implies that the projectors P and Q commute with the nuclear kinetic energy operator, *i.e.*,

$$[P, T_N] = [Q, T_N] = 0\,.\tag{2.14}$$

The global vector state of the system $|\psi\rangle$ satisfies the Schrodinger equation:

$$(\mathcal{H} - E)|\psi\rangle = 0\,,\tag{2.15}$$

where E is the total energy. By using the completeness property of project operators it can be slitted into two parts:

$$|\psi\rangle = P|\psi\rangle + Q|\psi\rangle\,.\tag{2.16}$$

The 'open-channel' component $P|\psi\rangle$ has the same asymptotic form of $|\psi\rangle$. It has, in fact, an outgoing-wave component which describes an electron escaping to infinity and it behaves as a product of a wave function of the target molecule and of a free electron. The 'closed-channel' component $Q|\psi\rangle$ vanishes asymptotically for large electron separation. In this view, $P|\psi\rangle$ is linked to the non-resonant background scattering while $Q|\psi\rangle$ is associated to the resonant collision. The coupled inhomogeneous equations satisfied by $P|\psi\rangle$ and $Q|\psi\rangle$ are obtained by substituting Eq.(2.16) into Eq.(2.8) and then projecting into P and Q space:

$$P(\mathcal{H}_0 - E)P|\psi\rangle = -P\mathcal{V}Q|\psi\rangle\,,\tag{2.17}$$
$$Q(\mathcal{H}_0 - E)Q|\psi\rangle = -Q\mathcal{V}P|\psi\rangle\,,\tag{2.18}$$

where the Born-Oppenheimer approximation, Eq.(2.14), and the following properties have been used:

$$P\mathcal{V}P = Q\mathcal{V}Q = Q\mathcal{H}_0 P = P\mathcal{H}_0 Q = 0\,.\tag{2.19}$$

The formal solution of the open-channel equation in (2.17) can be written in a Lippmann–Swinger-like form:

$$P|\psi\rangle = |\epsilon\rangle \otimes |v_i\rangle + \frac{1}{P(E - \mathcal{H}_0)P}P\mathcal{V}Q|\psi\rangle\,,\tag{2.20}$$

where $|\epsilon\rangle \otimes |v_i\rangle$ represents, asymptotically, a free electron with energy ϵ incident on the target molecule in vibrational level v_i and $E = \epsilon + v_i = \frac{k^2}{2m_e} + v_i$ is the total energy of the system. As we are interested to describe the bound state solution of the system, by putting the solution in Eq.(2.20) into closed-channel Eq.(2.18), after some manipulations, we arrive to the following integro-differential equation for the so-called nuclear wave function $\xi(R)$:

$$\left(T_N + V_0 + \epsilon_d - E\right)\xi(R) + \int dR' \, \mathcal{K}(R, R', E)\, \xi(R') = -V_{dk}^*(\epsilon, R)\, \chi_i(R)\,. \tag{2.21}$$

This is the fundamental equation governing the motion of the nuclei in the resonant anion state. In Eq.(2.21),

$$\chi_i(R) = \langle R|v_i\rangle\,, \tag{2.22}$$

and it is eigenfunction of the neutral molecule potential V_0:

$$(T_N + V_0)\,\chi_n = v_n\,\chi_n\,. \tag{2.23}$$

The complex, non-local and energy-dependent kernel $\mathcal{K}(R, R', E)$ is written as:

$$\mathcal{K}(R, R', E) = \sum_n \left[\Delta(R, R', E - v_n) - \frac{i}{2}\Gamma(R, R', E - v_n)\right]\chi_n^*(R')\chi_n(R)\,, \tag{2.24}$$

in term of the non-local and energy-dependent width and level shift operator, given respectively by:

$$\Gamma(R, R', E - v_n) = 2\pi\, V_{dk}(E - v_n, R)V_{dk}^*(E - v_n, R')\,, \tag{2.25}$$

and

$$\Delta(R, R', E - v_n) = \mathcal{P}\int d\epsilon'\,\frac{V_{dk}(\epsilon', R)V_{dk}^*(\epsilon', R')}{E - v_n - \epsilon'}\,, \tag{2.26}$$

where $\mathcal{P}$ denotes the Cauchy principal value of the integral. The only assumption made in deriving these results, apart the restriction to a single discrete electronic state, is that the electronic states $|d\rangle$ and $|\vec{k}\rangle$ are diabatic, *i.e.* weakly dependent on the vibrational coordinate R.

Usually, the computational effort to solve the full non-local theory is very tedious, caused by the energy dependence of the kernel, and the usual practice is to work in the local approximation, *i.e.* the so-called 'boomerang model'. This is the case when the incident electron energy ϵ is large compared with the spacing of the vibrational levels v_n of the neutral molecule, that is,

$$|v_n - v_m| \ll \epsilon\,, \qquad \forall n, m\,, \tag{2.27}$$

and it becomes reasonable to make the following replacement in Eq.(2.24):

$$E - v_n = \epsilon + v_i - v_n \approx \epsilon\,. \tag{2.28}$$

Moreover, if we are in the neighborhood of the resonance region we can make the local electron energy *ansatz*, that is:

$$\epsilon = \frac{k^2}{2m_e} \approx \epsilon_d(R) \,. \tag{2.29}$$

With the approximations state in Eqq.(2.28) and (2.29), the non-local kernel $\mathcal{K}$ in Eq.(2.24) becomes a local function of R and energy independent:

$$\mathcal{K}(R, R', \epsilon) = \left[\Delta(R, \epsilon) - \frac{i}{2}\Gamma(R, \epsilon)\right] \delta(R, R') \,, \tag{2.30}$$

and for the width we have,

$$\Gamma(R) = 2\pi \left|V_{dk}(R, \epsilon_d(R))\right|^2 \,. \tag{2.31}$$

In the local version of the theory, the level shift operator Δ in Eq.(2.26) diverges and it is not possible to compute the corresponding local operator. It becomes an external phenomenological parameter, sometime included in the real part of the anion potential. Therefore, in the local approximation, the resonant nuclear wave function $\xi(R)$ satisfies an ordinary differential equation:

$$\boxed{\left(T_N + V^- - \frac{i}{2}\Gamma - E\right)\xi(R) = -V_{dk}^*(\epsilon, R)\,\chi_i(R) \,,} \tag{2.32}$$

where we have set $V^- = V_0 + \epsilon_d$, the real part of the anion potential.

By using the theory presented here, the cross section for vibrational excitation process in (2.1) is given by:

$$\sigma_{v_i \to v_f}(\epsilon) = \frac{2S_r + 1}{2(2S + 1)}\frac{g_r}{g}\frac{64\,\pi^5\,m_e^2}{\hbar^4}\frac{k_f}{k_i}\left|\langle\chi_f|V_{dk}(\epsilon')|\xi\rangle\right|^2 \,, \tag{2.33}$$

where: g and g_r are the degeneration factors for the potentials of neutral and anionic states respectively; $2(2S + 1)$ and $2S_r + 1$ are the number of polarization states for the incident (electron and neutral molecule) and resonant state respectively; $k_{i(f)}$ is the incoming (outgoing) electron momenta given by Eq.(2.29); $\xi(R)$ is the solution of the nuclear wave equation of the negative ion in Eq.(2.21) or in Eq.(2.32); χ_f is the eigenfunction for the final vibrational level v_f in Eq.(2.23).

For dissociative attachment and dissociative recombination processes in (2.2) and (2.3) the corresponding cross section is given by [21]:

$$\sigma_v(\epsilon) = \frac{2S_r + 1}{2(2S + 1)}\frac{g_r}{g}\,2\,\pi^2\,\frac{m_e}{k}\frac{K}{\mu}\lim_{R \to \infty}\left|\xi_v(R)\right|^2 \,, \tag{2.34}$$

where K is the asymptotic momentum $(R \to \infty)$ of the dissociating atomic fragments with reduced mass μ and k is the incoming electron momentum.

Analogously to the VE processes, dissociative excitation (2.4) cross section is given by:

$$\sigma_v(\epsilon) = \frac{2S_r + 1}{2(2S + 1)} \frac{g_r}{g} \, 4 \, \pi^3 \int d\epsilon' \, \frac{1}{k^2} \, |\langle \chi_{\epsilon'} | V_{dk} | \xi_v \rangle|^2 \,, \tag{2.35}$$

where $\chi_{\epsilon'}$ is the continuum wave function of the molecule with energy ϵ' representing the free atoms and an electron. The integration is extended over all the continuum state of the molecule.

The differential cross section is linked to integral cross section by,

$$\frac{d\sigma(\epsilon)}{d\Omega} = g_l(\Omega) \, \sigma(\epsilon) \,, \tag{2.36}$$

where $g_l(\Omega)$ is a energy-independent angular function corresponding to l-partial wave [22].

A part the molecular vibrations also the rotational levels can be taken into account in the theory. By assuming a Boltzmann distribution for the rotational levels at temperature T_r, the j-averaged energy of vibrational level v can be computed as:

$$\bar{\epsilon}_v(T_r) = \sum_{j=0}^{j_{max}} \epsilon_{v,j} \, (2j + 1) \, \frac{e^{-\epsilon_{v,j}/k_B T_r}}{Q_v(T_r)} \,, \tag{2.37}$$

where $\epsilon_{v,j}$ is the energy of ro-vibrational level (v, j) and Q_v is the partition function of the system. Analogously, the j-averaged cross section as a function of the rotational temperature is given by:

$$\bar{\sigma}_v(\epsilon, T_r) = \sum_{j=0}^{j_{max}} \sigma_{v,j}(\epsilon) \, (2j + 1) \, \frac{e^{-\epsilon_{v,j}/k_B T_r}}{Q_v(T_r)} \,, \tag{2.38}$$

where $\sigma_{v,j}(\epsilon)$ represents a generic ro-vibrational specific cross section.

Finally, by assuming a Maxwellian distribution for the electrons the rate coefficient K for a given cross section $\sigma(\epsilon)$ can be expressed, as a function of the electron temperature T_e, as:

$$\begin{aligned} K(T_e) &= \langle \sigma \, v \rangle \\ &= \int \sigma(\epsilon) f(\epsilon, T_e) \sqrt{\frac{2\epsilon}{m_e}} \, d\epsilon \\ &= \left(\frac{1}{m_e \pi} \right)^{1/2} \left(\frac{2}{k_B T_e} \right)^{3/2} \int \epsilon \, \sigma(\epsilon) \, e^{-\epsilon/k_B T_e} \, d\epsilon \,, \end{aligned} \tag{2.39}$$

where $f(\epsilon, T_e)$ is the Maxwell distribution of velocity and k_B is the Maxwell-Boltzmann constant.

Up to now, forward reaction in (2.1)–(2.4) have been considered. By assuming the principle of microscopic reversibility, at equilibrium, the corresponding backward processes can be determined by detailed balance.

2.1.1 Green function solution of $\xi(R)$

The main difficulty in calculating the cross section of a process is to determine the solution of the resonant wave function $\xi(R)$ in Eq.(2.21) or in Eq.(2.32). The wave function $\xi(R)$ can be found by direct resolution using numerical technique (*e.g.* Numerov's method) and imposing *ad-hoc* correct bound limit. It is possible to use another more analytic method by using the Green function technique. In this approach, the starting point is to consider the homogeneous associated equation of the Eq. (2.32), with the Green function $G(E; R, R')$ satisfying the equation:

$$\left(T_N + V^- - \frac{i}{2}\Gamma - E\right) G(E; R, R') = \delta(R - R'),$$
(2.40)

so that the final solution $\xi(R)$ can be written as:

$$\xi(R) = -\int dR' \, G(E; R, R') \, V_{dk}^*(R') \, \chi_i(R').$$
(2.41)

Considering the whole set of eigenfunctions ψ_n, discrete and continuous, of the resonant potential V^-,

$$\left(T_N + V^-\right)\psi_n = \bar{v}_n \, \psi_n,$$
(2.42)

(the continuous part of the spectrum has been discretized) they form a complete system of eigenfunctions and it is possible to expand the Green function in term of the ψ_n:

$$G(E; R, R') = \sum_n c_n(E, R') \, \psi_n(R).$$
(2.43)

By putting the Green expansion in Eq. (2.43) into Eq. (2.40) and after some manipulations it is possible to arrive to the following expression for the coefficient c_n:

$$
\begin{aligned}
c_n(E, R') &= \sum_m \left[(\bar{v}_n - E)\delta_{nm} - \frac{i}{2}\Gamma_{nm}\right]^{-1} \psi_m(R'), \\
&= \sum_m \mathcal{M}_{nm}^{-1}(E) \, \psi_m(R'),
\end{aligned}
$$
(2.44)

where it has been defined the matrix element of the operator $\hat{\Gamma}$ between two resonant eigenstates,

$$\Gamma_{nm} = \int dR \, \psi_n(R) \, \hat{\Gamma}(R) \, \psi_m(R).$$
(2.45)

The Green function can be written as:

$$G(E; R, R') = \sum_{n,m} \mathcal{M}_{nm}^{-1}(E)\psi_n(R')\psi_m(R).$$
(2.46)

The resonant wave function $\xi(R)$ is therefore given by:

$$\xi(R) = -\sum_{n,m} \mathcal{M}_{nm}^{-1}(E)\, I_n^i\, \psi_m(R)\,, \qquad (2.47)$$

where has been introduced the Frank–Condon-like integral between the resonant and neutral eigenstates with the coupling potential V_{dk},

$$I_b^a = \int dR\; \psi_b(R)\, V_{dk}(R)\, \chi_a(R)\,. \qquad (2.48)$$

Finally, the cross section can be written, apart the kinetic and statistical factors, as:

$$\begin{aligned} \sigma_{if}(\epsilon) \;\; &\propto \;\; \left| \int dR\, \xi(R)\, V_f(R)\, \chi_f(R) \right|^2 \\ &= \;\; \left| \sum_{n,m} \mathcal{M}_{nm}^{-1}(\epsilon + v_i)\, I_n^i\, I_m^f \right|^2 . \end{aligned} \qquad (2.49)$$

2.2 Multichannel Quantum Defect Theory

In order to include the molecular ions in the theoretical framework presented in Section 2.1, it is needed to introduce the Multichannel quantum Defect theory (MQDT). The processes (2.1), (2.3) and (2.4) with the ion AB^+ result from the coupling between ionization and dissociation channels, *i.e.* groups of states characterized by a common set of quantum numbers and by the same fragmentation threshold (either for ionization or for dissociation), having the energy below or above this threshold. More specifically, within a *quasi-diabatic* representation [25, 26, 27], an *ionization* channel is built starting from the ground electronic state of the ion in one of its vibrational levels v^+, and is completed by gathering all the mono-electronic states of a given orbital quantum number l, describing an 'optical' electron. These mono-electronic states describe, with respect to the v^+ threshold, either a 'free' electron - in which case the total electronic state corresponds to (auto)ionization - or to a bound one - in which case the electronic state AB^* corresponds to a temporary capture into a Rydberg state. Meanwhile, a dissociation channel relies on an electronically bound state AB^{**} whose potential energy in the asymptotic limit is situated below the total energy of the system. Given the total energy of the molecular system, a channel is *open* if this energy is higher than the energy of its fragmentation threshold, and *closed* in the opposite case. Relying exclusively on the open channels means accounting for the *direct* mechanism. The inclusion of the closed channels allows for the *indirect* mechanism, which interferes with the direct one resulting in the *total* process.

The MQDT approach starts with the building of the interaction matrix $\boldsymbol{\mathcal{V}}$, performed in the so-called 'A-region' [28], where the Born-Oppenheimer context is appropriate for

the description of the collision system. The good quantum numbers in this region are N, M, and Λ, associated respectively to the total angular momentum and its projections on the z-axis of the laboratory-fixed and of the molecule-fixed frames. In the A-region, the states belonging to an ionization channel may be modeled reasonably well with respect to hydrogenic states, in terms of the quantum defect μ_l^Λ, which is dependent on the internuclear distance R, but assumed to be independent of energy. An ionization channel is coupled to a dissociation one, labeled d_j, on *electronic* level first, through an R-dependent scaled 'Rydberg-valence' interaction term, $V_{d_j,l}^{(e)\Lambda}$, which is assumed to be independent of the energy of the electronic states pertaining to the ionization channel.

Integrating this coupling over the internuclear distance gives elements of the interaction matrix $\boldsymbol{\mathcal{V}}$:

$$\mathcal{V}_{d_j,lN^+v^+}^{NM\Lambda}(E,E) = \langle \chi_{Nd_j}^\Lambda | V_{d_j,l}^{(e)\Lambda} | \chi_{N^+,v^+}^\Lambda \rangle\,, \tag{2.50}$$

where E is the total energy and $\chi_{d_j}^\Lambda$ and χ_{N^+,v^+}^Λ are the nuclear wave-functions corresponding to a dissociative state and to an ionization channel, respectively. This procedure applies in each Λ-subspace, and results in a block-diagonal global interaction matrix.

Starting from the interaction matrix $\boldsymbol{\mathcal{V}}$ and from the zero-order Hamiltonian H_0, we build the reaction $\boldsymbol{\mathcal{K}}$-matrix, which satisfies the Lippmann-Schwinger equation [29]:

$$\mathcal{K} = \mathcal{V} + \mathcal{V}\frac{1}{E-H_0}\mathcal{K}\,. \tag{2.51}$$

In order to express the result of the short-range interaction in terms of phase-shifts, we perform a unitary transformation of our initial basis into a new one, corresponding to eigenchannels, *via* the diagonalization of the reaction matrix $\boldsymbol{\mathcal{K}}$:

$$\mathcal{K}\mathbf{U} = -\frac{1}{\pi}\tan(\eta)\mathbf{U}\,. \tag{2.52}$$

In the external 'B-region' [28], characterized by large electron-core distances, the Born-Oppenheimer model is no longer valid for the neutral molecule and Λ is no longer a good quantum number, and a frame transformation [24, 30, 31] is performed, *via* the projection coefficients:

$$
\begin{aligned}
\mathcal{C}_{lN^+v^+,\Lambda\alpha} &= \left(\frac{2N^++1}{2N+1}\right)^{1/2}\langle l\left(\Lambda-\Lambda^+\right)N^+\Lambda^+|lN^+N\Lambda\rangle\frac{1+\tau^+\tau\,(-1)^{N-l-N^+}}{\left[2\left(2-\delta_{\Lambda^+,0}\right)\left(1+\delta_{\Lambda^+,0}\delta_{\Lambda,0}\right)\right]^{1/2}} \\
&\quad\times \sum_v U_{lv,\alpha}^\Lambda\langle\chi_{N^+v^+}^{\Lambda^+}|\cos(\pi\mu_l^\Lambda(R)+\eta_\alpha^\Lambda)|\chi_{Nv}^\Lambda\rangle\,, \tag{2.53}
\end{aligned}
$$

$$\mathcal{C}_{d_j,\Lambda\alpha} = U_{d_j\alpha}^\Lambda\cos\eta_\alpha^\Lambda\,, \tag{2.54}$$

which can be represented by matrix $\boldsymbol{\mathcal{C}}$. The other solutions, represented by matrix $\boldsymbol{\mathcal{S}}$, are obtained as $\mathcal{S}_{lN^+v^+,\Lambda\alpha}$ and $\mathcal{S}_{d_j,\Lambda\alpha}$ by replacing cosine with sine in Eqs. (2.53) and (2.54). In the equations, χ_{Nv}^Λ is the vibrational wavefunction of the neutral system in the interaction

(A) region. The quantities τ^+ and τ are related to the reflection symmetry of the ion and neutral wave function respectively, and take the values $+1/-1$ for symmetric/antisymmetric states respectively.

Matrices $\mathcal{C}$ and $\mathcal{S}$ are the building blocks of the generalized scattering matrix $\boldsymbol{X}$, involving all the channels, open ('o') and closed ('c'), and organized in 4 sub-matrices:

$$\boldsymbol{X} = \frac{\mathcal{C} + i\mathcal{S}}{\mathcal{C} - i\mathcal{S}}, \qquad \boldsymbol{X} = \begin{pmatrix} X_{oo} & X_{oc} \\ X_{co} & X_{cc} \end{pmatrix}, \tag{2.55}$$

Imposing boundary conditions leads to the physical scattering matrix [32]:

$$\boxed{\boldsymbol{S} = \boldsymbol{X}_{oo} - \boldsymbol{X}_{oc} \frac{1}{\boldsymbol{X}_{cc} - \exp(-\mathrm{i}2\pi\boldsymbol{\nu})} \boldsymbol{X}_{co}\,,} \tag{2.56}$$

where the diagonal matrix $\boldsymbol{\nu}$ is formed with the effective quantum numbers (in atomic units),

$$\nu_{N^+ v^+} = [2(E_{N^+ v^+} - E)]^{-1/2}\,, \tag{2.57}$$

associated with each vibrational threshold $E_{N^+ v^+}$ of the ion situated above the energy E (and consequently labelling a *closed* channel).

For a molecular ion initially on the level $N_i^+ v_i^+$ recombining with an electron of energy ε, the cross section of capture into all the dissociative states d_j of the same symmetry can be written:

$$\sigma^{N,sym}_{diss \longleftarrow N_i^+ v_i^+}(\varepsilon) = \frac{\pi}{4\varepsilon} \frac{2N+1}{2N_i^+ + 1} \rho^{sym} \sum_{l,\Lambda,j} |S^{N\Lambda}_{d_j, l N_i^+ v_i^+}|^2\,, \tag{2.58}$$

Here ρ^{sym} is the ratio between the multiplicities of the neutral and the target ion.

2.3 R-matrix method

Basically, in the resonant electron-molecule scattering theories presented in Section 2.1 and 2.2 the main physical quantities request by the model are represented by the potential energy curves, couplings for the resonances and quantum defects for the Rydberg states. There are many approach to calculated those quantities. In my works I used the R-matrix method [33] implemented in the UKRMat quantum chemistry code [34]. In a fixed-nuclei approach, R-matrix calculates the electron-molecule scattering amplitude from which is possible to determine the molecular data request from the resonant theory.

The main facet of the R-matrix method is the division of configurational space into an inner and an outer region. The inner region is defined as the volume of a sphere of radius a centered at the center-of-mass of the target molecule. This region is constructed so that the wave functions of all N except the scattering electron vanish at boundary of the sphere. In this region the exchange effects, *i.e.* the short range electron-electron correlations and

polarization effects, are important. Implicitly this method assumes that the Pauli principle, which asserts that all inner region electrons are identical and any electron wave function must be anti-symmetric to interchange of these electrons. In the outer region it is assumed that one electron can be considered to be distinct. This electron therefore moves in a local potential arising from its long-range interaction with the target. The exchange effects are neglected in this region. The construction of matrix R provides the link between the inner and outer region. The R-matrix method has some distinct advantages. The main one is that the inner region problem needs to be solved only once. The energy dependence is obtained entirely from the solution of the much simpler outer region case. This allows us to generate solutions at a large number of energies at a minimal extra computational effort. This generates cross sections on a fine energy grid that helps in analyzing the nature of resonances that may arise.

In the inner region the total wave function is expanded in a configuration-interaction (CI) basis which takes the following form for each total orbital angular momentum, spin and parity combination:

$$\Psi_k^{N+1} = \mathcal{A} \sum_{i,j} \Phi_i^N(\mathbf{x}_1 \ldots \mathbf{x}_N)\, \xi_j(\mathbf{x}_{N+1})\, a_{ijk} \ + \ \sum_m \chi_m(\mathbf{x}_1 \ldots \mathbf{x}_{N+1})\, b_{mk}\,, \qquad (2.59)$$

where $\mathcal{A}$ is an anti-symmetrization operator, $\mathbf{x}_N$ are the spatial and spin coordinates of the N-th electron, Φ_i^N is the wave function of the i-th target state, ξ_j are the continuum orbitals of the scattering electron, k represents a particular R-matrix basis function. The variational coefficients a_{ijk} and b_{mk} are determined by matrix diagonalization. Furthermore the electrons, whose space-spin coordinates are represent by $\mathbf{x}_i$, must obey the Pauli principle and are therefore anti-symmetrized by operator $\mathcal{A}$. In practical implementations for generating the configurations which make up this term it is often necessary to impose a constraint on the coupling of the first N electrons to ensure that the target wave function does not get contaminated by states with the same configuration but different space-spin symmetry. The second summation involves configurations which have no amplitude on the R-matrix boundary and where all electrons are placed in orbitals associated with the target. Since they are confined to a finite volume of space they will be referred to as L^2 configurations. Such configurations are essential to relax the constraint in the orthogonalization between the continuum orbitals and those belonging to the target of the same symmetry. In more sophisticated models the L^2 configurations are also used to model the effects of target polarization. The remaining information that is required to set-up the outer region problem concerns properties of the target. The target state energies relative to the ground state are needed as they give the energies of the asymptotic channels. The multipole moments associated with these target states are also required as they determine the outer region.

2.4 Adiabatic-Nuclei approximation

The Adiabatic Nuclei (AN) approximation is well-known in scattering theory and the interested reader can refer to the rich literature on the subject [35, 36] for details. We will only recall here the main aspects of its formulation for diatomic molecules and state the relevant equations useful for the next discussion.

The AN in its standard treatment, is based on the decoupling of the nuclear and electronic motion, so that the total scattering wave function can be approximated by the product of the electronic wave function in the fixed-nuclei approximation, *i.e.* parametrically dependent on the internuclear distance R, and the nuclear ro-vibrational wave function. This factorization is based on the assumption that the speed of the target and incident electrons is much higher than that of the nuclei, so that an electronic transitions take place in a very short time, during which the nuclei remain still at a given internuclear distance.

The cross section from the initial state $|i\rangle$ to the final state $|f\rangle$ is given by:

$$\sigma_{i \to f}(\epsilon) = \frac{\pi}{k^2} \sum_{S,\Lambda,l,l'} g_s \left| \left\langle f \left| T_{l,l'}^{\Lambda,S}(R;k) \right| i \right\rangle \right|^2 , \qquad (2.60)$$

where ϵ is the incident electron energy and k its momentum. $T_{l,l'}^{\Lambda,S}(R;k)$ is the R-depending T-matrix expressed in terms of the l, l' partial wave quantum numbers, Λ is the group symmetry index and S is the spin state quantum number of the global electron-molecule system. g_S is a spin multiplicity factor, given as $(2S + 1)/2(2S_i + 1)$, where $2(2S_i + 1)$ is the initial total spin. The T-matrix is calculated by the R-matrix method for some values of the internuclear distance R and for an extended range of energies.

Chapter 3

Cross sections calculations and database

In this chapter, the molecular data set I produced for plasma kinetic modeling application are collected. They are classified by molecular species and include potential energy curves, vibrational levels, cross sections and rate coefficients. Full computational details are not reproduced here; for that one is referring to the original papers. The list of the considered chemical processes are summarized in Table 3.1.

#	Process	Reference
1	$e + N_2(X\,^1\Sigma_g^+, v) \rightarrow N_2(X\,^1\Sigma_g^+, v') + e$	[37, 38]
2	$e + N_2(X\,^1\Sigma_g^+, v) \rightarrow N(^4S) + N(^4S) + e$	[39]
3	$e + NO(X\,^2\Pi, v) \rightarrow NO(X\,^2\Pi, v') + e$	[37]
4	$e + O_2(X\,^3\Sigma_g^-, v) \rightarrow O_2(X\,^3\Sigma_g^-, v') + e$	[40]
5	$e + O_2(X\,^3\Sigma_g^-, v) \rightarrow O(^3P) + O^-(^2P)$	[41, 42]
6	$e + O_2(X\,^3\Sigma_g^-, v) \rightarrow O(^3P) + O(^3P) + e$	[41, 42]
7	$e + CO(X\,^1\Sigma^+, v) \rightarrow CO(X\,^1\Sigma^+, v') + e$	[43]
8	$e + CO(X\,^1\Sigma^+, v) \rightarrow C(^3P) + O^-(^2P)$	[44]
9	$e + CO(X\,^1\Sigma^+, v) \rightarrow C(^3P) + O(^3P) + e$	[44]
10	$e + CO_2(X\,^1\Sigma_g^+, v) \rightarrow CO_2(X\,^1\Sigma_g^+, v') + e$	[45]
11	$e + He_2^+(X\,^2\Sigma_u^+, v) \rightarrow He + He^+ + e$	[46]
12	$e + BeH^+(X\,^1\Sigma^+, v) \rightarrow BeH^+(X\,^1\Sigma^+, v') + e$	[47]
13	$e + BeH^+(X\,^1\Sigma^+, v) \rightarrow Be^* + H(^2S)$	[47]
14	$e + BeH^+(X\,^1\Sigma^+, v) \rightarrow Be^+(^2S) + H(^2S) + e$	[47]

Table 3.1: List of the processes considered in the manuscript.

3.1 N_2

In this section, the electron-impact collisions involving ground state of N_2 molecules are reported. In particular, are discussed the processes of vibrational and dissociative excitation, respectively labeled, in Table 3.1, as processes 1 and 2, and occurring through the resonant state $N_2^-(X\,^2\Pi_g)$. Nitrogen molecule plays a role of fundamental importance in many scientific and industrial activities. Typical examples are provided by air plasmas studied in a variety of fields such as environmental research, Earth's atmosphere phenomena, combustion, and aerospace technologies [7, 48, 49, 50]. Detailed chemical aspect of the processes involving molecular nitrogen have been studied in the papers [51, 52, 53].

The first measurements for electron–nitrogen vibrational excitation scattering was performed by Schulz [54, 55]; followed by numerous experimental investigations [56, 57, 58, 59, 60, 61, 62, 63] and theoretical calculations [22, 57, 64, 65, 66, 67, 68, 69]. A completed collection of experimental data can be found in the review of Itikawa [70]. However, despite the broad production of cross sections data, especially for nitrogen, all the previous works are restricted to excitations between the first few vibrational levels. This circumstance is particularly limiting for models of those plasma systems in which strong non-equilibrium conditions exist.

Electron-N_2 scattering calculations were performed using the R-matrix method as implemented in the UKRMol codes [34]. The boundary sphere was set to 10 a_0. Target calculations used the cc-pVQZ Gaussian Type Orbital (GTO) basis set due to Dunning. Orbitals for the N_2 target where generated using multi-configuration self-consistent field (MCSCF) calculations run in MOLPRO [71]. The CAS used in MOLPRO calculations and to define also the target wave function in the R-matrix implementation is given by:

$$(1\sigma_{\mathrm{g}}, 1\sigma_{\mathrm{u}})^4 (2\sigma_g, 2\sigma_u, 1\pi_u, 3\sigma_g, 1\pi_g, 3\sigma_u)^{10}\,.$$

A total of 128 target states were generated (eight per symmetry) of which the lowest 49 in energy were retained for the inner region. Calculations were performed for a 100 geometries from 0.8 Å to 3.77 Å in steps of 0.03 Å.

For the scattering calculations, the following target orbitals

$$(4\sigma_g, 5\sigma_g, 4\sigma_u, 2\pi_u, 2\pi_g, 1\delta_g)\,,$$

were retained. These were augmented by continuum orbital containing up to g ($l = 4$) functions represented by a GTO expansion at the target center-of-mass [72]. These were orthogonalized to the target orbitals with a deletion threshold set to 10^{-7} [73]. The target times continuum configurations were augmented by the following short-range functions based on the use of target orbitals:

$$(1\sigma_{\mathrm{g}}, 1\sigma_{\mathrm{u}})^4 (2\sigma_g, 2\sigma_u, 1\pi_u, 3\sigma_g, 1\pi_g, 3\sigma_u)^{11}\,,$$
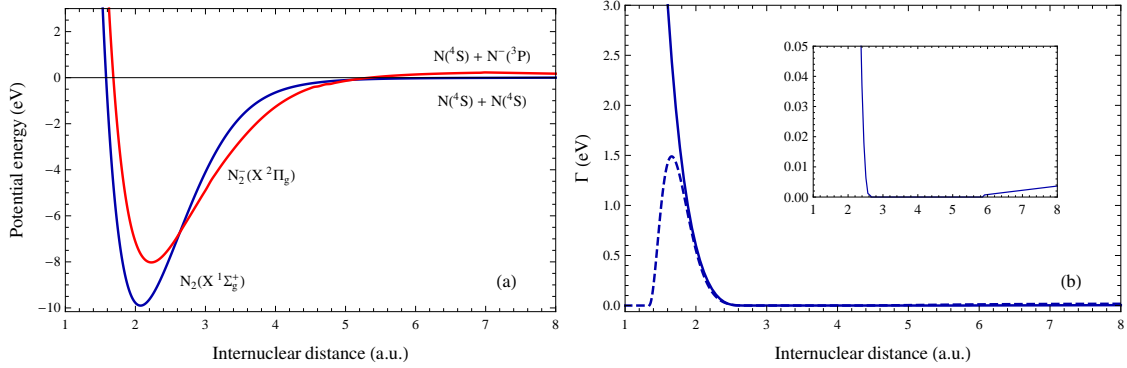
Figure 3.1: (a) Potential energy curves for $N_2(X\ ^1\Sigma_g^+)$ and $N_2^-(X\ ^2\Pi_g)$ and (b) resonance width $\Gamma(R)$ as a function of the internuclear distance: solid line, this work; dashed line, phenomenological width. The inset plot shows a magnified view of our resonance width ($\Gamma(R) \leq 0.05$ eV).

which involves placing the scattering electron in the target CAS, and

$$(1\sigma_{\mathrm{g}}, 1\sigma_{\mathrm{u}})^4 (2\sigma_g, 2\sigma_u, 1\pi_u, 3\sigma_g, 1\pi_g, 3\sigma_u)^{10} (2\pi_u, 4\sigma_g, 5\sigma_g, 2\pi_g, 1\delta_g, 4\sigma_u)^1 \, ,$$

where the scattering electron enters and otherwise unoccupied target virtual. These configurations were not constrained by contracting to target CI wave functions [74].

The $N_2(X\ ^1\Sigma_g^+)$ potential energy curve is taken from Le Roy *et al.* [75] who obtained it by an accurate fit to the spectroscopic data. The resulting potential curves for both N_2 and N_2^-, along with the corresponding width $\Gamma(R)$, are shown in Fig. 3.1(a)-(b) respectively. The $N_2^-(X\ ^2\Pi_g)$ resonance curve crosses $N_2(X\ ^1\Sigma_g^+)$ at $\sim 2.657\ a_0$ and $\sim 5.132\ a_0$. In the intermediate region the molecular ion N_2^- becomes stable and the resonance width vanishes, as is shown in the inset box in Fig. 3.1(b). For geometries where N_2^- is bound, the position of the bound state was determined using the same model and by performing negative energy scattering calculations [76]. Table 3.2 contains the list of vibrational levels of N_2 for $J = 0$.

The cross sections were calculated in the framework of local-complex-potential theory presented in the Section 2.1. In order to validate the results, plots in the Figures 3.2, 3.3, 3.4, 3.5 contain the comparison with experimental measurements. Figures 3.6 and 3.7 summarize the state-resolved cross sections for vibrational excitation and dissociation respectively. The peaks present in the cross sections refer to the resonant vibrational states of N_2^-. The effect of the rotation are included in the Figures 3.8 and 3.9.

v	ϵ_v (eV)	v	ϵ_v (eV)	v	ϵ_v (eV)	v	ϵ_v (eV)
0	0.000	15	3.959	30	7.084	45	9.163
1	0.288	16	4.195	31	7.260	46	9.252
2	0.573	17	4.426	32	7.430	47	9.335
3	0.855	18	4.654	33	7.596	48	9.409
4	1.133	19	4.878	34	7.757	49	9.476
5	1.408	20	5.099	35	7.913	50	9.535
6	1.679	21	5.315	36	8.064	51	9.587
7	1.947	22	5.528	37	8.210	52	9.631
8	2.211	23	5.737	38	8.350	53	9.667
9	2.471	24	5.942	39	8.485	54	9.696
10	2.728	25	6.143	40	8.614	55	9.717
11	2.982	26	6.339	41	8.737	56	9.732
12	3.232	27	6.532	42	8.853	57	9.742
13	3.478	28	6.721	43	8.963	58	9.748
14	3.720	29	6.905	44	9.067		

Table 3.2: Vibrational levels given by the N$_2$ potential energy curve [75] counted from the lowest level $v = 0$, which has a zero-point energy of 0.146 eV.
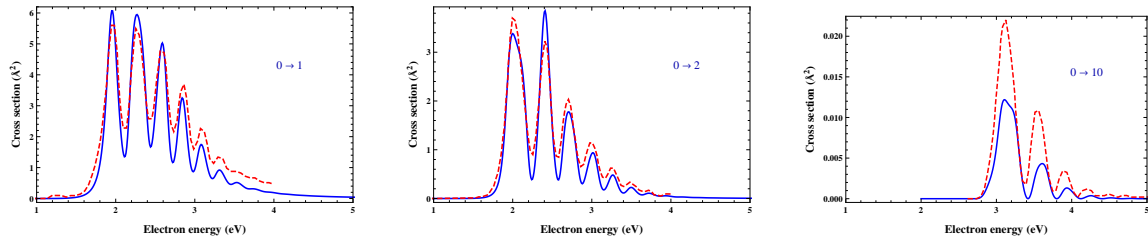
Figure 3.2: Cross section comparison between the present calculations (full-blue line) and the measurements (dashed-red line) of Ref. [60]. The experimental data have an estimated uncertainty of $\pm 20\%$.
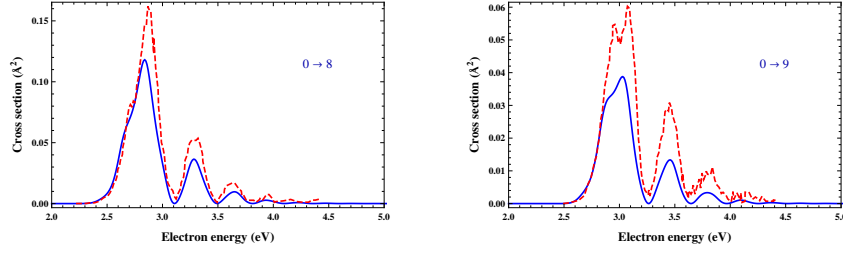
29

Figure 3.3: Cross section comparison between the present calculations (full-blue line) and the measurements of Vićić *et al.* [56].
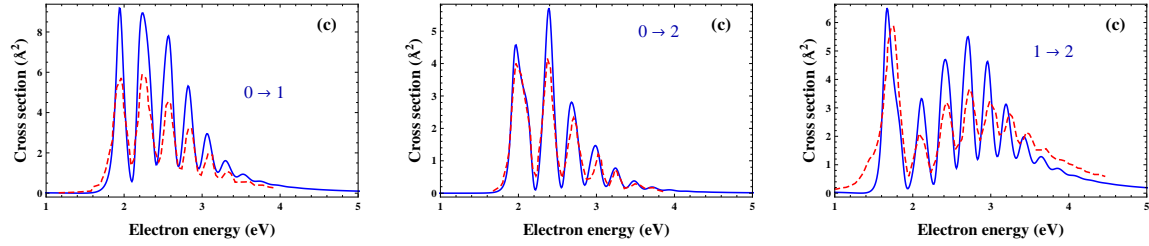

Figure 3.4: Calculated electron–N_2 resonant cross sections (solid line) compared with Wong experimental data (full circle) as cited in Ref. [22].
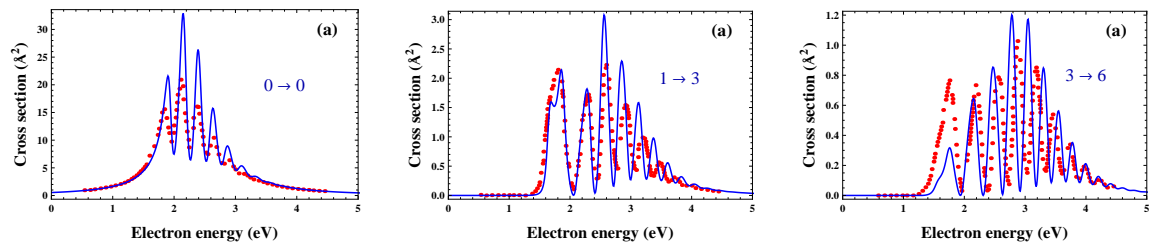

Figure 3.5: Calculated electron–N_2 resonant cross section (solid line) compared with the results of Dubé and Herzenberg [22] (full circle).
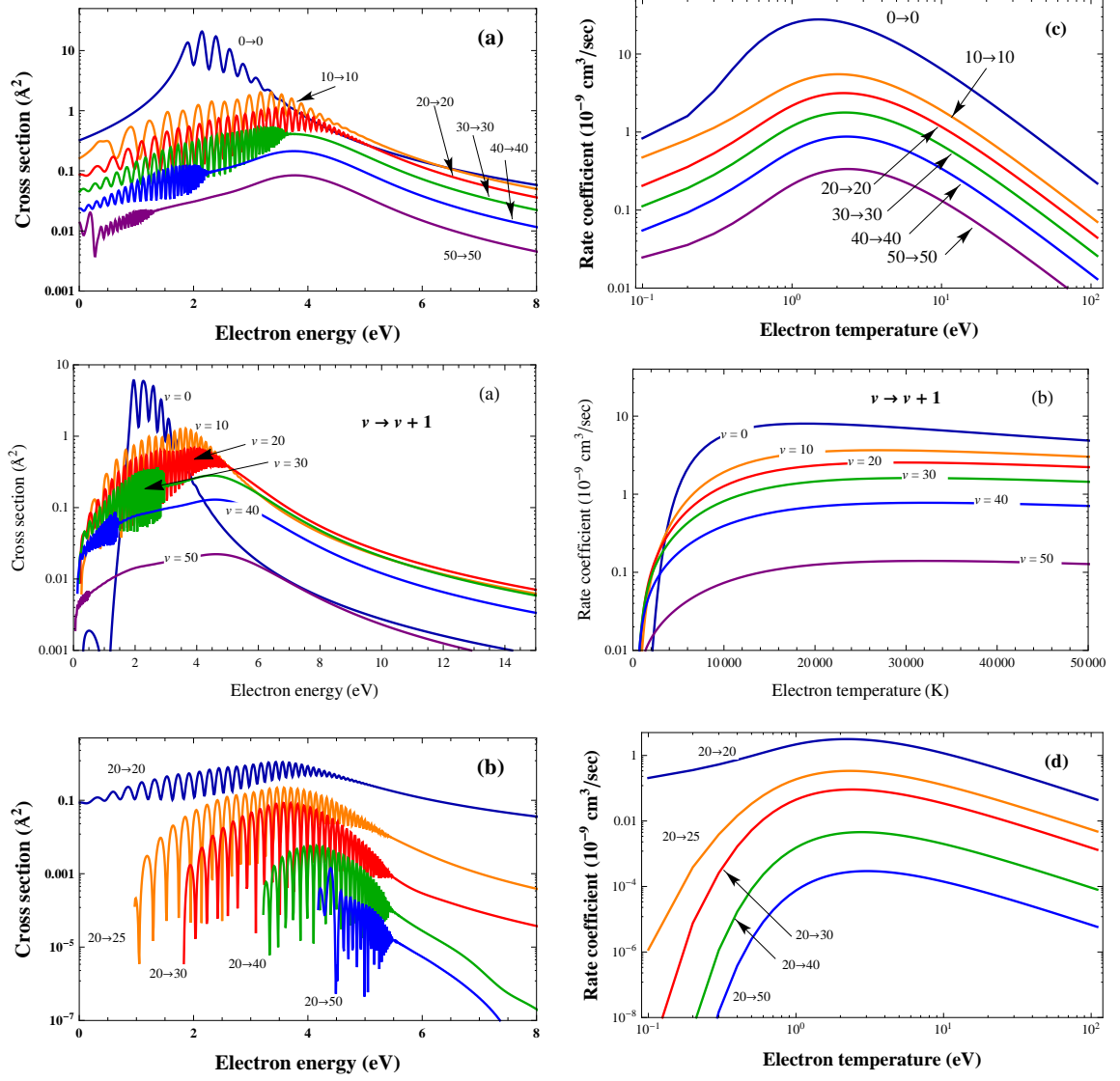
Figure 3.6: Summary of calculated electron–N$_2$ state-to-state resonant cross sections (left side) and the corresponding rate coefficients (right side) for the vibrational excitations indicated in the panels.
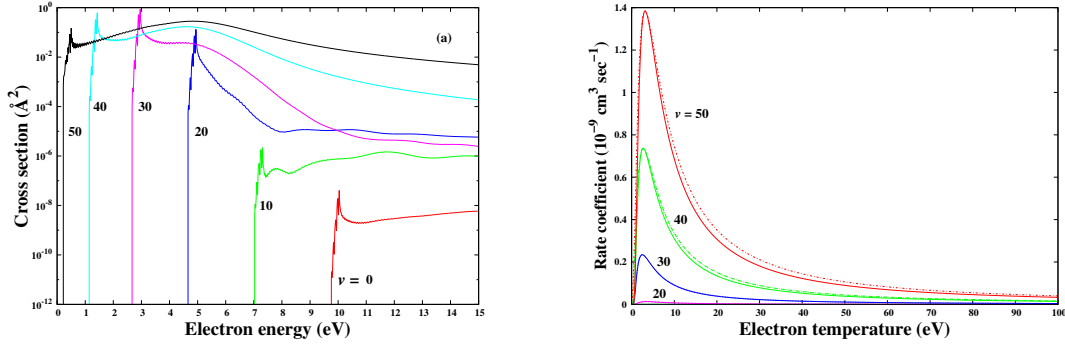
Figure 3.7: Resonant electron-N_2 dissociative excitation cross sections for some initial vibrational levels.
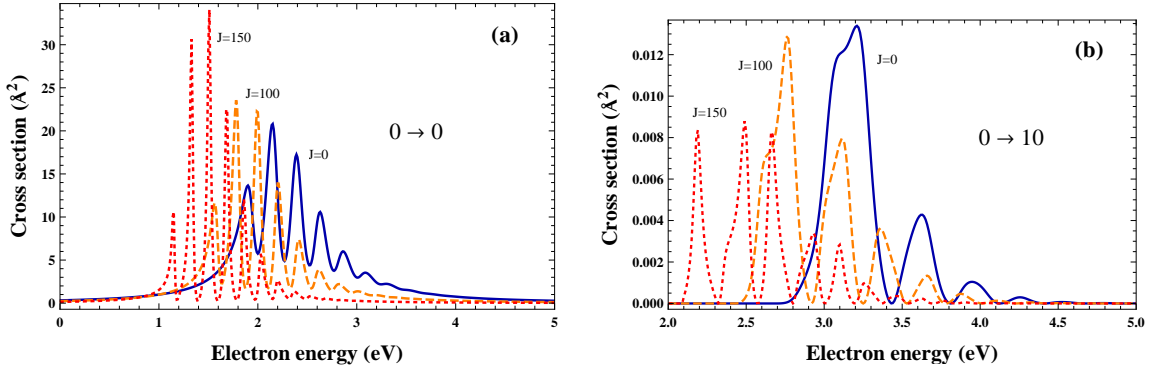

Figure 3.8: Effect of rotation on electron–N_2 resonant VE cross sections calculated for different initial J: $J = 0$ (solid line), $J = 50$ (dashed line) and $J = 150$ (dotted line).
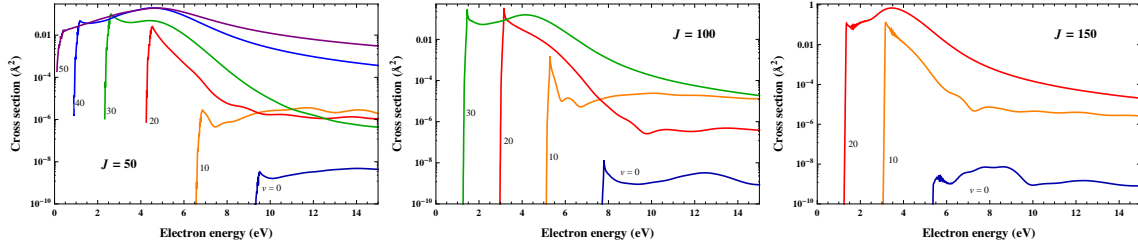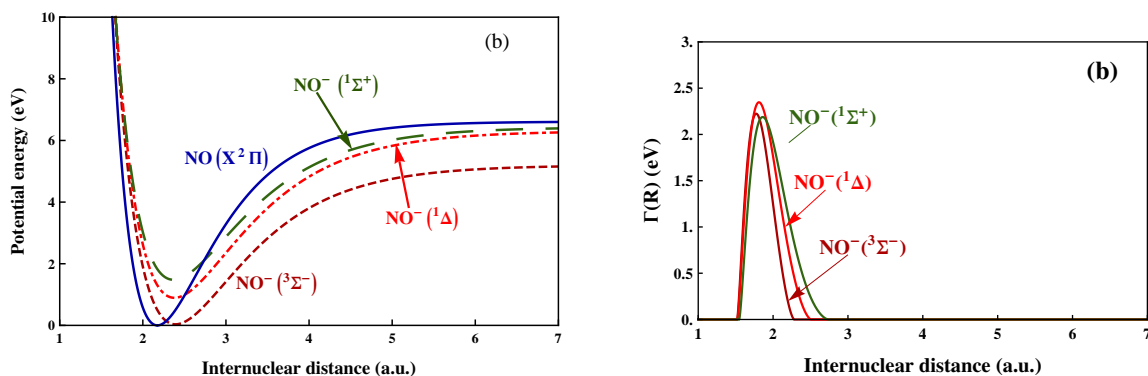

Figure 3.9: Resonant dissociation cross sections as a function of the electron energy, for some vibrational levels and for $J = 50$, $J = 100$ and $J = 150$.

	NO($X^2\Pi$)	NO$^-$($^3\Sigma^-$)	NO$^-$($^1\Delta$)	NO$^-$($^1\Sigma^+$)
D_e (eV)	6.61	5.16	5.41	4.95
R_e (a.u.)	2.17	2.39	2.38	2.37
α (a.u.)	1.48	1.20	1.18	1.20
W (eV)	0	0.035	0.895	1.480

Table 3.3: Morse potential parameters for NO and for the three symmetries of NO$^-$.

Figure 3.10: Morse potential for NO molecule (solid curve) and for the three NO$^-$ states: $^3\Sigma^-$ (dashed line), $^1\Delta$ (dot-dashed line) and $^1\Sigma^+$ (long-dashed line) for $J = 0$, and the $\Gamma(R)$.

3.2 NO

The resonant scattering of electron with nitric oxide involves three electronic states of NO$^-$ ion of $^3\Sigma^-$, $^1\Delta$ and $^1\Sigma^+$ symmetry, with statistical weight of $\frac{3}{8}$, $\frac{1}{4}$ and $\frac{1}{8}$ respectively. In this case the total cross section is given by the sum over three state:

$$\sigma_{if}(\epsilon) = \sigma_{if}^{^3\Sigma^-}(\epsilon) + \sigma_{if}^{^1\Delta}(\epsilon) + \sigma_{if}^{^1\Sigma^+}(\epsilon). \tag{3.1}$$

The Morse parameters for the neutral molecule and for the molecular ion, taken from the Refs. [77, 78, 79], are listed in Table 3.3. The corresponding potential curves are shown in Fig. 3.10 and the vibrational levels are listed in Table 3.4.

Figures 3.11–3.13 show the cross section, as a function of the electron energy, for some of the vibrational excitations, compared with experimental data of Allan [80], Jelisavcic et al. [61] and Josic et al. [81] and figure 3.14 shows the comparison with the calculations of Trevisan et al. [82]. Final results for vibrational excitations cross sections and rate constants are summarized in figs. 3.15 and 3.16.

v_i	ϵ_i (eV)	v_i	ϵ_i (eV)	v_i	ϵ_i (eV)	v_i	ϵ_i (eV)
0	0.000	14	2.908	28	4.959	42	6.150
1	0.236	15	3.083	29	5.072	43	6.203
2	0.468	16	3.254	30	5.181	44	6.251
3	0.695	17	3.420	31	5.286	45	6.294
4	0.918	18	3.582	32	5.387	46	6.333
5	1.137	19	3.739	33	5.483	47	6.368
6	1.351	20	3.892	34	5.575	48	6.399
7	1.561	21	4.041	35	5.662	49	6.425
8	1.767	22	4.185	36	5.745	50	6.446
9	1.968	23	4.325	37	5.824	51	6.464
10	2.165	24	4.460	38	5.898	52	6.477
11	2.357	25	4.592	39	5.968	53	6.485
12	2.545	26	4.718	40	6.033		
13	2.729	27	4.841	41	6.094		

Table 3.4: NO vibrational levels for $J = 0$ referred to the ground state which is at 0.119 eV from the bottom of the potential.
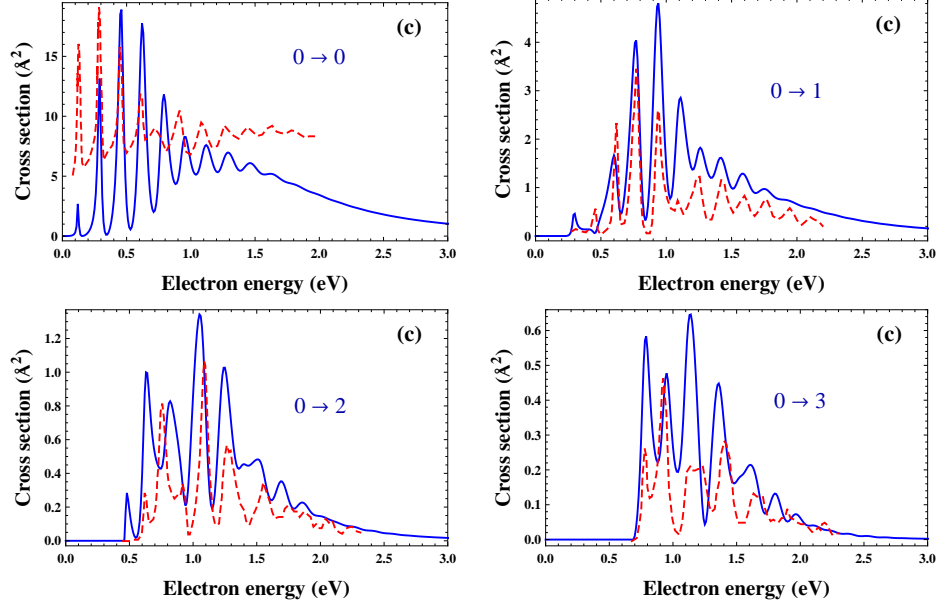

Figure 3.11: Calculated electron–NO resonant cross sections (solid line) compared with the experimental data of Allan (dashed line) [61].
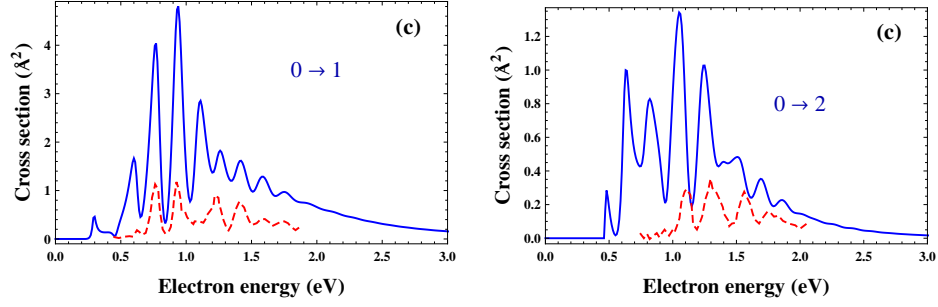
Figure 3.12: Calculated electron–NO resonant cross sections (solid line) compared with the experimental data of Jelisavcic et al. (dashed line) [80].
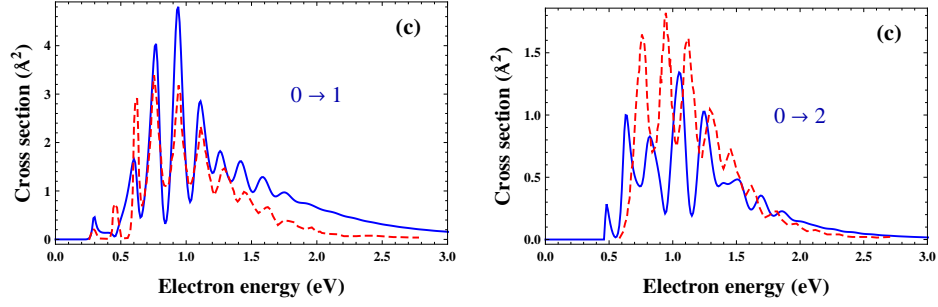

Figure 3.13: Calculated electron–NO resonant cross sections (solid line) compared with the experimental data of Josic (dashed line) [81].
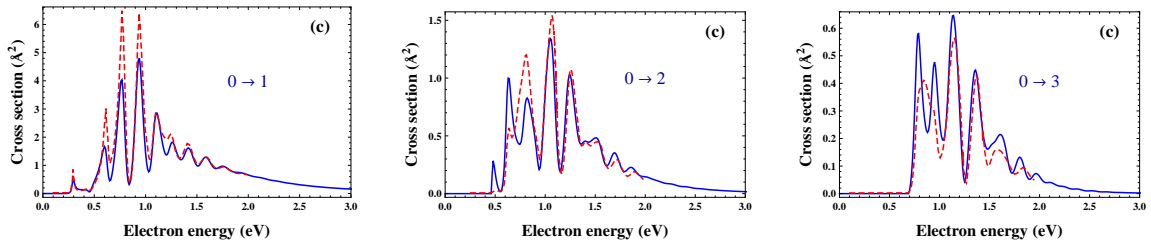

Figure 3.14: Electron–NO resonant cross sections compared with the theoretical results of Trevisan et al. [82], for the vibrational transitions indicated in the panels.
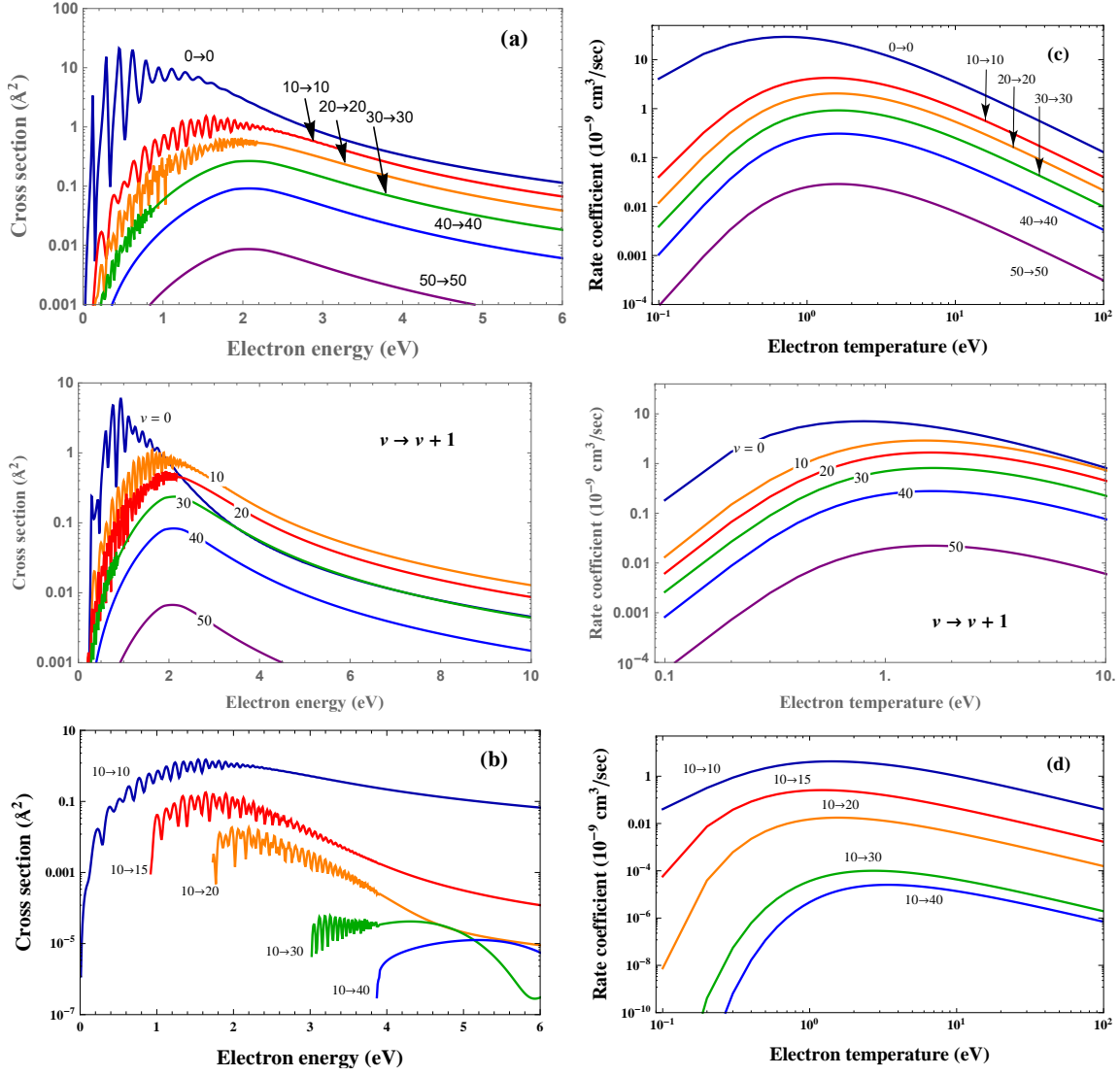
Figure 3.15: Summary of electron-NO vibrational excitation cross sections and on the corresponding rate coefficients.
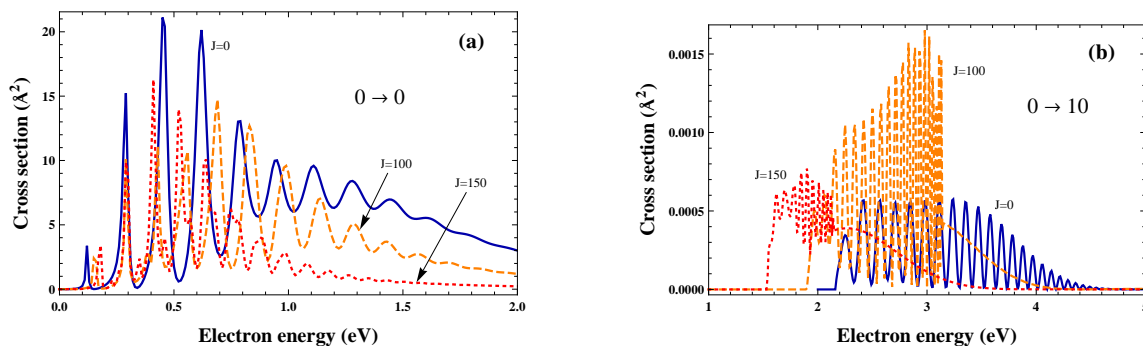
Figure 3.16: Effect of rotation on vibrational excitation cross sections of e-NO process.

3.3 O$_2$

Low energy electron-impact scattering for O$_2$ molecule involves four electronic states of the O$_2^-$ molecular ion, identified by the symmetries $^2\Pi_g$, $^2\Pi_u$, $^4\Sigma_u^-$ and $^2\Sigma_u^-$ [17]. In this section I refer to the processes of vibrational excitation, dissociative attachment and dissociative excitation, corresponding respectively to the processes 4, 5 and 6 in Table 3.1. First calculations were made by Noble *et al.* [83]. More recent papers on vibrational excitation scattering can be found in the Refs. [84, 85, 86, 87, 88]. Although dissociative electron attachment from oxygen molecules has been widely studied [89] there are only a few, rather old, papers reporting cross section measurements of the DEA process as a function of the incident electron energy. We cite here Rapp and Briglia [90], Schulz [91] and Christophorou *et al.* [92]. DEA from the $^1\Delta_g$ state of O$_2$ has also been observed [93] and found to have a cross section of similar magnitude to process involving the ground state. Cross sections for EID only appear to have been measured for electronically excited states of O$_2$ by Cosby [94]. An extensive collection of experimental data can be found in the review of Itikawa [95].

In the works in Refs. [40, 41, 42] we updated Noble *et al.*'s R-matrix calculations in order to have a better representation of the states involved in the scattering processes. Calculations were performed using the UKRMol codes [34] and the quantum chemistry code MOLPRO [71]. Orbitals for the O$_2$ were generated using configuration interaction (CI) calculations using a cc-pVTZ Gaussian-type orbital (GTO) basis set. The electrons in the lowest 3 core orbitals, $(1\sigma_g, 2\sigma_g, 1\sigma_u)^6$, were frozen and an active space was constructed from 9 valence orbitals $(3\sigma_g, 2\sigma_u, 3\sigma_u, 1\pi_u, 2\pi_u, 1\pi_g)^{10}$. The scattering calculations with 17 electrons also used a GTO basis [72] to represent the continuum electron. The calculations were based on the use of a complete active space CI representation which involves placing the extra electron in both a continuum orbital and target orbitals using the following prescription:

$$(1\sigma_g, 2\sigma_g, 1\sigma_u)^6 (3\sigma_g, 2\sigma_u, 3\sigma_u, 1\pi_u, 2\pi_u, 1\pi_g)^{11},$$
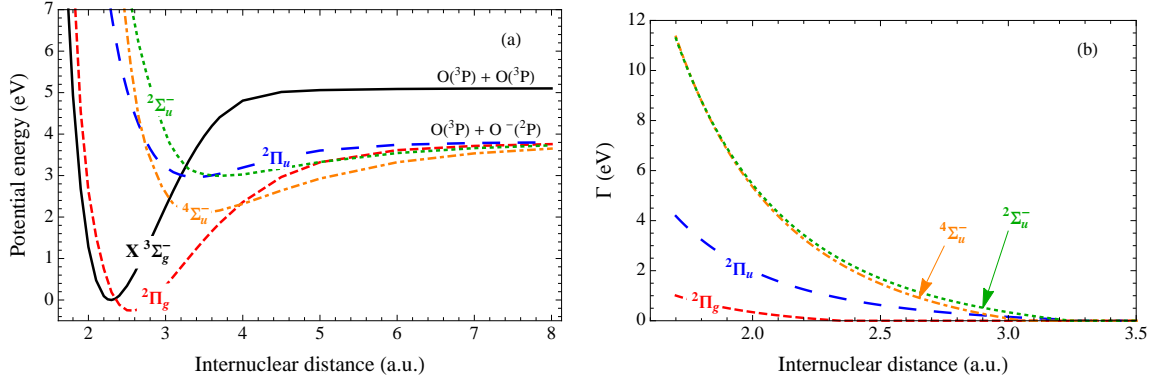
Figure 3.17: (a) Potential energy curves for ground state $X\,^3\Sigma_g^-$ of O_2 and for the four lowest resonant states O_2^-; (b) The corresponding resonance widths, $\Gamma(R)$.

and

$$(1\sigma_g, 2\sigma_g, 1\sigma_u)^6(3\sigma_g, 2\sigma_u, 3\sigma_u, 1\pi_u, 2\pi_u, 1\pi_g)^{10}(4\sigma_g, 5\sigma_g, 3\pi_u, 4\sigma_u, 2\pi_g, 3\pi_g, 1\delta_g, 1\delta_u)^1,$$

where the second set of configurations involves placing the extra electron in an uncontracted [74] target virtual orbital. Calculations used an R-matrix radius of 10 a_0. Both the MOL-PRO and R-matrix calculations were performed using D_{2h} symmetry. The potential energy curves and widths are shown in Fig. 3.17 and the list of vibrational levels is reported in Table 3.5.

For electron–O_2 resonant scattering, the vibrational excitation cross section can be divided into two distinct energy regions: below 4 eV, where the cross section exhibits sharp structures, and above this energy, where a broad maximum, peaked around 10 eV, is observed. Figure 3.18 shows the calculated RVE cross sections compared with Allan's results [96], for the first vibrational levels. At energy below 2 eV the $^2\Pi_g$ state of the O_2^- dominates and since this is the most stable anion state (see the lowest curve in Fig. 3.17(a)) and the longest lived (see the narrow resonance width in Fig. 3.17(b)), the cross section consists of a series of narrow spikes. As noted by Allan, the narrowness of the peaks makes experimental measurements difficult at low energy near the threshold, where the resonance width is comparable to the instrumental resolution. As a consequence the experimental error is large, about 35%. Within this experimental uncertainty, our absolute cross sections are generally lower than the experimental ones, showing a discrepancy for the highest peaks no larger than about a factor of two. The peak positions of the present results, reflecting the energy of the resonant vibrational levels, are slightly shifted with respect the experimental points.

Figure 3.19 shows the behavior of the cross sections in the second region where the $^4\Sigma_u^-$ resonance is supposed to be dominant. The principal feature is a broad peak in the cross

38

v	ϵ_v	v	ϵ_v	v	ϵ_v
0	0.000	14	2.435	28	4.280
1	0.196	15	2.587	29	4.382
2	0.388	16	2.735	30	4.476
3	0.573	17	2.881	31	4.565
4	0.756	18	3.024	32	4.651
5	0.937	19	3.164	33	4.730
6	1.117	20	3.301	34	4.794
7	1.291	21	3.436	35	4.847
8	1.461	22	3.568	36	4.898
9	1.629	23	3.696	37	4.938
10	1.796	24	3.821	38	4.960
11	1.960	25	3.942	39	4.976
12	2.122	26	4.059	40	4.987
13	2.281	27	4.172	41	4.994

Table 3.5: Calculated vibrational levels of O$_2$(X $^3\Sigma_g^-$). Energies are given in eV.
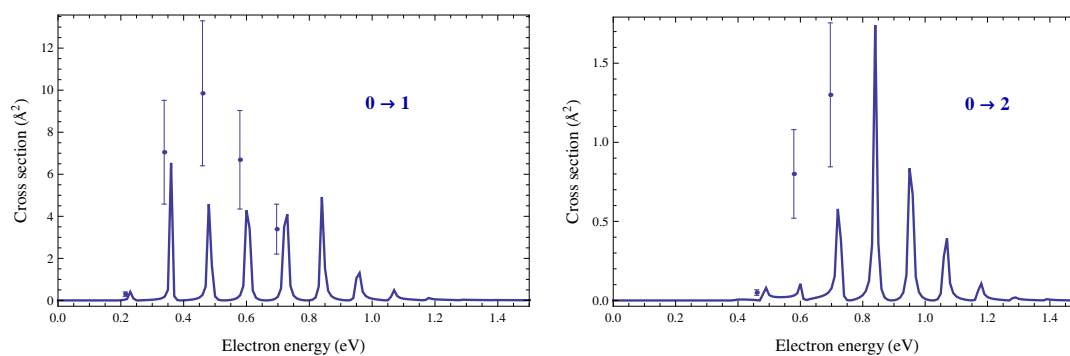
Figure 3.18: Electron–O$_2$ VE cross sections, at low energy where $^2\Pi_g$ state dominates, for $0 \rightarrow 1$ and $0 \rightarrow 2$ transitions compared with experimental results [96, 95].
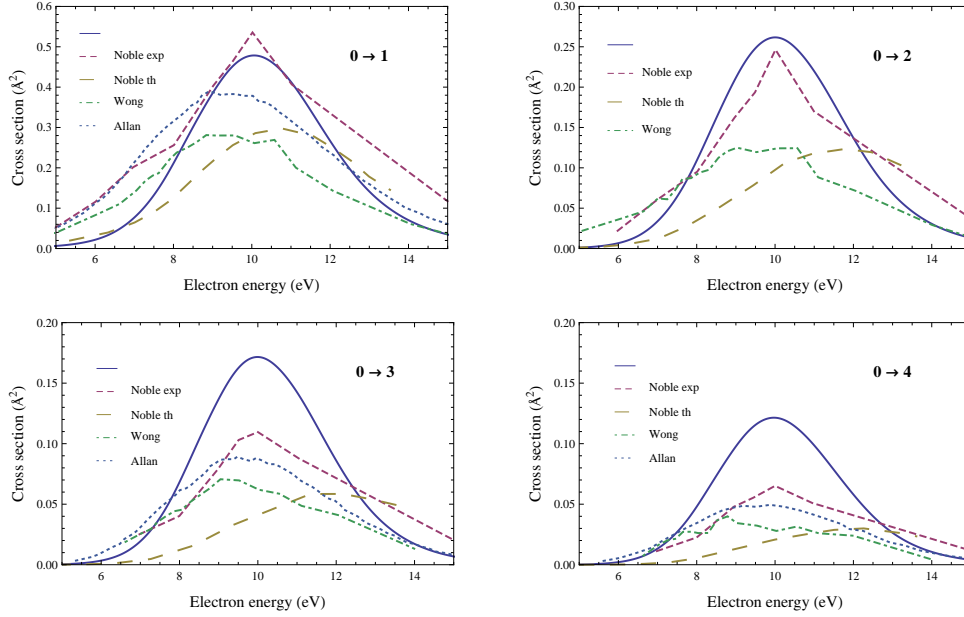
Figure 3.19: Angular integrated electron–O$_2$ vibrational excitation cross section in the 10 eV region. Our calculated cross sections (solid curve) are compared with experimental (dashed line, error of 20%–26%) and theoretical (long-dashed line) results of Noble *et al.* [83], Wong *et al.*'s measurements (dot-dashed line, error about 30%) [97] and Allan's experiment (dotted line, error 35%) [96].

section, located around 10 eV, which contrasts with the sharp shape of the peaks present at lower energies. Since a 10 eV electron has sufficient energy to dissociate the O$_2$ molecule, the interference between the neutral vibrational wave function in the entry-amplitude of Eq. (2.32) with the continuum part of the anionic spectrum, gives rise to a smooth shape for the cross section. This behavior is not present in other similar systems such as electron–CO [43] or electron–N$_2$ [37], where, above the dissociation threshold, the cross section shows a continuum unstructured shape which decreases monotonically with the energy.

Figure 3.20 shows our results for the DEA cross section for O$_2(v = 0)$ compared with the experimental results of Rapp and Briglia [90], Schulz [91] and Christophorou *et al.* [92]. The agreement is excellent, within the experimental error of ±15%: the peak is positioned at 6.43 eV with an absolute value of 0.0154 Å^2 and the FWHM of about 2 eV. As found experimentally, the main contribution to DEA cross section comes from the $^2\Pi_u$ state of O$_2^-$. We also note, at about 8.5 eV, the presence of a significant contribution due to the $^4\Sigma_u^-$ symmetry which, added to the main $^2\Pi_u$ contribution, reproduces the high-energy tail observed experimentally. The non-negligible contribution of $^4\Sigma_u^-$ resonance to DEA cross
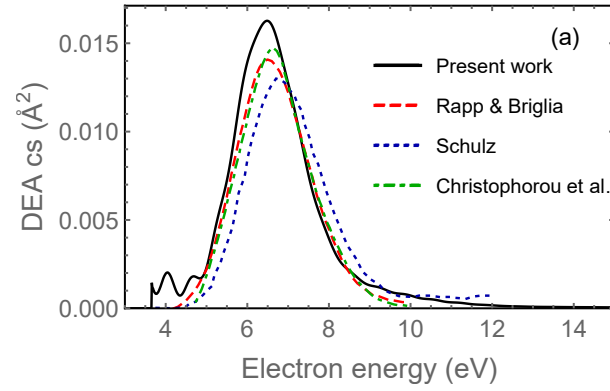
Figure 3.20: Calculated dissociative electron attachment cross section for $v = 0$ compared with experimental results of Rapp and Briglia [90], Schulz [91] and Christophorou *et al.* [92].

section has already been deduced from the measured angular distribution of O$^-$ ions [98].

Finally, figures 3.21, 3.22 and 3.23 summarize the results of electron-oxygen cross sections.

Figure 3.21: Electron-O_2 vibrational-excitation cross sections (left panels) and the corresponding rate coefficients (right panels) for rotational quantum number $J = 1$.

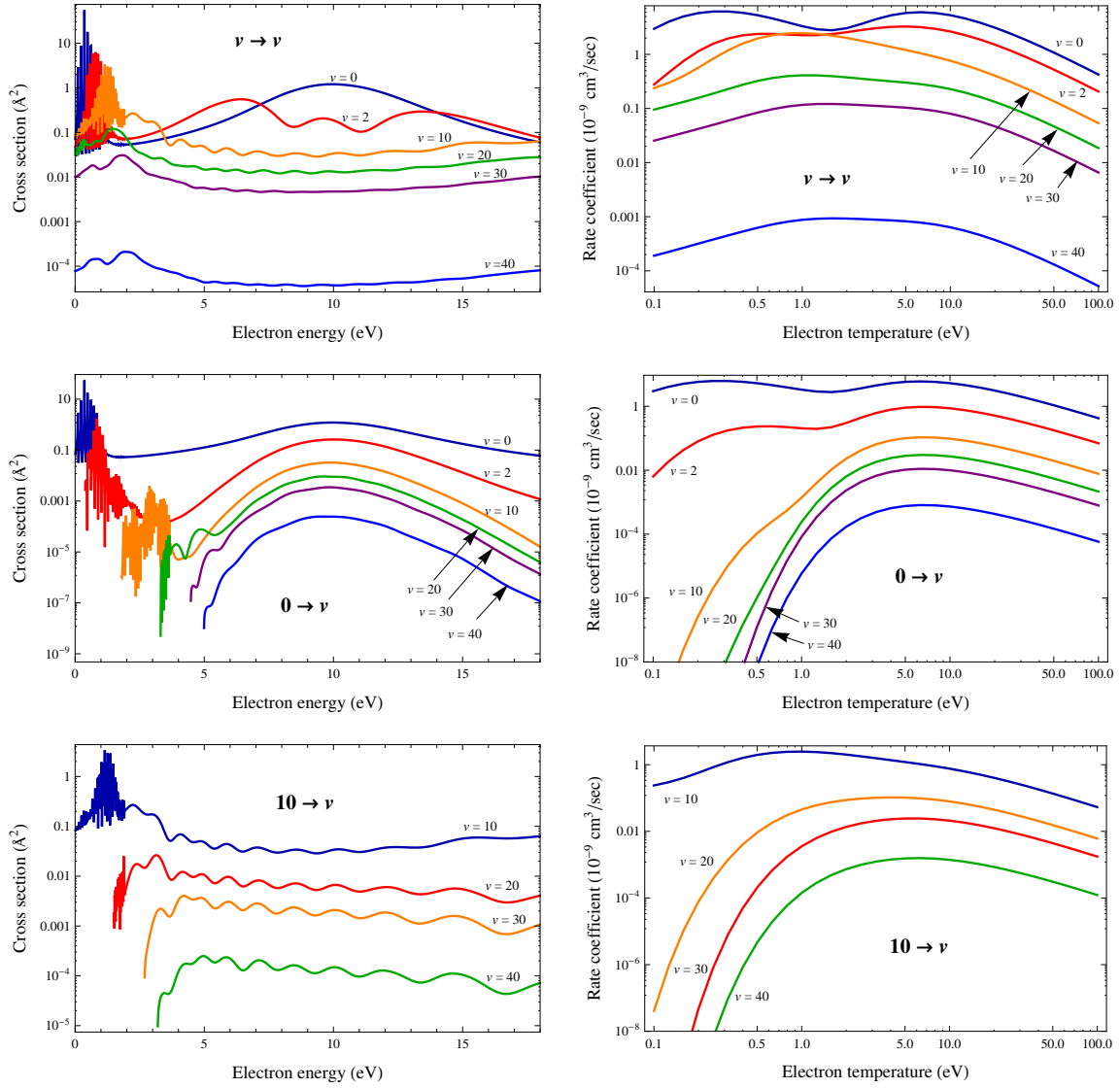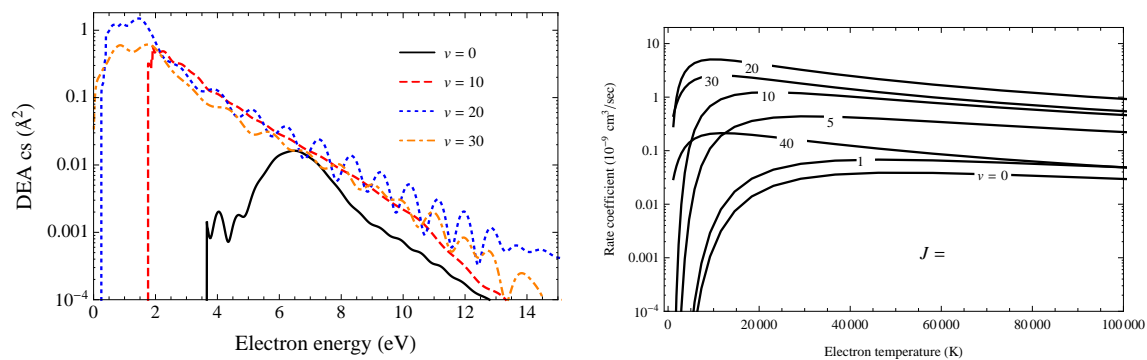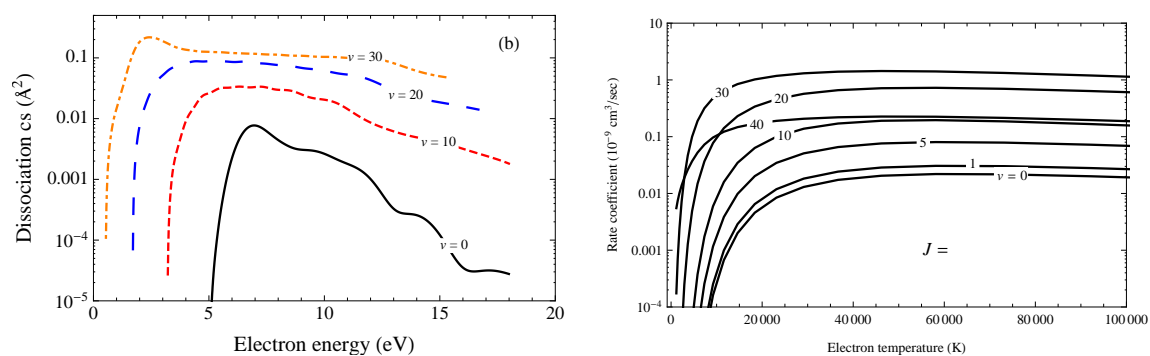Figure 3.22: Dissociative electron attachment cross sections and rate coefficients for vibrationally excited O$_2$.

Figure 3.23: Dissociative excitation cross sections and rate coefficients for vibrationally excited oxygen.

3.4 CO

In this section the results on state-to-state electron-CO scattering for vibrational excitation, dissociative attachment and dissociative excitation (processes 7, 8 and 9 in Table 3.1) are presented. Carbon monoxide is a very important molecule playing a fundamental role in many fields. It is, in fact, one of the most abundant species in interstellar medium and can act as a tracer for H_2 molecules, which, due to the lack of ground electronic state transition dipole moment, cannot be observed directly but is detected thorough collisions with CO molecules [99]. CO is a component of Mars' and Venus' atmosphere and, in the latter case, represents the most abundant chemical species. It therefore plays a crucial role also in space missions in connection to the (re-)entry problems [100]. Carbon monoxide, finally, is also useful in the understanding of processes involved in CO laser [101] and to study CO plasma in presence of electrical discharge [102, 103].

The first measurements has been made by Schulz [55]. Resonance enhanced vibrational excitation of CO from its vibrational ground state ($v_i = 0$) has been well-studied experimentally, notably in recent work by Allan [104], Poparić *et al.* [105] and by Gibson *et al.* [106]; earlier experimental work is reviewed by Brunger and Buckman [19] and a complete set od experimental data can be found in Itikawa paper [107]. Theoretically the best calculations are due to Morgan [106, 108, 109] who used an R-matrix method to characterize the resonance as a function of CO internuclear distance. Modeling the cooling of electrons in non-equilibrium CO-containing flows can be found in the papers in Refs. [110, 111, 112]. No experimental data are available for dissociative excitation while DEA has been measured by Rapp and Briglia [90].

Carbon and oxygen together, in CO, have a total of 10 valence electrons. To satisfy the octet rule for the carbon, the two atoms form a *triple bond*, with six shared electrons in three bonding molecular orbitals, rather than the usual double bond found in organic carbon compounds (one electron from double occupied *p*-orbital of oxygen goes into the empty carbon *p*-orbital). Since four of the shared electrons come from the oxygen atom and only two from carbon: (i) one of the bonding orbitals is occupied by two electrons from oxygen, forming a dative or dipolar bond. This causes a polarization of the molecule, with a small negative charge on carbon and a small positive charge on oxygen; (ii) The other two bonding orbitals are each occupied by one electron from carbon and one from oxygen, forming (polar) covalent bonds, and a reverse polarization is produced because the greater electronegativity of oxygen, with a small negative charge on oxygen. In the free carbon monoxide, a net negative charge δ^- remains at the carbon end and the molecule has a small dipole moment of $\mu = 0.122$ Debye [113]. This is schematically represented in Fig. 3.24. Oxygen has a larger electron density, but also a larger positive charge. Because most of the electron density is located between the atoms, the molecule has a net positive charge on the oxygen side. By contrast, the isoelectronic dinitrogen molecule has no dipole
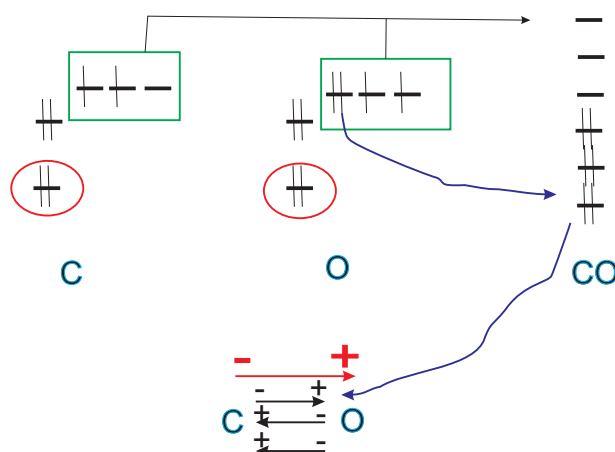
Figure 3.24: Triple bond and polarization in CO molecule.

moment.

The ground state $X^1\Sigma^+$ of potential energy for carbon monoxide CO has been calculated *via* Molpro [71] by using the aug-cc-pwCV5Z basis in MCSCF and MRCI configuration plus Davidson correction. Calculations for the resonant state were performed using the diatomic molecule implementation of the UK Molecular R-matrix codes [73] which uses Slater Type Orbitals (STOs) to represent the target and numerical functions to represent the continuum. Our methodology and calculations are heavily based on the work of Morgan [108]. We used the STO basis given by Kirby-Docken and Liu [114] to generate a total of 16σ and 12π molecular orbitals, and numerical Bessel functions for partial waves up to $l = 6$ for the continuum inside the R-matrix sphere which had a radius of 10 a_0. To avoid linear dependence problems, two of the continuum π orbitals were removed by Lagrange orthogonalization to the target orbitals [115]. Resonance positions and widths were obtained by fitting the $^2\Pi$ eigenphase sum at geometry to a Breit-Wigner form using program RESON [116]. Morgan tested a number of models but found that a Static Exchange plus Polarisation (SEP) model performed best. This model uses a Hartree-Fock (HF) target wavefunction and includes polarisation effects augmenting the scattering wavefunction with so called two particle – one hole (2p-1h) configurations. These configurations involve simultaneously exciting a single target electron into an unoccupied target ("virtual") orbital and placing the scattering electron in a virtual orbital. Results for resonances parameters are well-known to be sensitive to the precise choice of parameters in an SEP calculation [117]. Our final model froze the C and O 1s and 2s electrons and considered excitation of remain 6 "valence" electrons into virtual orbitals, all of which were retained. At the CO equilibrium bondlength this model gives a resonance position and width of (1.67, 0.82) eV which can be compared to Morgan's values of (1.68, 0.95) eV. It can be seen that the positions are in excellent agreement but our
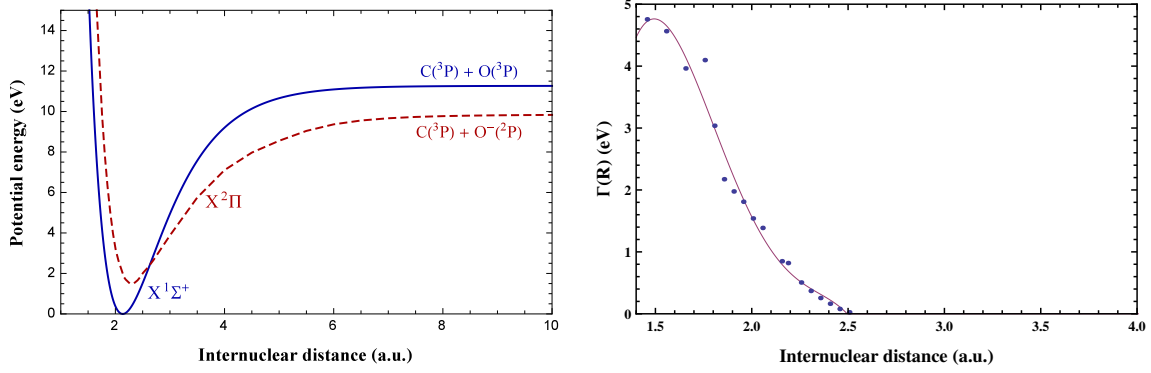
Figure 3.25: Potential energy curves for CO (solid curve) and CO$^-$ (dashed line) and the resonance width. The asymptotical electron affinity is 1.43 eV whereas the experimental oxygen electron affinity is 1.46 eV [118]

width is somewhat narrower. As discussed below, it was decided to increase our calculated widths by 10 % to improve agreement with experiment. Final results on potential energy curve and resonance width are shown in 3.25 and the list of vibrational levels of CO is reported in Table 3.6.

In order to validate the results, Fig. 3.26 compares our cross sections with the Allan results and the theoretical predictions of Morgar for some VE cross sections. Finally, Figures 3.27, 3.28 and 3.29 summarize the results for $J = 0$ for the three processes considered while Figs. 3.30 and 3.31 show the effect of rotation.

v	$\epsilon_{v,0}$ (eV)	v	$\epsilon_{v,0}$ (eV)	v	$\epsilon_{v,0}$ (eV)	v	$\epsilon_{v,0}$ (eV)
0	0.0000	20	4.8243	40	8.2869	60	10.3877
1	0.2735	21	5.0297	41	8.4243	61	10.4570
2	0.5437	22	5.2318	42	8.5582	62	10.5229
3	0.8104	23	5.4305	43	8.6888	63	10.5854
4	1.0738	24	5.6257	44	8.8160	64	10.6445
5	1.3337	25	5.8176	45	8.9397	65	10.7002
6	1.5902	26	6.0060	46	9.0601	66	10.7524
7	1.8434	27	6.1911	47	9.1771	67	10.8013
8	2.0931	28	6.3727	48	9.2906	68	10.8468
9	2.3394	29	6.5510	49	9.4008	69	10.8888
10	2.5823	30	6.7258	50	9.5075	70	10.9275
11	2.8218	31	6.8972	51	9.6109	71	10.9628
12	3.0580	32	7.0652	52	9.7108	72	10.9946
13	3.2907	33	7.2299	53	9.8073	73	11.0231
14	3.5200	34	7.3911	54	9.9005	74	11.0481
15	3.7459	35	7.5489	55	9.9902	75	11.0697
16	3.9684	36	7.7033	56	10.0765	76	11.0880
17	4.1874	37	7.8543	57	10.1594	77	11.1028
18	4.4031	38	8.0019	58	10.2389	78	11.1142
19	4.6154	39	8.1461	59	10.3150	79	11.1222
						80	11.1267

Table 3.6: CO vibrational levels and the corresponding energies (relative to the state $v = 0$) for ground electronic state and for $j = 0$. The dissociation energies are $D_e = 11.266$ eV and $D_0 = 11.128$ eV.
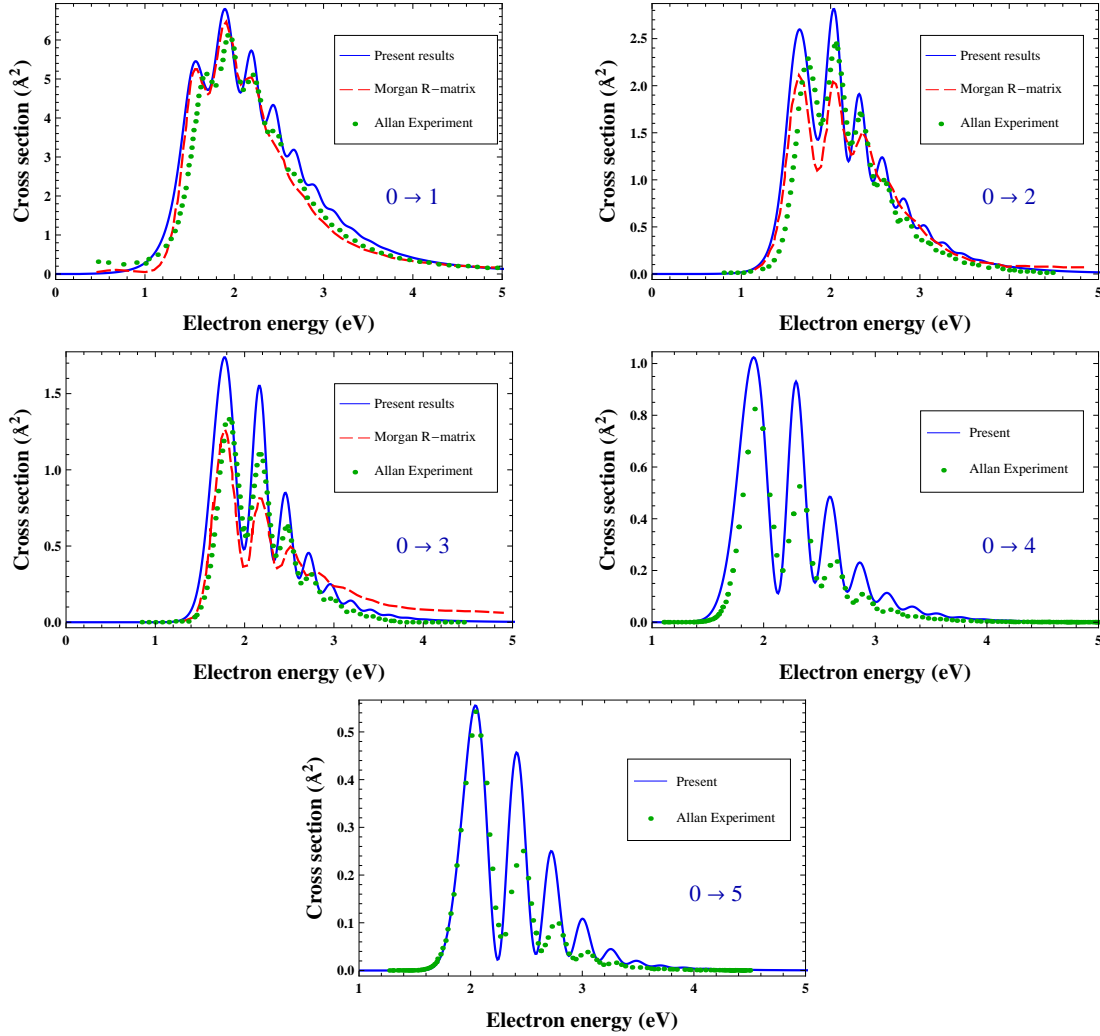
Figure 3.26: electron-CO resonant cross sections compared with experimental results of Allan [104] and the theoretical R-matrix calculation of Morgan [108].
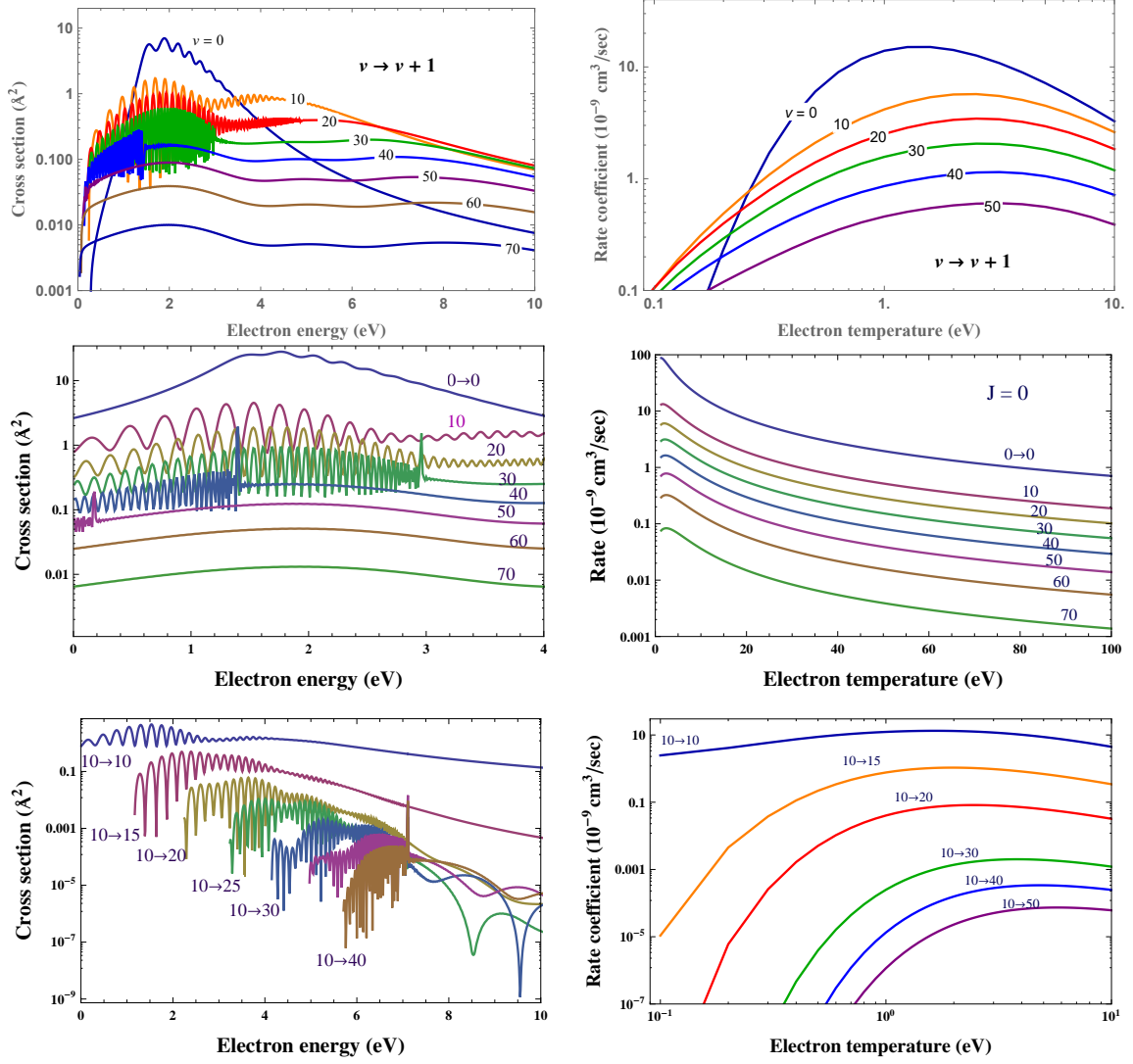
Figure 3.27: Summary of electron-CO VE cross sections.
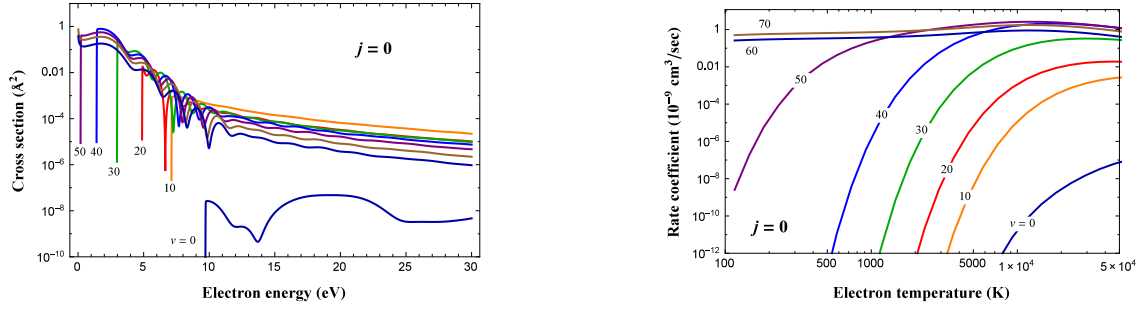
Figure 3.28: Vibrational state-resolved dissociative electron attachment cross sections and the corresponding rate constants for $j = 0$.
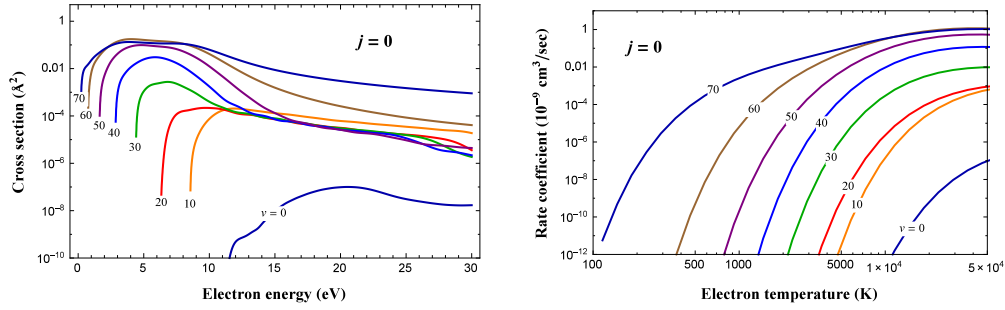
Figure 3.29: Vibrational state-resolved electron-impact dissociation cross sections and the corresponding rate constants for $j = 0$.
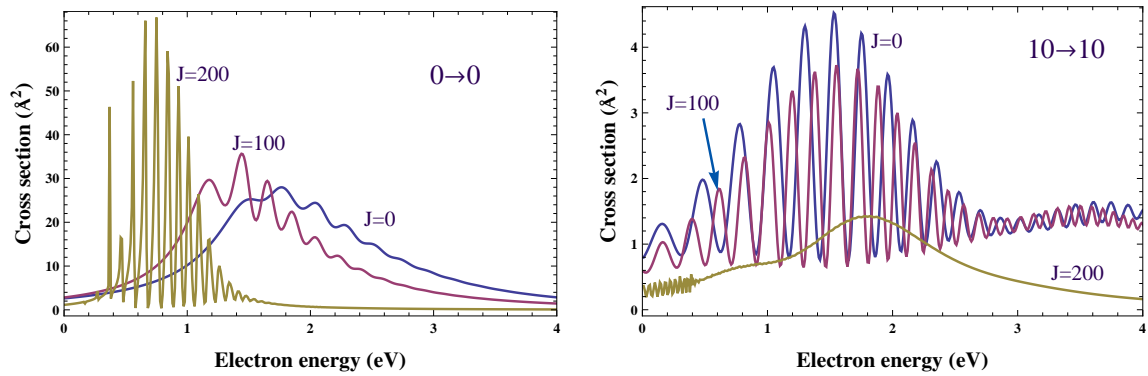
Figure 3.30: Effect of rotation on electron-CO VE cross sections for different values of J.

Figure 3.31: Rotational state-resolved cross sections for $v = 0$: (a) dissociative electron attachment and (b) electron impact dissociation. Dashed-black curves refer to the j-averaged cross sections calculated by assuming a rotational temperature of 10000 K.

3.5 CO$_2$

One of the technological problems, connected with strategies for reduction of the global warming coming from the greenhouse effect produced by carbon dioxide, is represented by the capture at source and storage of the CO$_2$ gas, mainly based on the plasmolysis process leading 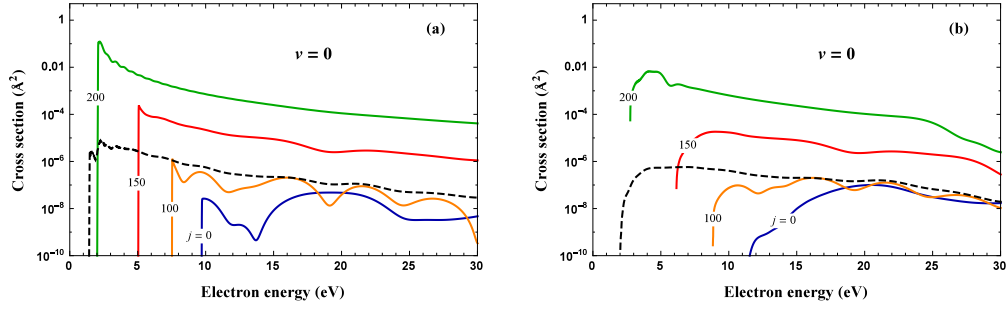to the splitting of CO$_2$ into CO molecules and atomic or molecular oxygen [119, 120]. The efficiency of the dissociation processes is strongly determined by the vibrational activation of the molecule. Models of CO$_2$ plasmas, aimed to optimize and clarify this chemical conversion, have recently been constructed [121, 122, 112, 123, 124, 125]. The main limitation of these models is the lack of information on electron-impact cross sections or rate coefficients for collisions inducing vibrational transitions in CO$_2$ molecules; as result modellers usually resort to estimated rates or approximate scaling-laws [124].

In order to fill this void, in the Ref [45] was presented a preliminary data set of electron-impact cross sections for vibrational excitation of ground electronic state of carbon dioxide molecule useful in plasma kinetic modeling. The cross sections show two distinctive features observed experimentally: a $^2\Pi_u$ shape resonance around 3.8 eV [126, 127, 128] and, at energies below 2 eV, an enhancement due to the presence of the $^2\Sigma_g^+$ symmetry virtual state [129, 130, 131]. Both phenomena are explained in terms of a temporary CO$_2^-$ system. For a general review on this topics see Itikawa paper [132] and references therein.

In Ref. [45] was presented the cross sections for the following process:

$$e + \text{CO}_2(\text{X}\,^1\Sigma_g^+; v) \rightarrow \text{CO}_2^-(^2\Pi_u) \rightarrow e + \text{CO}_2(\text{X}\,^1\Sigma_g^+; v')\,, \tag{3.2}$$
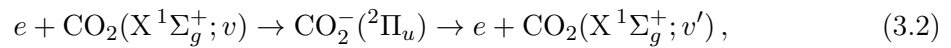
which occurs through the formation of the shape resonance generated by the electronic state $^2\Pi_u$ of the CO$_2^-$ ion. CO$_2$ in its ground electronic state, X$\,^1\Sigma_g^+$, is a linear molecule with C–O equilibrium distance $R_{eq} = 2.19\,a_0$ characterized by three normal modes of vibration,

denoted in the following by $v = (\nu_1, \nu_2, \nu_3)$ and referred to, respectively, as the symmetric stretching, bending mode (doubly degenerate) and asymmetric stretching.

In principle, scattering involving polyatomic molecules needs a multidimensional treatment of the potential energy surface and of the nuclear motion, in order to take into account the non-adiabatic coupling between different vibrational modes [133]. However, as we are limiting ourself to the lowest vibrational levels, where the potential energy is approximatively harmonic, is possible to adopt the assumption of separation of the modes and split the CO_2 potential into three one-dimensional independent modes. This allows one to compute the cross sections employing the local model of resonant collisions as formulated for diatomic vibrational excitation [37, 39, 41]. In the uncoupled vibrational mode approximation, each mode is considered as independent. This implies that the scattering processes involves one mode only and does not affect at all the other two. Preliminary results for the symmetric stretch mode only, were given previously [134]. Here we present calculations on all the three normal modes of the molecule, for $0 \leq \nu_i \leq \nu_i' \leq 10$ ($i = 1, 2, 3$), and for electron collision energies from the threshold up to 10 eV.

A peculiar aspect of the the doubly degenerate $^2\Pi_u$ symmetry of CO_2^- ion is that it splits, upon bending, into two (Renner-Teller) $^2A_1$ and $^2B_1$ components, no longer degenerate, due to the breaking of linear geometry (D_{2h} symmetry to C_{2v} symmetry of bending mode) [135, 136, 137]. A second aspect, that derives from the stretch-bend coupling possible in polyatomic molecules, is an accidental degeneracy of vibrational levels belonging to different modes, known as Fermi resonance [137, 132]. In the case of CO_2 a quasi-degeneracy occurs between the pure stretch (100) and the pure bending (020) levels (Fermi dyads) that result in a near 50:50 mixing of the two states which is well-known experimentally [128]. Here we neglect this stretch-bend coupling; it is at least arguable that including it will only result in redistribution of flux in the excitation cross sections rather than radically different excitation rates.

The CO_2 potential energy curves were computed using the *ab-initio* quantum chemistry code MOLPRO [71], by adopting a aug-cc-pVQZ basis set and the coupled-cluster (CCSD(T)) and MCSCF models. Scattering calculations were performed using the UK polyatomic R-matrix codes [33, 34]. A static exchange plus polarization (SEP) model, and the same basis used for CO_2, were utilised to calculate the complex potential energy curve for CO_2^-. The R-matrix calculations were performed on a grid of fixed internuclear distances. The position and width of the resonant state were then calculated by fitting the corresponding eigenphases sum with a Breit-Wigner function [116].

The potential energy curves for CO_2 and CO_2^- species and for the three normal modes, are shown in Fig. 3.32 along with the corresponding resonance widths Γ. These curves are plotted as a function of the atomic displacements, Δ, calculated with respect to the equilibrium geometry for the three modes. Table 3.7 reports the vibrational energy levels ϵ_{ν_i} for each normal mode ($i = 1, 2, 3$).

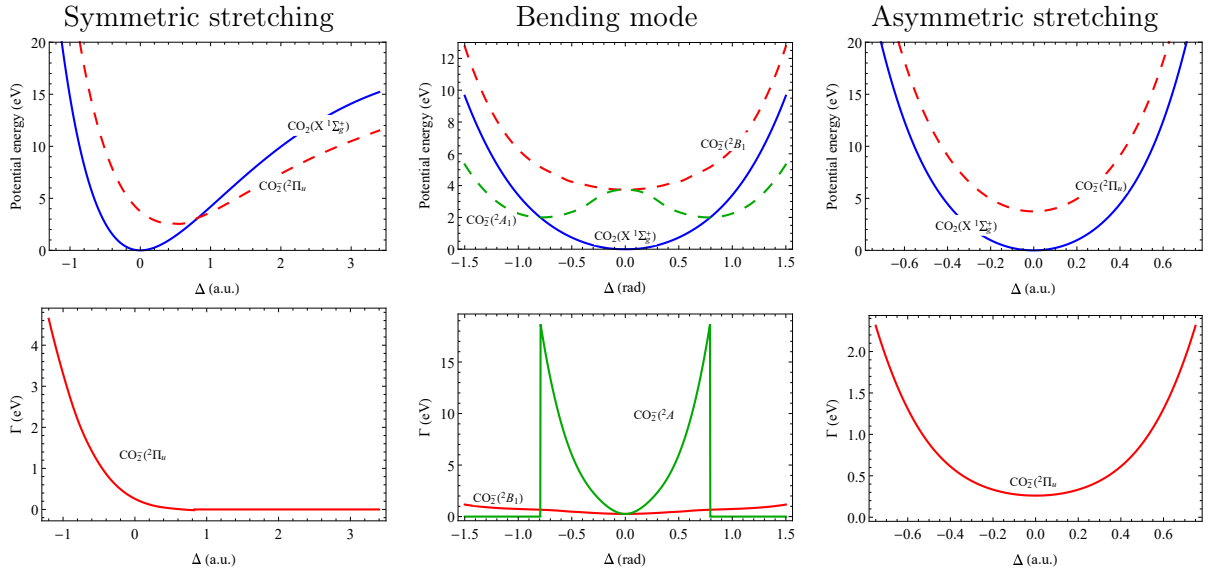Figure 3.32: Upper panels: Potential energy curves for the electronic ground electronic state X $^1\Sigma_g^+$ of CO$_2$ (full-blue line) and for the resonant state CO$_2^-$ (dashed-red and green lines) for the three normal modes symmetric stretching, bending and asymmetric stretching. Lower panels: the corresponding resonance widths. Δ represents the displacement from the equilibrium geometry.

ν_i	Symmetric stretching $i = 1$	Bending mode $i = 2$	Asymmetric stretching $i = 3$
0	0.	0.	0.
1	0.1676 (0.172)	0.0764 (0.082)	0.2973 (0.291)
2	0.3345	0.1585 (0.159)	0.5996
3	0.5007	0.2415	0.9052
4	0.6661	0.3246	1.2138
5	0.8309	0.4081	1.5252
6	0.9949	0.4919	1.8396
7	1.1583	0.5760	2.1569
8	1.3208	0.6604	2.4771
9	1.4827	0.7450	2.8000
10	1.6439	0.8299	3.1257
$\epsilon_{\nu_i=0}$	0.0840	0.0357	0.1469

Table 3.7: CO_2 vibrational levels ϵ_{ν_i} in the three normal modes referred to the energy of the corresponding ground vibrational levels whose value $\epsilon_{\nu_i=0}$, with respect to the minimum of the potential energy curve, is given in the last row. In parenthesis are shown the experimental values from Ref. [137]. All entries are in eV.

In order to validate the results, Fig. 3.33 shows the comparison with experimental data for symmetric stretching cross sections available in literature.

Figure 3.34 shows selected cross section results, as a function of the incident electron energy, for the three normal modes. All cross section curves show a main pronounced peak close to 3.8 eV which corresponds to the CO_2^- resonance threshold. The other secondary peaks correspond to the CO_2^- vibrational levels (boomerang oscillations).
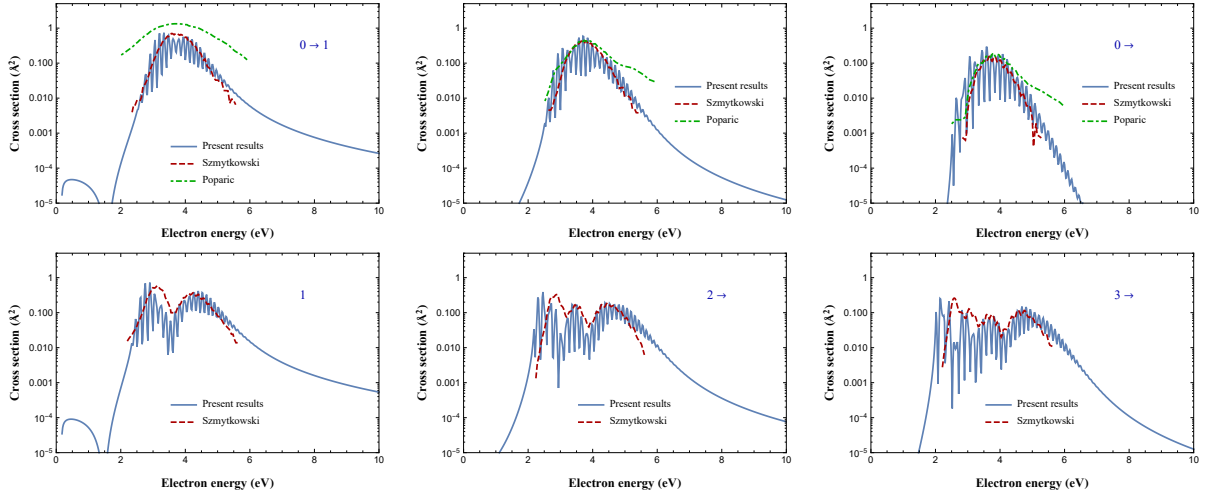
Figure 3.33: Comparison between present results with available experimental data in Refs. [138, 139] for selected symmetric stretching cross sections.
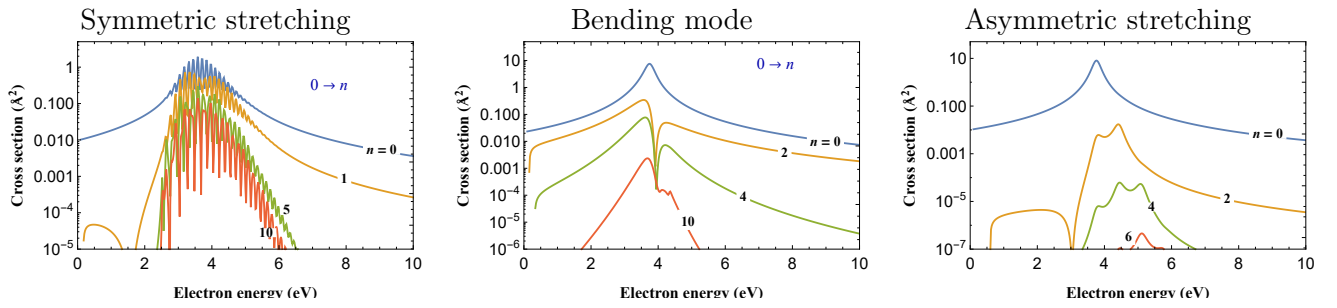

Figure 3.34: Summary of the electron-CO$_2$ vibrational excitation cross sections.

3.6 He_2^+

He_2^+ is a simple molecular ion that is present in many natural and technological systems. It plays a dominant role in electric discharges [140] and stellar medium [141], as well as in the chemistry of the early universe [5, 142] and thermonuclear fusion [143]. In helium containing plasmas, electron-impact dissociative recombination and direct dissociation are among the main reactive processes of the He_2^+ ion leading to atomic and ionic species. Dissociative recombination is a low-energy process occurring through temporarily neutralization of He_2^+ ion followed by dissociation into two He atoms. It has been widely studied due its importance in relatively low-temperature system (see Ref. [144] and references therein). On the opposite side, direct dissociation of He_2^+ induced by electron-impact into He atom and He^+ ion requires fast electrons with a kinetic energy equal or larger than the excitation energy of the process, which amounts, at the ground state equilibrium bond-length, to about 10 eV. Corresponding temperatures of this order of magnitude of energies are typical for the divertor plasmas of toroidal fusion devices. The plasma cooling in the divertor region favors the recombination processes which allow for the formation of molecular excited species, so that plasma chemistry, involving gas-phase and surface becomes rather complex.

The basis set employed in this work is the cc-pVTZ Gaussian basis set for He_2^+ molecule. This set includes polarization functions. The electronic configuration for the ground state $\text{X}\,^2\Sigma_u^+$ of He_2^+ in its natural symmetry is $(1\sigma_g)^2\,(1\sigma_u)$. The molecule is treated in a reduced D_{2h} symmetry. In the close coupling expansion of the trial wave function of the scattering system, we included the X state and the first excited state $\text{A}\,^2\Sigma_g^+$, $(1\sigma_g)^2\,(2\sigma_g)$. CI wave functions are used to represent each target state. In our CI model, we have the occupied orbitals which are augmented by the virtual (vacant) molecular orbitals. We include virtual orbitals up to $7a_g$, $3b_{2u}$, $3b_{3u}$, $1b_{1g}$, $7b_{1u}$, $3b_{2g}$, $3b_{3g}$, $1a_u$. The three molecular orbitals were free to move into the entire active space. The vertical excitation energy of the A state at equilibrium distance is 9.954 eV with respect to the X state. We obtained for the dipole transition moment of X-A transition a value of 0.96856 a.u.

Figures 3.35(a) and (b) show a comparison of our R-matrix potential curves and transition dipole moments, with those of Refs. [145] and [146], respectively. The ground and excited states of He_2^+ support respectively 24 and 2 vibrational levels. The corresponding eigenvalues are shown in Table 3.8. The shallow minimum of A state appears at $R \approx 8.7$ a.u. an internuclear distance far away from the Franck-Condon (FC) regions of $\text{X}\,^2\Sigma_u^+$ so it cannot affect the dissociation process in any way.

The state-resolved cross sections calculated in Adiabatic Nuclei approximation are shown in Fig. 3.36. The local maximum at 7 eV is generated by the formation of a resonance occurring in the low energy region.
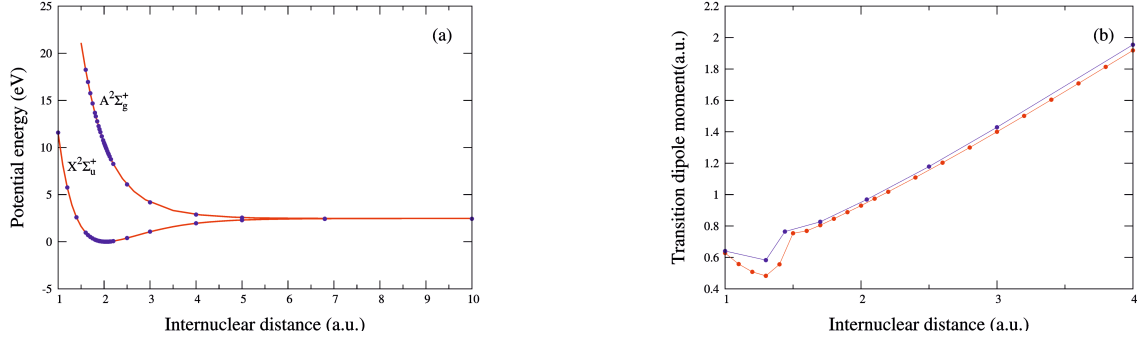
Figure 3.35: (a) Ground (X $^2\Sigma_u^+$) and excited (A $^2\Sigma_g^+$) R-matrix electronic potential energies and (b) transition dipole moments compared with the calculations taken from Refs. [145] and [146] respectively.
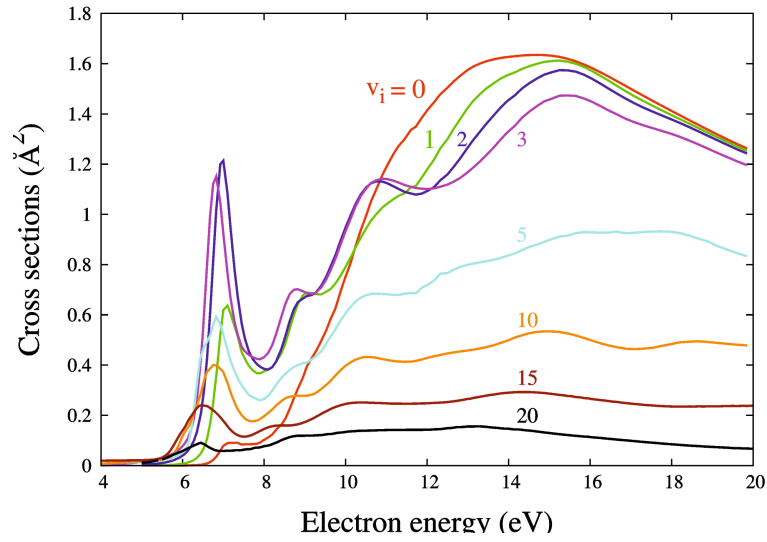
Figure 3.36: State-resolved AN cross sections for different He$_2^+$ vibrational levels v_i.

v	X $^2\Sigma_u^+$ Present results	X $^2\Sigma_u^+$ Ref. [147]	A $^2\Sigma_g^+$ Present results	A $^2\Sigma_g^+$ Ref. [145]
0	0.1042	0.1042	2.4733	2.4730
1	0.3069	0.3061	2.4743	2.4740
2	0.4997	0.4992		
3	0.6839	0.6837		
4	0.8597	0.8594		
5	1.0265	1.0264		
6	1.1846	1.1846		
7	1.3346	1.3340		
8	1.4761	1.4745		
9	1.6094	1.6062		
10	1.7347	1.7289		
11	1.8521	1.8426		
12	1.9607	1.9472		
13	2.0597	2.0426		
14	2.1485	2.1288		
15	2.2266	2.2056		
16	2.2938	2.2729		
17	2.3501	2.3306		
18	2.3952	2.3785		
19	2.4292	2.4165		
20	2.4523	2.4446		
21	2.4651	2.4627		
22	2.4700	2.4715		
23	2.4740	2.4739		

Table 3.8: Vibrational eigenvalues (eV) for the X $^2\Sigma_u^+$ and A $^2\Sigma_g^+$ electronic states compared with those from Ref. [147] and Ref. [145] respectively. All the values are referred to the bottom of the ground state potential curve.

3.7 BeH$^+$

Because of its low-core plasma radiation losses, high oxygen gathering capability and re-
duced erosion and migration (relative to other plasma facing materials), beryllium has been
chosen as a first wall material in the main chamber of the International Thermonuclear Fu-
sion Reactor (ITER) [11, 10]. The interaction of a hydrogen fusion plasma with the Be
reactor walls will result in release of both atomic Be and Be hydrides (BeH, BeH$_2$) into the
bulk. The experiments with deuterium plasma–Be-wall interaction, performed in the linear
divertor plasma simulator PISCES-B [148, 149, 150], have indeed demonstrated copious
production of BeD molecules reaching 80% of the total Be release at plasma ion impact
energies of $\sim$10 eV and 40% at 70–90 eV ion energies [150]. In a recent experiment on JET
(with Be first wall and tungsten divertor) the BeD fraction was found to be about 33%
of the total Be release at the ion impact energy of 75 eV [151]. The molecular-dynamics
simulations [150, 152] confirm these experimental findings and predict even a higher frac-
tion of BeD molecules in the total beryllium erosion. This indicates that the chemistry
in low-temperature edge regions ($< 0.5 - 20$ eV) of a hydrogen plasma interacting with
a beryllium wall, will be dominated by the processes of beryllium hydride BeH (and its
ionization and dissociation products) with the basic plasma constituents.

Collision processes with BeH and BeH$^+$ with electrons, as well as their reactions with
H and H$^+$, are therefore of great importance for transport modelling studies of beryllium
in edge plasmas and for the molecular diagnostics of these plasmas based on the BeH and
BeH$^+$ radiation. Unfortunately, due to the high toxicity of beryllium, no measurements
on electron scattering process with BeH$^+$ are available in literature and the required cross
section information for these processes are very scarce. Thus, calculations seem to be the
only way to obtain these data. For the BeH$^+$ ion the collision processes studied so far are
the electron-impact electronic excitation [153] and the dissociative recombination [154, 155,
156, 157, 158, 159]. In particular, we note that only a few studies considered vibrationally-
excited BeH$^+$ ions [153, 157, 158, 159].

Potential energy curves (PECs) for the ground electronic state X $^1\Sigma^+$ and the first
excited electronic state $a\,^3\Sigma^+$ of BeH$^+$ were calculated by using the *ab-initio* quantum
chemistry code MOLPRO [71]. The calculation used internally-contracted multi-reference
configuration interaction (ic-MRCI) level of theory with a cc-pVTZ basis set and were
performed in C_{2v} symmetry. These calculations kept the $1\,a_1$ orbital frozen and used 9
active orbitals, $(5\,a_1, 2\,b_1, 2\,b_2)$, and 34 external orbitals $(14\,a_1, 8\,b_1, 8\,b_2, 4\,a_2)$, for a total
of 44 contractions. The calculations covered 30 internuclear distances between $1.5\,a_0$ and
$10\,a_0$.

The *ab-initio R*-matrix method [33, 34] was used to determine the positions and widths
of BeH resonant states in the electron-BeH$^+$ scattering, as a function of the internuclear
distance. An initial configuration interaction (CI) calculation was first performed at the

BeH$^+$ equilibrium bond length $R_e = 2.5369$ a_0 using the Slater-type orbital (STO) basis set of Bagus *et al.* [160]. The basis set contained 5 s-type, 4 p-type, 2 d-type and 1 f-type STOs centered on the Be atom and 3 s-type, 1 p-type and 1 d-type STOs centered on the H atom respectively. A set of molecular orbitals containing 17 σ, 9 π, 4 δ and 1 ϕ were then built using the STOs. Subsequently, a self-consistent field (SCF) calculation was performed for the lowest BeH$^+$ states using these molecular orbitals. Finally, 17 σ, 9 π and 4 δ were used in a CI calculation using a $(1\sigma - 6\sigma, 1\pi, 2\pi)^4$ complete active space (CAS) target model as it gave good agreement of the vertical excitation energies for the target at the equilibrium bond length. Calculations were then repeated for 55 internuclear distances, from 1.5 a_0 to 10 a_0, to yield the BeH$^+$ target PECs. To get the bound states, an inner region calculation was first made with the CAS target model mentioned above, supplemented by continuum orbitals obtained from a truncated partial wave expansion about the molecular center of mass. The inner region solutions were then used to construct an R-matrix at the boundary. The R-matrix was propagated to 50.01 a_0 in the outer region where, in addition to the Coulomb potential, the diagonal and off diagonal dipole and quadrupole moments of the BeH$^+$ target states were included. Bound states were then found using the searching algorithm of Sarpal *et al.* [76]. For the resonant states, the R-matrix was propagated to 70 a_0 and was matched to asymptotic Coulomb functions obtained using a Gailitis expansion [161]. Resonances were detected and fitted to a Breit-Wigner profile to obtain their positions and widths. Calculations were repeated for 55 internuclear distances in the range 1.5 a_0 to 10 a_0 to obtain the BeH bound state PECs, resonance curves and resonance widths as a function of the internuclear distance. The full details can be found in Refs. [154, 162].

A total of 12 resonant states in $^2\Sigma^+$ (5 states), $^2\Pi$ (5 states) and $^2\Delta$ (2 states) symmetries were considered. The final PECs and widths are summarized in Fig. 3.37 for BeH$^+$ and BeH** resonant states where a splineing procedure was applied to the calculated points. Table 3.9 contains the list of vibrational levels of BeH$^+$ and its isotopes and Table 3.10 reports the number of rotational levels for each vibrational state.

v^+	BeH$^+$	BeD$^+$	BeT$^+$
0	0.134	0.100	0.085
1	0.396	0.296	0.253
2	0.648	0.486	0.417
3	0.890	0.672	0.577
4	1.121	0.852	0.734
5	1.340	1.026	0.886
6	1.549	1.193	1.034
7	1.748	1.354	1.176
8	1.937	1.510	1.315
9	2.113	1.660	1.449
10	2.278	1.805	1.580
11	2.430	1.943	1.706
12	2.569	2.075	1.828
13	2.695	2.200	1.946
14	2.807	2.319	2.059
15	2.903	2.431	2.167
16	2.981	2.535	2.270
17	3.041	2.633	2.368
18	3.077	2.722	2.462
19		2.804	2.549
20		2.877	2.632
21		2.941	2.709
22		2.995	2.780
23		3.038	2.846
24		3.068	2.904
25			2.956
26			3.000
27			3.037
28			3.064

Table 3.9: Energy (eV) of vibrational levels for three isotopes with respect to the bottom of BeH$^+$ potential energy curve for $j = 0$.
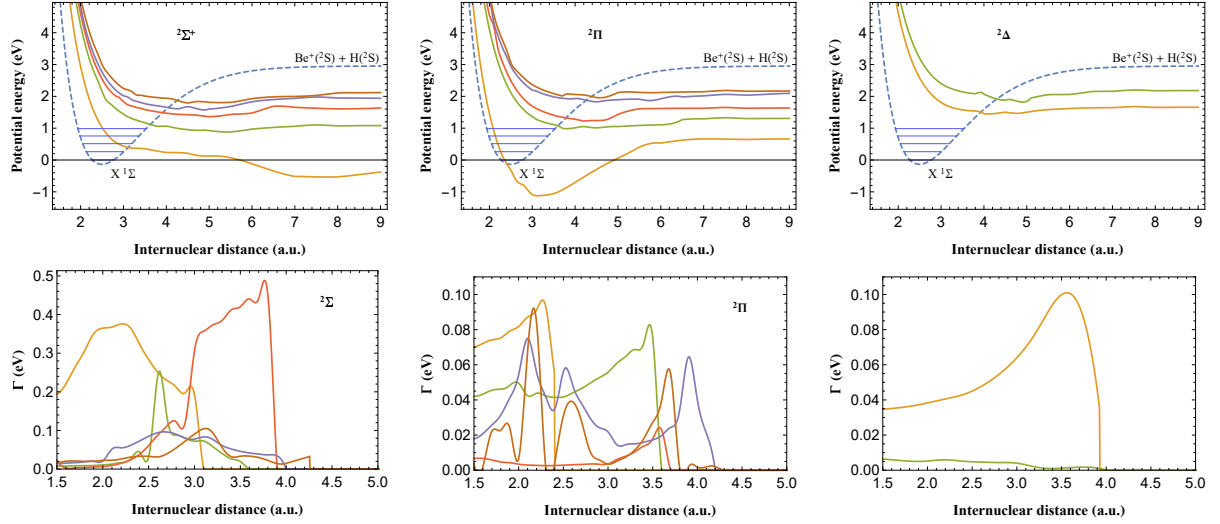
Figure 3.37: Potential energy curves (top line) and widths (bottom line) for BeH** resonant states in $^2\Sigma^+$, $^2\Pi$ and $^2\Delta$ scattering channels for $j^+ = 0$. Dashed line refers to potential energy curve for BeH$^+$ ground electronic state where the first vibrational levels are marked.

v^+	j^+_{max}	v^+	j^+_{max}	v^+	j^+_{max}
0	51	7	39	14	21
1	50	8	37	15	18
2	49	9	35	16	14
3	47	10	32	17	10
4	45	11	30	18	3
5	43	12	27		
6	41	13	24		

Table 3.10: Number of rotational states compatible for each vibrational levels of BeH$^+$.
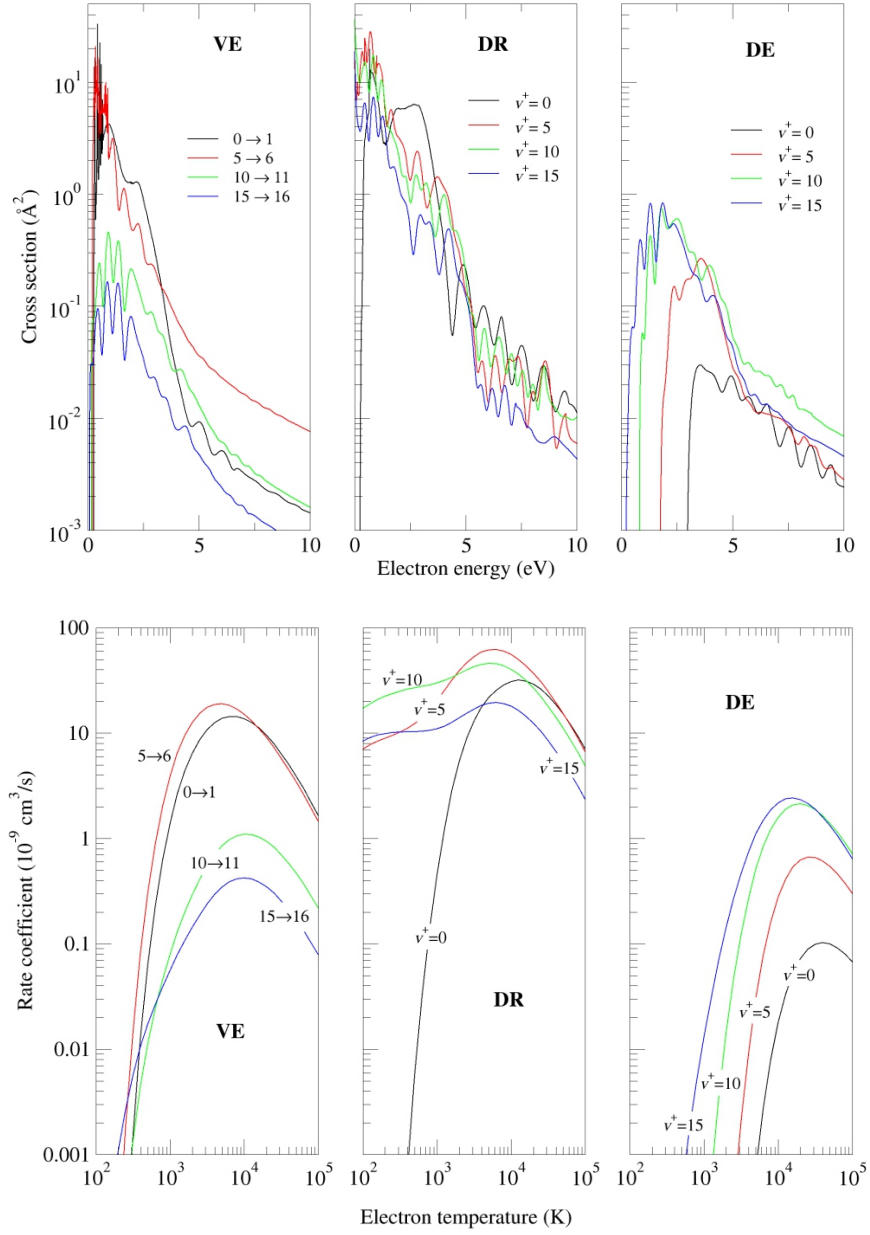
Figure 3.38: Summary on the global cross sections (top row) and the corresponding rate coefficients (lower row) for $j^+ = 0$ and summed over the resonant states for the three precesses considered in the text shown for some selected vibrational excitation (left panel), for dissociative recombination and dissociative excitation (central and right panels) starting from the vibrational levels shown in the figure.
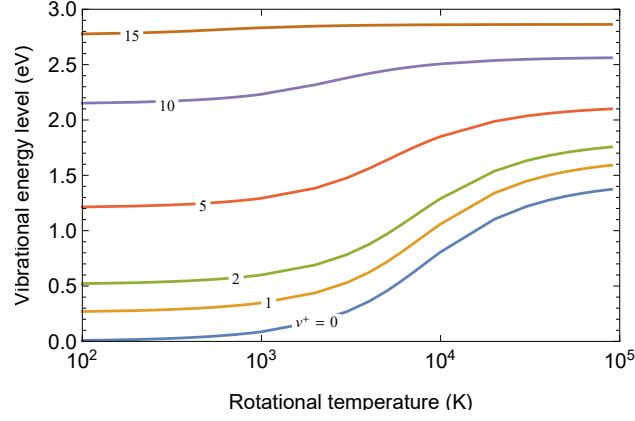
Figure 3.39: Effect of rotational temperature on j-averaged vibrational levels of BeH$^+$.

Figure 3.40: Summary on rotational effects on the cross section of the three processes considered in the text for BeH$^+$. On the top row: the cross sections for rotational quantum numbers $j^+ = 0, 10, 20, 30, 40, 50$ (solid lines); on the bottom row: the j-averaged cross sections (dashed lines), for different rotational temperatures as shown in the panels.

Chapter 4
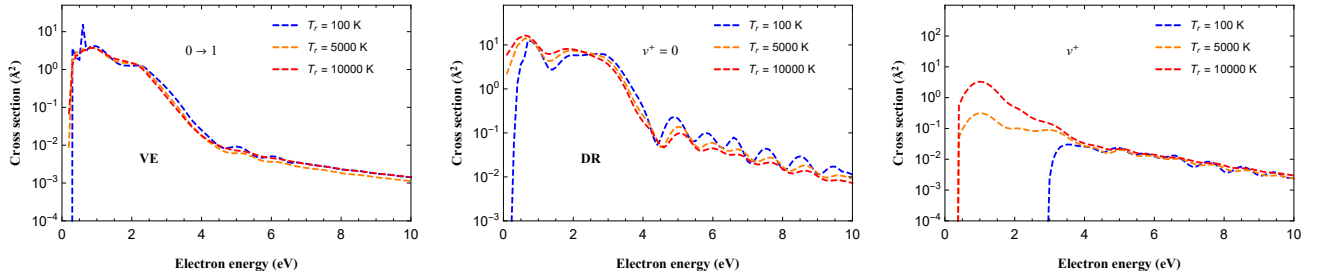
Kinetic modeling in nitrogen-containing plasmas

A lot of work has been presented over the last 40 years aimed at understanding the non-equilibrium vibrational kinetics of non-equilibrium molecular plasmas. Some examples can be found in the papers [15, 163, 164] and references therein. Particular attention has been devoted to the coupling of vibrational and electronic distributions with the electron energy distribution function through the so-called superelastic collisions (also known as second kind collisions) [165, 166]. The treatment of non-equilibrium vibrational and electronic kinetics has become progressively more complex, with many elementary processes included to better model the plasma [52, 167, 168, 169, 170, 171, 172, 173]. Sophisticated models are now available which can be used to understand the properties of nitrogen containing plasmas.

Unfortunately, the available experimental measurements generally characterize average quantities, such as the degree of dissociation and ionization, rather than the more informative vibrational distribution functions (vdf) and electron energy distribution functions (eedf), which remain difficult to measure. The recent measurements of the vdf of nitrogen [174, 175] are limited to vibrational levels with $v < 20$ and thus fail to probe the plateau predicted for the higher lying vibrational levels.

In the present chapter, I discuss some of the results I obtained in molecular plasma modelling. In particular, I will review those articles focusing on nitrogen-containing plasmas. In the Section 4.1 the main theoretical aspects to treat non-equilibrium flows are summarized.

4.1 Master equation formalism

The physical system consists of n chemical species described by m temperatures. Each of k-specie has a translation (T_k^{tr}), vibrational (T_k^{vib}) and electronic excitation (T_k^{exe}) temper-

ature which can be one of the m temperatures. Rotational temperatures are supposed to be in equilibrium at T_k^{tr}. The independent variables for the system are: the global mass density $\rho = M/V$, the mass fractions $y_k = M_k/M$ of the species $k = 1 \ldots n$, the velocity u of the flux and the temperatures T_i, $i = 1 \ldots m$. The conservation equations, *i.e.* the Euler equations, for the system are:

$$\partial_t \rho + \vec{\nabla} \cdot (\rho \vec{u}) = 0 \,, \tag{4.1}$$

$$\partial_t (\rho y_k) + \vec{\nabla} \cdot (\rho y_k \vec{u}) = \dot{\omega}_k \,, \qquad k = 1 \ldots n \,, \tag{4.2}$$

$$\partial_t (\rho \vec{u}) + \vec{\nabla} \cdot (\rho \vec{u} \otimes \vec{u}) = -\vec{\nabla} \cdot \hat{P} \,, \tag{4.3}$$

$$\partial_t (\rho h) + \vec{\nabla} \cdot (\rho h \vec{u}) = 0 \,, \tag{4.4}$$

$$\partial_t (\rho \epsilon(T_i)) + \vec{\nabla} \cdot (\rho \epsilon(T_i) \vec{u}) = \dot{\Omega}(T_i) \,, \qquad i = 2 \ldots m \,. \tag{4.5}$$

respectively for the conservation of global mass, species, momentum, total energy. The equation (4.5) corresponds to the energy conservation for each of $m-1$ extra temperatures. The Eq. (4.2) sometimes is called the "Master Equation".

In the previous equations (4.1)–(4.5), the global mass density ρ is given by:

$$\rho = \frac{n_0}{N_A} \sum_{k=1}^n x_k \, m_k \,, \tag{4.6}$$

where n_0 is the global particle density of the mixture, m_k the molar mass of the specie k and x_k the molar fraction of the specie k related to the mass fraction y_k by:

$$y_k = \frac{x_k \, m_k}{\sum_k x_k \, m_k} \,. \tag{4.7}$$

For the general chemical reaction r:

$$\sum_{k=1}^n \nu_k^r [N_k] \rightleftarrows \sum_{k=1}^n \nu_k'^r [N_k] \,, \tag{4.8}$$

the corresponding source terms, $\dot{\omega}_k^r$, is given by:

$$\dot{\omega}_k^r = \frac{m_k}{N_A} \left(\nu_k'^r - \nu_k^r \right) \left[k^{f,r} \prod_{i=1}^n [N_i]^{\nu_i^r} - k^{b,r} \prod_{i=1}^n [N_i]^{\nu_i'^r} \right] \,, \tag{4.9}$$

where ν_k^r and $\nu_k'^r$ are the stoichiometric coefficients, $[N_k]$ is the particle density of the specie k related to the mass fraction by:

$$[N_k] = y_k \, \rho \, \frac{N_A}{m_k} \,, \tag{4.10}$$

and $k^{f,r}$ ($k^{b,r}$) is the forward (backward) rate constant of the reaction r. The total source term for mass production rate of specie k due to chemical reactions is the sum over the reactions:

$$\dot{\omega}_k = \sum_r \dot{\omega}_k^r \,. \tag{4.11}$$

We note that from Eqs.(4.1) and (4.2) must be:

$$\sum_k \dot{\omega}_k = 0 \,. \tag{4.12}$$

The total pressure $p = \sum_{k=1}^n p_k$ of the mixture is given in term of the partial pressures p_k,

$$p = \sum_{k=1}^n \sum_{i=1}^m \rho y_k r_k \delta(T_k^{tr} - T_i) T_i \,, \tag{4.13}$$

where we defined $r_k = R/m_k$. $h = H/M$ is the total enthalpy per mass unit of the system:

$$h = \sum_{k=1}^n y_k h_k \,, \tag{4.14}$$

where $h_k = H_k/M_k$ is the enthalpy per mass unit of the specie k defined by:

$$
\begin{aligned}
h_k &= \frac{u^2}{2} + \frac{U_k}{M_k} + \frac{p_k}{\rho_k} \\
&= \frac{u^2}{2} + \frac{U_k}{M_k} + r_k T_k^{tr} \,.
\end{aligned}
\tag{4.15}
$$

In writing Eq.(4.15) we assumed all species to have the same drift velocity u and they fill the full volume V. The internal energy per mass unit, U_k/M_k, of specie k is given by:

$$\frac{U_k}{M_k} = \frac{3}{2} r_k T_k^{tr} + U_k^{rot}(T_k^{tr}) + U_k^{vib}(T_k^{vib}) + U_k^{exe}(T_k^{exe}) + h_k^{0f} \,, \tag{4.16}$$

where each contribution is calculated as:

$$U_k^i = \frac{\sum_j g_{j,k} \, \epsilon_{j,k} \, exp(-\frac{\epsilon_{j,k}}{K_B T^i})}{\sum_j g_{j,k} \, exp(-\frac{\epsilon_{j,k}}{K_B T^i})} \,, \tag{4.17}$$

where $\epsilon_{j,k}$ and $g_{j,k}$ are the internal (e.g. vibrational) levels of the specie k. Therefore the total enthalpy per mass unit in Eq.(4.14) becomes:

$$h = \frac{u^2}{2} + \frac{\sum_k U_k}{M} + \frac{\sum_k p_k}{\rho} \,. \tag{4.18}$$

$\epsilon(T_i)$ is the that part of energy from the total enthalpy of the system in equilibrium at temperature T_i, defined as:

$$\epsilon(T_i) = \sum_{k=1}^{n} y_k \epsilon_k(T_i) , \qquad (4.19)$$

and the source terms

$$\dot{\Omega}(T_i) = \sum_k y_k \dot{\Omega}_k(T_i) . \qquad (4.20)$$

After some manipulations, the final equations, for 1-D shock wave, are:

$$\rho u = \text{const} , \qquad (4.21)$$

$$\rho u \, \partial_x y_k = \dot{\omega}_k , \qquad (4.22)$$

$$\left(\frac{\rho u^2}{p} - 1\right) \partial_x u + \sum_i u \frac{\sum_k \rho y_k r_k \delta(T_k^{tr} - T_i)}{p} \partial_x T_i = -\frac{1}{p} \sum_k \dot{\omega}_k r_k T_k^{tr} , \qquad (4.23)$$

$$\rho u^2 \partial_x u + \sum_i \rho u \sum_k y_k \left[c_{P,k}^{tr} \delta(T_k^{tr} - T_i) + c_{V,k}^{vib} \delta(T_k^{vib} - T_i) + c_{V,k}^{exe} \delta(T_k^{exe} - T_i) \right] \partial_x T_i = - \sum_k \dot{\omega}_k h_k , \qquad (4.24)$$

$$\rho u \sum_k y_k \frac{\partial \epsilon_k(T_i)}{\partial T_i} \partial_x T_i = \dot{\Omega}(T_i) - \sum_k \dot{\omega}_k \epsilon_k(T_i) , \qquad (4.25)$$

where $c_{P,k}$ and $c_{V,k}$ are the heat capacities. In Eq. (4.25) if T_i refers to the electron temperature an extra $p_e \partial_x u$ term should be added on LHS due to the ambipolar field, where p_e is the electron partial pressure.

Defining the vector of independent variables $\vec{Y}$:

$$\vec{Y} = \begin{pmatrix} y_k \\ u \\ T_i \end{pmatrix} , \qquad (4.26)$$

the previous equations (4.22)–(4.25) can be summarized in a matrix formalism as:

$$\hat{A}(x, \vec{Y}) \, \partial_x \vec{Y} = \vec{F}(x, \vec{Y}) . \qquad (4.27)$$

The discontinuity at Shock is calculated from conservation equations:

$$\rho u = (\rho u)_0 , \qquad (4.28)$$

$$\rho u^2 + p = (\rho u^2 + p)_0 , \qquad (4.29)$$

$$\sum_k y_k k_y + \frac{u^2}{2} = \left(\sum_k y_k k_y + \frac{u^2}{2} \right)_0 , \qquad (4.30)$$

68

assuming the mass fractions y_k and the temperatures T_i, $i = 2 \ldots m$ kept frozen whereas only the velocity u and temperature T_1 change. $(\cdots)_0$ means quantities calculated before the shock. After some manipulations we have the following equations:

$$\alpha u^2 + \beta u + \gamma T_1 + \delta = 0 \,, \tag{4.31}$$

$$\frac{u^2}{2} + bT_1 - a = 0 \,, \tag{4.32}$$

where the constants are:

$$\alpha = (\rho u)_0 \,, \tag{4.33}$$

$$\beta = (\rho u^2 + p)_0 \,, \tag{4.34}$$

$$\gamma = \sum_{k=1}^{n} (\rho u)_0 y_k r_k \delta(T_k^{tr} - T_i) \,, \tag{4.35}$$

$$\delta = \sum_{i>2} \sum_{k=1}^{n} (\rho u)_0 y_k r_k \delta(T_k^{tr} - T_i) T_i \tag{4.36}$$

$$a = \left(\sum_{k=1}^{n} y_k \left(\frac{5}{2} r_k + R \right) \delta(T_k^{tr} - T_i) T_i + \frac{u^2}{2} \right)_0 \tag{4.37}$$

$$b = \sum_{k=1}^{n} y_k \left(\frac{5}{2} r_k + R \right) \delta(T_k^{tr} - T_i) \tag{4.38}$$

and T_1 and u given from:

$$\left(\alpha - \frac{\gamma}{2b} \right) u^2 + \beta u + \left(\frac{\gamma a}{b} + \delta \right) = 0 \tag{4.39}$$

$$T_1 = \frac{1}{b} \left(a - \frac{u^2}{2} \right) \,. \tag{4.40}$$

4.2 Electron-vibration energy transfer

The ro-vibrational relaxation of $N_2(X\,^1\Sigma_g^+)$ molecules in a background gas composed of $N(^4S_u)$ atoms and free electrons is studied by using an ideal isochoric and isothermic chemical reactor. A rovibrational state-to-state (StS) model is developed to study energy transfer process induced by free electron and atomic collisions.

The full data-set of rate coefficients comprises inelastic and exchange reaction processes due to collisions of $N_2(X\,^1\Sigma_g^+)$-$N(^4S_u)$ as well as inelastic excitation processes, due to electron nitrogen collisions. For the first processes we have used the *ab initio* NASA Ames database [176, 177, 178, 179], while for the electron-induced processes the model relies on the R-matrix calculations presented in the section 3.1. To give an idea of the relative
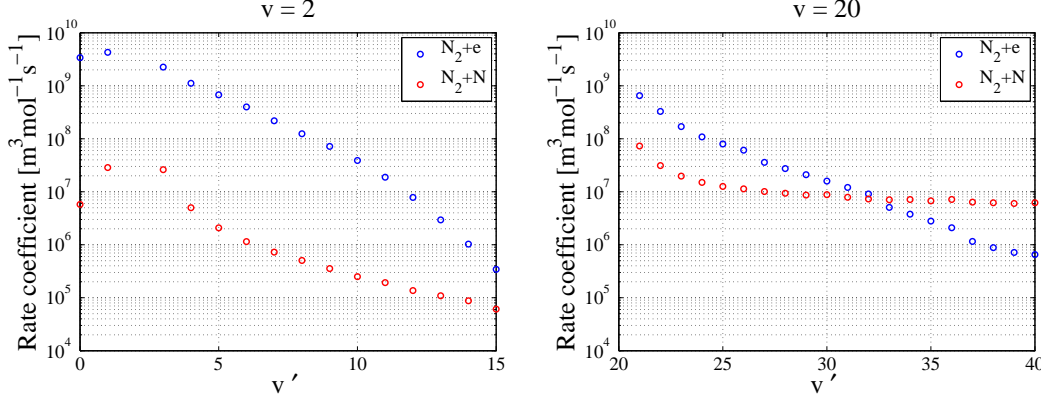
Figure 4.1: Comparison of e + $N_2(X\,^1\Sigma_g^+)$ and $N(^4S_u) + N_2(X\,^1\Sigma_g^+)$ vibrational excitation rate coefficients for $T = T_e = 10.000$ K, and $J = 0$. (On the left) The initial vibrational state is $v = 2$. (On the right) the initial vibrational state is $v = 20$.

importance of the $N_2(X\,^1\Sigma_g^+)$-$N(^4S_u)$ and $N_2(X\,^1\Sigma_g^+)$-e^- processes, Figure (4.1) shows a comparison in terms of reaction rate coefficients for a fixed electron and heavy particle translational and rotational temperature assumed in thermal equilibrium with each other at 10.000 K. In the figure, we show results for the low-lying (*e.g.*, $v=2$) and high-lying initial vibrational levels (*e.g.*, $v=20$). At low vibrational energies, there is a significant enhancement of the N_2-e^- vibration excitation cross sections due to the well-known 2.3 eV $^2\Pi_g$ resonance [19, 63]. As a result, the $N_2(X\,^1\Sigma_g^+)$-e^- vibrational excitation rate coefficients are several orders of magnitude larger than the corresponding $N(^4S_u)$ - $N_2(X\,^1\Sigma_g^+)$ vibrational excitation rates. For the high vibrational levels, however, the trend is reverted. The reason is twofold: Firstly, the effect of the resonance becomes less important due to the larger differences in the energies between $N_2(X\,^1\Sigma_g^+)$ and the $N_2^-(^2\Pi_g)$ energies for the higher vibrational levels; secondly, the heavy particle excitation processes become more efficient, as the high lying vibrational levels are closely spaced.

We wish to investigate the behavior of nitrogen molecules in their electronic ground state when subjected to sudden heating in an ideal chemical reactor. We make the following assumptions:

- The reactor is plunged into a thermal bath maintained at constant temperature T.

- The initial number density of the gas inside of the reactor is set to $n = 2.41546 \times 10^{24}$ m^{-3}. For this value, the translational energy mode of the atoms and molecules is assumed to follow a Maxwell-Boltzmann distribution at the temperature T of the thermal bath. This is equivalent to an initial pressure of 10.000 Pa.

- At the beginning of the numerical experiment, the population of the rovibrational

energy levels is assumed to follow a Maxwell-Boltzmann distribution at the internal temperature $T_0^I = 300$ K.

- The volume of the chemical reactor is kept constant during the experiment and the thermodynamic system is closed (no mass exchange with surrounding environment).

- The dissociation and ionization processes are ignored, and we assume that the molecule-molecule collisions do not participate in the excitation processes.

- The molar fractions of nitrogen atoms and free electrons are fixed to the value of $x_N=x_e=5\%$ and it is constant throughout the relaxation.

The rotation and vibration of molecules in the gas can be described by means of a STS approach. In this case, the temporal evolution of the populations of molecules in a particular rovibrational energy level (v,J), is obtained by solving a system of kinetic equations, also referred to as Master Equations.

We study the kinetics of nitrogen molecules, $N_2(X\,^1\Sigma_g^+)$, relaxing in a background gas composed of electrons and nitrogen atoms for heavy particles temperatures ranging from 10.000 to 30.000 K. At the beginning of the simulation, the rotational and vibrational levels of $N_2(X\,^1\Sigma_g^+)$ are populated according to a Maxwell-Boltzmann distribution at T_0^I = 300 K. Initially, the velocity of the free electrons is assumed to be Maxwellian and in thermal equilibrium with T_0^I. For this condition, the bulk of the nitrogen molecules occupy the lowest several rovibrational energy levels. With time, the random motion of heavy and light particles, brings about collisions, thus enabling the redistribution of the heavy kinetic energy into rotation, vibration and free-electron energies.

The free-electron temperature as well as the vibrational, rotational and internal energies are shown in Figure (4.2). The two plots describe the relaxation of the $N_2(X\,^1\Sigma_g^+)$ molecules for two different test conditions: a low temperature case, where $T = 10.000$ K, shown on the left; and a higher temperature case, where $T = 30.000$ K, shown on the right.

In the low temperature case, the relaxation time scales of the energy modes [1] differ by an order of magnitude, with rotation being the fastest process to relax, followed respectively by free-electron and vibration.

The inelastic scattering process of the molecules with the nitrogen atoms controls their rotational excitation. In fact, due to their small mass, the electrons cannot significantly influence the rotational motion of the molecular nuclei. Thus, the rotational kinetics appears completely decoupled from the vibrational and the free-electron relaxation. The behavior of the vibrational relaxation is more complicated. In the early stages, the relaxation is controlled by the $N_2(X\,^1\Sigma_g^+)$-$N(^4S_u)$ collisional processes, and appears to be significantly slower than the rotational relaxation. As the molecules become vibrationally excited, they

---

[1]Here the relaxation time is defined as the time required by the generic energy mode to reach 64 % of their final equilibrium value.
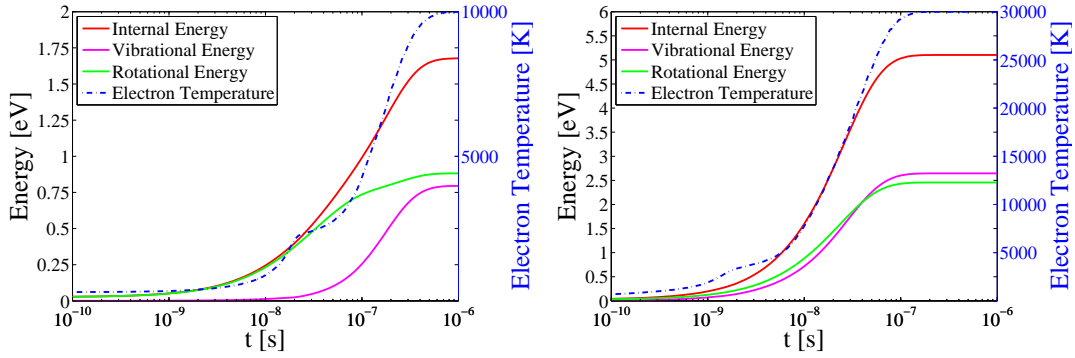
Figure 4.2: Time evolution of the averaged rotational $e_{N_2}^R$ and vibrational energies, $e_{N_2}^V$ and the electron temperature T^e. The collisional processes included are $N_2(X\,^1\Sigma_g^+) - \epsilon$ and $N_2(X\,^1\Sigma_g^+) - N(^4S_u)$. (On the left) The heat-bath temperature was set to $T = 10.000$ K; (On the right) the heat-bath temperature was set to $T = 30.000$ K. The purple and the green lines indicate $e_{N_2}^V$ and $e_{N_2}^R$ respectively. $e_{N_2}^I$ is plotted in red. The free electron temperature is shown in blue.

transfer part of their energy to the electrons, because of the inelastic deactivation processes (*i.e.*, $N_2(X\,^1\Sigma_g^+)$-e^-). Thus, the inelastic energy transfer processes involving $N_2(X\,^1\Sigma_g^+)$-e^- collisions are ultimately responsible of the thermalization of electrons and control the electron temperature.

The evolution of the free electron temperature is characterized by an initial exponential increase, followed by a plateau, and by the fast relaxation to the final equilibrium value. The presence of the plateau in the free electron temperature curve, is explained by the active role played by the electrons in the excitation of the nitrogen molecules. Electrons can efficiently promote the excitation of the vibrational levels of the molecules, however, this process quickly depletes their energy, thus cooling their temperature. The presence of this feedback process limits the ability of the electrons to influence the vibrational relaxation process.

To gain insights on the dynamics of the relaxation of the system, we have computed the population of the internal energy levels at four different times in the relaxation: the initial time; the time t $= 10^{-8}$ s, when the excitation of the free electrons becomes significant; the time t $= 10^{-7}$ s, when a plateau is observed in the free electron temperature; and the time t $= 10^{-6}$ s, when the final equilibrium condition is reached. The four different distributions are shown in Figure (4.3). In the figure, the states characterized by the same vibrational quantum number are indicated with the same color.

At the beginning and at the end of the simulation the population of the rovibrational levels, as expected, follows a Maxwell-Boltzmann distribution at the initial and final tem-
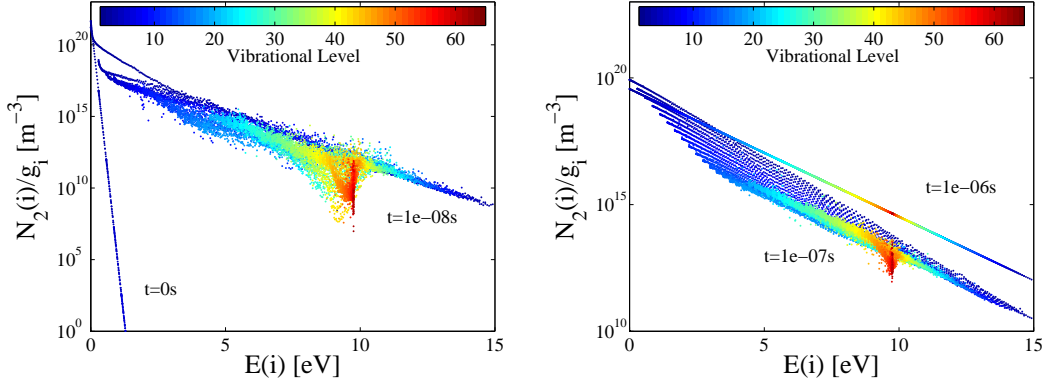
Figure 4.3: $T = 10.000$ K case: Time evolution of the $N_2(X^1\Sigma_g^+)$ rovibrational population distribution. Both $N_2(X^1\Sigma_g^+) - \epsilon$ and $N_2(X^1\Sigma_g^+) - N(^4S_u)$ processes are included in the simulation. Color coatings indicate levels characterized by the same quantum number. The initial conditions are: $T = 10.000$ K, $T_0^I = T_0^R = T_0^e = 300$ K, $x_e = x_N = 5\%$.

perature respectively. At intermediate times, the two distributions strongly depart from a Maxwell-Boltzmann distribution. In the early stages of the relaxation (e.g., $\approx 10^{-8}$ s), the population distribution is divided in distinct strands characterized by different vibrational quantum number. Within each strand, the low-lying rovibrational levels follow a Maxwell-Boltzmann distribution at the initial temperature T_0^I, while the higher states are excited due to the inelastic collisions with the nitrogen atoms. Similar distortion of the distribution has been discussed by Panesi et al. [180] The behavior of the high lying energy levels strongly depends on their quantum state and can be divided in two categories: the ones characterized by high J and low v quantum numbers, indicated in blue in the figure; and the levels characterized by large v and small J, indicated in red in the figure. The time evolution of these two groups of molecules appears significantly different. The former tend to be more populated, and their distribution gradually merges with the distribution of the low-lying levels, while the latter group appears to be drastically underpopulated. The reason for this behavior can be found in the dynamics of the excitation process. Initially, collision excite the molecules, according to a rotational ladder climbing process [180, 181]. However, population exchange between the rotationally excited molecules and the vibrationally excited ones is inefficient due to the differences in the quantum mechanical states.

Initially, the electrons cannot actively contribute to the excitation, since they are cold (e.g., $T_e = 300$ K). However, as they absorb energy from the molecules, their contribution to the excitation process becomes noticeable. At the end of the plateau in electron temperature curve (e.g., $\approx 10^{-7}$ s), the internal population function appears to be dissected in a series of partial Maxwell-Boltzmann distributions. The population within each mode is characterized by the same vibrational quantum number v, and can be described by a

rotational temperature T_v^R. A comparison of the vibrational and rotational distribution shows how the rotational temperature is significantly higher than the vibrational one. It is important to note that the multimodal character of the distribution is not restricted to the low lying levels, as observed in the analysis of the $N_2(X\,^1\Sigma_g^+) - N(^4S_u)$ case [180] but it spans the entire range of energies from the low-lying to the high-lying levels.

In the high temperature case, shown in Figure (4.2), rotation and vibration relax at similar rate, thus implying the existence of a unique internal temperature. The situation described here is often observed in the post shock relaxation region encountered during high speed atmospheric entry [180]. Similarly to the low temperature case, the vibrational relaxation is controlled by the heavy particles impact excitation processes, and the deactivation of excited nitrogen molecules controls the dynamics of the free electrons. The contribution of the free electron kinetics to the excitation of vibration is hindered by the feedback process, which lower the temperature of the free electrons, thus justifying the presence of the plateau.

4.3   Non-equilibrium dissociation mechanism

Despite its apparent simplicity, the dissociation rate is very difficult to be determined experimentally while theoretical calculations, based on semi-empirical electron-molecule dissociation cross sections, fails in reproducing experimental dissociation rates of simple molecules. This point was first emphasized by the Polak group [182], in the 70s, who showed that the experimental dissociation rate of nitrogen in glow discharges at low E/N can not be reproduced by direct electron impact dissociation involving the vibrational ground state of nitrogen (see also Ref. [183]). These experimental findings induced the plasma community to develop sophisticated theoretical models to explain the dissociation rate of diatomic molecules under electrical discharges beyond the direct impact dissociation. In particular a pure vibrational mechanism (PVM) [184, 185, 186] was developed, based on a three step mechanism: (i) introduction of vibrational quanta by resonant electron vibration excitation process (eV); (ii) redistribution of the quanta by vibration-vibration (VV) and vibration-translation (VT) energy exchange processes; (iii) overcoming by the same processes of the last vibrational level linked to a pseudo-level located in the continuum, *i.e.* miming the dissociation process. The corresponding PVM rates were found orders of magnitude higher than the corresponding rates by direct electron-impact from the ground vibrational level $v=0$. Some of the hypotheses contained in these results *i.e.* Maxwell distribution function for electrons and direct electron dissociation from $v=0$ were eliminated and a direct dissociation mechanism from all vibrational levels was considered [165]. In any case the vibrational distribution of nitrogen presented a long plateau such as to promote dissociation directly from PVM and indirectly by a direct electronic mechanism (DEM) including transitions from all vibrational levels.
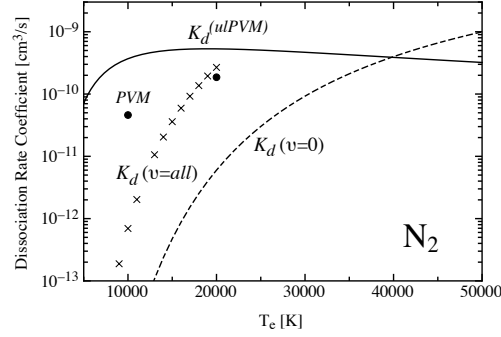
Figure 4.4: Nitrogen dissociation rate as a function of electron temperature calculated according to different models. (Solid line) $K_d^{(ulPVM)}$ from accurate eV rates taken from Section 3.1, (*dashed line*) dissociation rate from $\upsilon=0$ from recommended cross section by Cosby [191], (*crosses*) global dissociation rate from Park [6], (*Close circles*) pure vibrational mechanism PVM [184, 185, 186].

These results however were based on the knowledge, poor at that time, of the relevant cross sections. In particular the $(VT)_a$ rates involving nitrogen atoms were considered equal to the corresponding ones involving nitrogen molecules neglecting also multi-quantum transitions. Moreover, the eV rates were estimated, by crude scaling law from the known eV rates linking the first 8 levels. It should be noted that these results have been obtained considering 45 vibrational levels in nitrogen, a problem solved in the recently calculated rates and cross sections.

Inclusion of more realistic $(VT)_a$ rates from atomic nitrogen (including also vibrational multi-quantum transitions) was attempted many years ago by Armenise *et al.* [187]. The main result of this study was the practical disappearance of PVM in dissociating nitrogen mainly due to a new set of $(VT)_a$ rates. These rates are continuously updated especially for the processes involving low-lying vibrational levels important for the definition of a vibrational temperature [188, 189]. Insertion of these $(VT)_a$ rates in the kinetic model confirmed the impossibility of PVM mechanisms based on the last vibrational level of the molecule [190]. The aim of work is to reconsider the role of vibrational excitation in affecting the dissociation rates of simple molecules in plasmas sustained by low reduced electric fields E/N. Under these conditions the energy gained by electrons is mainly lost in pumping vibrational energy in the molecule through resonant e-V processes promoting chemical processes activated by the vibrational energy (PVM-like kinetic schemes).

Before examining the model results we want to compare old results obtained (*i*) by PVM; (*ii*) by the direct electron-impact dissociation from $\upsilon=0$ obtained by using the experimental Cosby cross sections [191]; (*iii*) by correcting the experimental electron-impact rates by a factor of 70 to take into account the role of vibrational excited molecules (Park's model)

[192] and (*iv*) by an upper limit of pure vibrational mechanism (*ulPVM*) [14]. In this last case we get the rate as a balance between the vibrational quanta introduced by eV processes and the loss of vibrational quanta by the dissociation process i.e.:

$$K_d^{(ulPVM)} = \frac{\sum_{v=1}^{v_{\max}} v K_{eV}(0 \to v)}{v_{\max}} , \qquad (4.41)$$

where $K_{eV}(0 \to v)$ is the rate coefficient of electron impact excitation process,

$$e + N_2(v = 0) \to N_2^- \to e + N_2(v) \qquad (4.42)$$
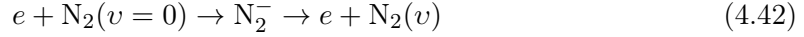
$v_{\max} = 67$ is the number of vibrational states supported by the potential well of the N_2 ground state. Equation 4.41 is derived from the balance of the input of vibrational quanta by eV processes and the corresponding loss by dissociation (every dissociation event needs 67 vibrational quanta), *i.e.* no loss of vibrational quanta occur through VT relaxation. All the rates reported in Fig. 4.4 have been obtained by considering a Maxwell distribution function for electrons and the complete set of eV cross sections from Section 3.1. Inspection of Fig. 4.4 shows that $K_d^{(ulPVM)}$ is orders of magnitude higher than the experimental rate from $v = 0$, $K_d^{\exp}$, in the electron temperature range $7500 < T_e < 30000$ K. In this temperature range $K_d^{(ulPVM)}$ is larger than the rate from the pure vibrational mechanism, which considers a non-equilibrium vibrational kinetics including VV, VT and eV processes and a ladder climbing model for the dissociation process. $K_d^{(ulPVM)}$ is also larger than the corrected rates estimated by Park by increasing the $v = 0$ contribution by a factor of 70.

Let us now consider the results obtained by our time dependent model. We have run our time dependent equations at fixed electron density (molar fraction $\chi_e = 10^{-6}$), pressure $p = 5.6$ torr and gas temperature ($T = 1000$ K). These conditions roughly reproduce the experimental conditions of Polak *et al.* [182]. The results of this model are time-dependent so that we can estimate the total dissociation rate at short times (*cold gas* approximation) and at longer times (*hot gas* approximation). To this end we select $t = 10^{-7}$ s for the first case and $t = 10^{-1}$ s for the second one. In the first case we have only the contribution from $v = 0$ estimated by the $v = 0$ electron-impact dissociation cross section and an EEDF depending only on E/N (*cold gas* approximation). At the selected longer time we have an EEDF, which depends not only on E/N but also on the population of vibrational and electronic states through the action of the relevant superelastic collisions [193, 167]. The vibrational distribution enters also in the total dissociation rate. We report in Fig. 4.5 $K_d(v = 0)$ and

$$K_d^{kin} = \sum_{v=0}^{v_{\max}} k(v) \frac{N_v}{N_{\text{tot}}} , \qquad (4.43)$$

as a function of E/N and compare these values with the experimental values of Polak *et al.* [182].
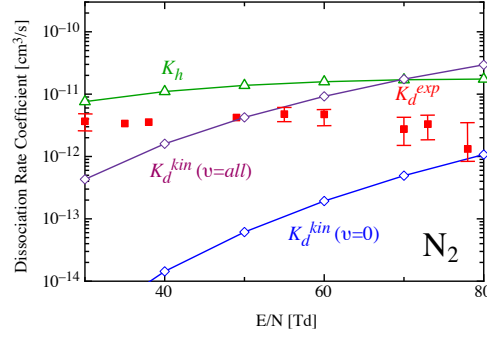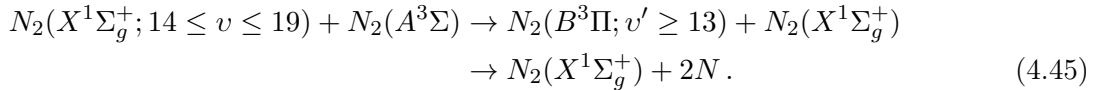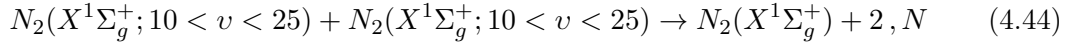
Figure 4.5: Nitrogen dissociation rates as a function of reduced electric field E/N, at p=5.6 torr, calculated according to different models. (*close squares*) experimental dissociation rate with error bars [182], (*open diamonds*) present results from kinetics with dissociation from $v = 0$ and from all vibrational levels ($t = 10^{-3}$ s in the time evolution), (*close circles*) pure vibrational mechanism PVM.

As expected $K_d^{kin}(v = 0)$ and $K_d(v = 0)$ are the same at $t = 10^{-7}$ s being orders of magnitude lower than the corresponding values at $t = 10^{-1}$ s, the last reported in Fig. 4.5. In this case the role of vibrational excited states is well evident bringing the theoretical results in the same scale of experimental ones for $E/N > 60$ Td. Theoretical and experimental results however present a strong disagreement for $E/N < 60$ Td. In this last case the theoretical results not only are orders of magnitude lower than the experimental ones but also do not reproduce the flat behavior of the experimental dissociation rate as a function of E/N. A flat behaviour is indeed presented by the quantity $K_d^{(ulPVM)}$ as a function of T_e (Fig. 4.4) (*i.e.* to a first approximation as a function of E/N) even though the corresponding theoretical values are more than two orders of magnitude higher than the experimental values. Moreover the old PVM rates reported in Ref. [165] for E/N=30 and 60 Td seem to fill the gap between theoretical and experimental values shown in Fig. 4.5.

Going beyond the possibility of the dissociation from the last bound level of nitrogen we could assume a vibrational mechanism [167, 194] involving two vibrationally excited molecules *i.e.*,

$$N_2(X^1\Sigma_g^+; 10 < v < 25) + N_2(X^1\Sigma_g^+; 10 < v < 25) \rightarrow N_2(X^1\Sigma_g^+) + 2\,, N \qquad (4.44)$$
$$N_2(X^1\Sigma_g^+; 14 \leq v \leq 19) + N_2(A^3\Sigma) \rightarrow N_2(B^3\Pi; v' \geq 13) + N_2(X^1\Sigma_g^+)$$
$$\rightarrow N_2(X^1\Sigma_g^+) + 2N\,. \qquad (4.45)$$

The corresponding rate coefficients can be calculated as [194],

$$k_{N_2(v)+N_2(v)} = 3.5\,10^{-15}\ \text{cm}^3/\text{s}\,, \qquad (4.46)$$
$$k_{N_2(v)+N_2(A)} = 4.5\,10^{-11}\exp(-1765/T_g)\ \text{cm}^3/\text{s}\,. \qquad (4.47)$$

This mechanism first proposed by Guerra *et al.* [194] and then used by Dyatko *et al.* [195] and by Capitelli *et al.* [193] can be ascribed to the PVM-like mechanism although using the intermediate portion of vdf as well as of metastable nitrogen molecules instead of the last vibrational level as in the original PVM level. Their sum at the stationary conditions ($t \sim 0.1 - 1$ s) have been reported in 4.5 and compared with the different models and with the experimental results. The rates are in this case in qualitative agreement with the experimental ones in all the E/N range. In particular they fill the gap between experimental values and theoretical ones based on electron impact dissociation rates for $E/N < 60$ Td.

4.4 Electron energy distribution function in nitrogen discharges

The formation of the electron energy distribution function in nanosecond atmospheric nitrogen discharges is investigated by means of self-consistent solution of the chemical kinetics and the Boltzmann equation for free electrons. The post-discharge phase is followed to few microseconds. The model is formulated in order to investigate the role of the cross section set, focusing on the vibrational-excitation by electron-impact through resonant channel. Four different cross section sets are considered, one based on internally consistent vibrational-excitation calculations, extended to the whole vibrational ladder, and the others obtained by applying commonly used scaling-laws. In particular, we focus our attention on the formation of the eedf under discharge and post-discharge conditions, and the creation of structures in the eedf due to superelastic collisions from vibrationally and electronically excited states. Particular emphasis is given to the dependence of computed microscopic and macroscopic quantities on the electron-molecule resonant vibrational-excitation cross sections.

As already noted, a complete, internally-consistent, data set of cross sections for electron impact vibrational-excitation was not previously available. To complete the available data different scaling-laws have been applied. The first scaling-law we consider was reported in Ref. [196] and was obtained by fitting the data calculated by Huo *et al.* [66]. The resulting expression gives rate coefficients for transitions involving excited vibrational levels, starting from the rate for the $v = 0$ level:

$$K_{v,v+n} = \frac{K_{0,n}}{1 + av},$$
(4.48)

where $a = 0.15$. Another simple scaling-law, reported in Ref. [169], is given by:

$$\sigma_{v,v+n}(\epsilon) = \sigma_{0,n}(\epsilon - \Delta\epsilon),$$
(4.49)

where $\Delta\epsilon$ is the energy difference due to the anharmonicity of the vibrational ladder:

$$\Delta\epsilon = \epsilon_n - \epsilon_0 + \epsilon_{n+v} - \epsilon_v.$$
(4.50)

Only transitions with $v + n < 10$ have been considered. A similar approach has been used in Refs. [165, 197], where $\Delta\epsilon$ were neglected. A third approach was obtained by extending the scaling-law for V-Tm rates for harmonic oscillator to the electron impact rates *i.e.* it was applied a Laundau-Teller model to the e-V rates:

$$K_{v,v+1} = (v + 1)K_{0,1} \, . \tag{4.51}$$

The kinetic model used in this paper has been described in detail elsewhere [198, 199, 193, 200, 111]. Briefly it consists of homogeneous kinetic equations coupling the non-equilibrium vibrational and electronically-excited state kinetics with the Boltzmann equation for the eedf. The processes induced by heavy particle collisions are listed in Table 1 of Ref. [193]. In particular, the processes coupling the vdf with electronically excited states and the chemical processes (dissociation and ionization) involving electronically excited states should be noted. The list of electron-impact transitions with vibrationally excited N_2 molecules is reported in Table 2 of Ref. [193].

The coupling between the chemical kinetics and the Boltzmann equation for free electrons is self-consistent, *i.e.* at each time step the level population and the gas composition give the input quantities for the Boltzmann equation and the rate coefficients for the electron induced processes are calculated from the actual eedf. Inelastic and superelastic collisions involving vibrationally and electronically excited states and free electrons are fully considered in this model. Also electron-electron collisions are included using an efficient algorithm described in Ref. [201]. The N_2 vibrational ladder includes 68 levels. This requires a rescaling of the old V-V and V-Tm rates which are based on 46 vibrational levels.

To solve the coupled problem we impose initial conditions for all the relevant quantities. In particular a Boltzmann distribution function at $T = 500$ K was selected for vdf and a Maxwell distribution function at the same temperature was selected for eedf. An initial molar fraction of electrons of $\chi_e = 10^{-10}$ was selected while pressure and gas temperature were kept at $p = 1$ bar and $T_g = 500$ K. Moreover, an uniform reduced electric field of $E/N = 200$ Td was applied for 3 ns and the simulation was followed in the post-discharge $(E/N = 0)$ for up to few microseconds *i.e.* we are using an Heavyside-tipe temporal evolution for E/N. The simulation is therefore typical for a nanosecond high voltage-high pressure discharge followed by a post-discharge regime typically met in plasma-assisted combustion. This kind of simulation can be justified in the framework of the aim of the present paper mainly devoted to the understanding of the role of different scaling laws in the e-V cross sections. More realistic E/N forms derived from the experiments [9, 202, 203] including a rise time of the applied voltage followed by a plateau as well as more complicated forms are left to future work.

We consider four test cases, see Table 4.1, based on the use of different scaling-laws for generating the electron-collision vibrational-excitation cross sections and on the numerically calculated data in Ref. [37, 39]. Cross sections for all the other processes, including the heavy

Case	Set of cross sections considered
A	Scaling-law of Eq. (4.48) is applied to the cross sections [196]
B	Scaling-law of Eq. (4.49) is used to calculate cross sections up to $v = 10$ [169]
C	Scaling-law of Eq. (4.51) is applied to the cross sections
D	Full set of cross sections taken from Ref. [37, 39]

Table 4.1: Scheme of the models used in the calculations.

particle kinetics, are the same for all the four cases. It should be noted that only models A and D include all the transitions between vibrational states, while model C considers transitions for levels with $v \leq 10$ and single-quantum excitations only.

Before examining the results we estimate the characteristic relaxation times for the eedf and vdf. The eedf, neglecting vibrationally excited molecules, reaches a quasi-stationary state in a timescale of the order,

$$t_{qse} = (N K_{eV})^{-1} \approx 0.3 \text{ ns}, \tag{4.52}$$

where $N = 1.52 \times 10^{19}$ cm^{-3} is the number density of heavy particles at $p = 1$ bar and $T = 500$ K and $K_{eV} \approx 2 \times 10^{-8}$ cm^{-3} is the rate coefficient for pumping vibrational energy in the system at $E/N = 200$ Td including all transitions from $v = 0$.

The eedf starts to be affected by the presence of vibrationally excited states, as well as electronically excited states, when their population starts to be important. As an example, the vibrational energy supplied by electron impact is proportional to the electron density times the e-V rate; therefore, by considering the maximum value obtained for the electron density ($n_e \approx 1.5 \times 10^{16}$ cm^{-3}), the characteristic time for vibrational excitation is given by:

$$t_{qsv} = (n_e K_{eV})^{-1} \approx 3.3 \text{ ns}. \tag{4.53}$$

We approximately recover these times in Fig. 4.6(a) where the average energy of electrons is shown as a function of time for models A to D.

We start by discussing macroscopic quantities which can be useful for understanding the behaviour of the vdf and eedf under discharge and post-discharge conditions. Figure 4.6(a), as already noted, reports the time evolution of the electron average energy calculated from the eedf as a function of the different models. We can see that in the range 0.1–1 ns the mean electron energy remains constant which is typical of an eedf in the cold gas approximation, *i.e.* without the action of superelastic collisions, while the energy undergoes a sudden increase in the time interval 1–3 ns due to the excitation of vibrational and electronic states. For $t = 3$ ns, the electron mean energy abruptly decreases as the applied field is switched off. For $t > 3$ ns, the mean electron energy is sustained by the vibrational and electronic energy content of molecules, which through superelastic collisions, heat cold electrons. Our results depend strongly on the model used for the electron-molecule cross sections, models
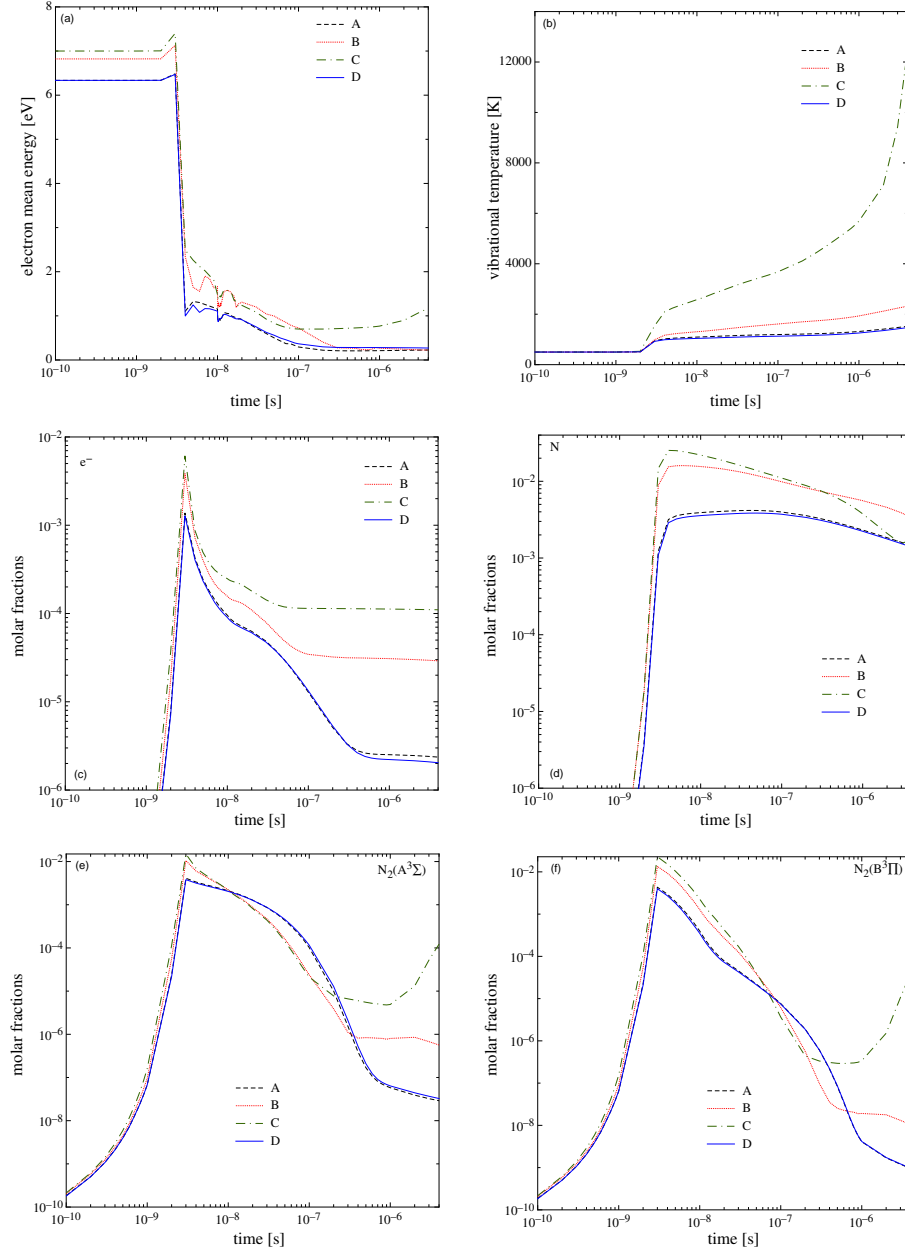
Figure 4.6: Time evolution of (a) mean electron energy; (b) nitrogen vibrational temperature; (c) free electrons molar fraction; (d) nitrogen atoms molar fraction; (e) and (f) molar fraction of N_2 triplet states for the four models considered.

81

A and D predict values of the average energies lower than the corresponding ones from models B and C. The differences in the average energies for the four models can be recovered from the corresponding differences in the vibrational temperature calculated from the first two vibrational levels (see Fig. 4.6(b)). We note that case C deviates from the results of cases A, B and D mainly due to the poor representation of the vibrational excitation with the scaling-law which generates much pumped vibrational distribution functions (see Fig. 4.7). These differences are important under post-discharge condition but remain negligible during the discharge. Inspection of the results shows similarities between the mean electron energy obtained from the four models. The vibrational temperature initially shows a quasi-stationary value, then grows for nearly 3 ns, where the mean electron energy shows a peak. In the post-discharge, the vibrational temperature still increases, unlike the mean electron energy, as it is sustained by chemical processes (recombination) and electronically excited states. Note that the temporal trend of 1-0 vibrational temperature is practically the same as the energy stored in the vibrational mode. In the long time range ($10^{-4} - 10^{-3}$ s) model B and C show a decrease of the vibrational energy, while for models A and D the cooling phase is moved to longer times. At longer times the vibrational temperature will converge to the gas temperature.

Figures 4.6(c) and (d) report the time evolution of free electron and atomic nitrogen molar fractions. Again models A and D give very similar results while models B and C predict a much higher concentrations of electrons and nitrogen atoms due to the corresponding differences in eedf as well as in the electron density. In particular the electron density is affected by electron impact ionization collisions involving the plateau of the vibrational distribution functions which are much more pumped in the cases B and C (see Fig. 4.7). The lower recombination rates of cases B and C compared with the cases A and D are probably due to additional ionization channels promoted by the plateau of the vibrational distribution function as well by electron impact collisions with electronically excited states. The behaviour of the two triplets of nitrogen molecules shown in Fig. 4.6(e) and (f) is also interesting: their concentration follows the same trend as the electron density and reaches a maximum value at the end of the ns discharge. Large differences are observed for $t > 1$ μs where models B and C predict much higher concentrations due to more effective recombination. The behaviour of the two triplets of nitrogen molecules is also interesting: their concentration follows the same trend as the electron density under discharge conditions reaching a maximum value at the end of the ns pulse. Large differences are observed for $t > 1$ μs where models B and C predict much higher concentrations as a consequence of 3-body N atom recombination forming $N_2(B)$ (and then $N_2(A)$ through radiative decay). Therefore $N_2(A)$ and $N_2(B)$ states follow the behaviour of nitrogen atoms as reported in Fig. 4.6(d).

Figure 4.7 shows the behaviour of the vdf obtained by the four models at different characteristic times: (a) at the end of the discharge pulse; (b) at $t = 10$ ns; and (c) at
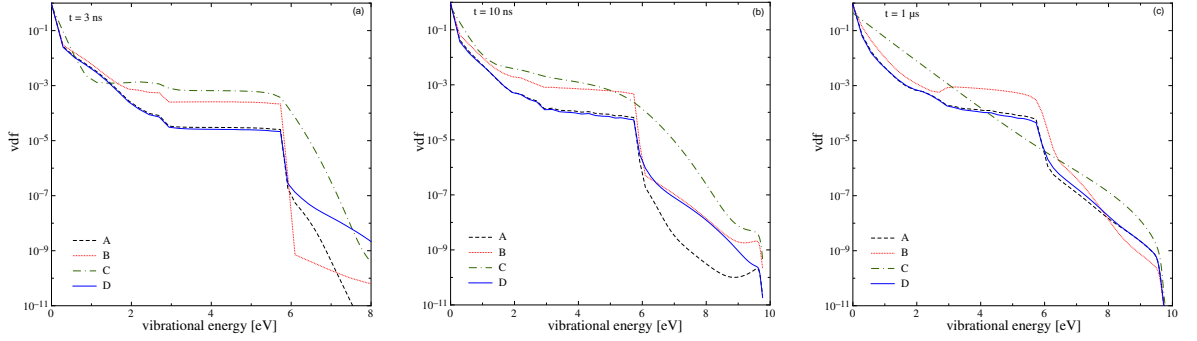
Figure 4.7: Vibrational distributions function of N_2 molecules at three characteristic times and for the four models considered in the text.
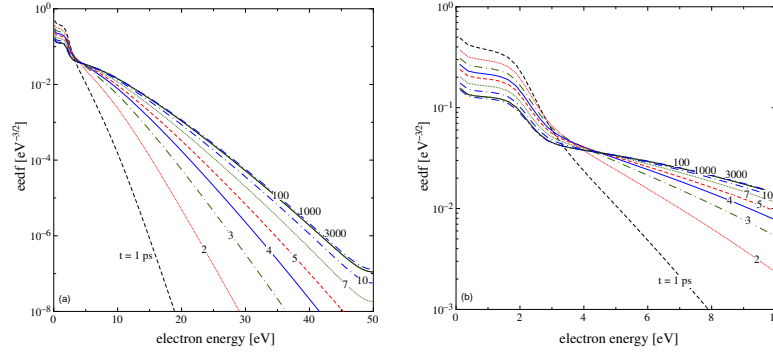

Figure 4.8: (a) Time evolution of eedf under discharge conditions according to model D. (b) The same plot as in (a) but in the energy range 0–10 eV.

$t = 1$ μs in the post-discharge. Models A and D give similar vdfs up to 6 eV, for $t = 3$ and 10 ns, but predict large differences above 6 eV. This behaviour reflects the limitations of the scaling-law of Eq. (4.48). Models B and C behave similarly up to 10 ns. At 1 μs, model C predicts a quasi-Boltzmann distribution but model B shows a well-developed plateau, in line with models A and D, but at much higher v than in these last cases.

Let us now consider the time evolution of eedf under discharge and post discharge conditions. Figure 4.8 illustrates the situation during the discharge. The evolution of the eedf towards a quasi-stationary state is rather regular. After 0.1 ns, the eedf reaches a quasi-stationary value and, in this regime, superelastic collisions do not affect the distribution due to the high value of the electron energy. As shown in Fig. 4.9, the four models give small differences in the eedf, especially in the low-energy region, being dominated by e-V inelastic processes. The situation completely changes in the post-discharge regime where the decrease of average energy enhances the role of superelastic collisions from electronic
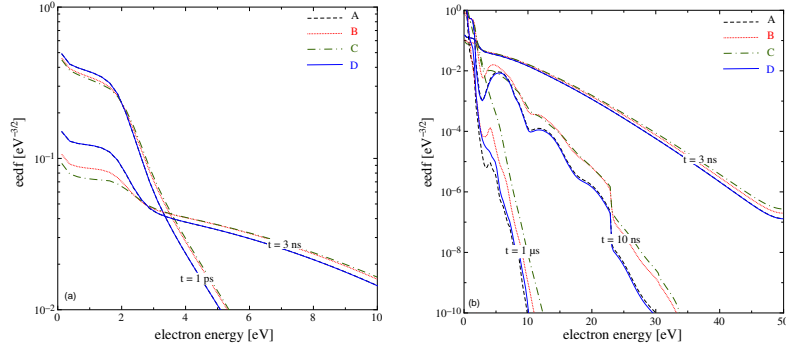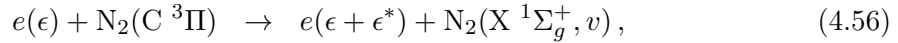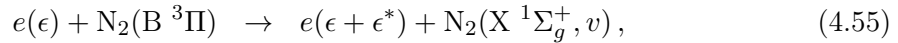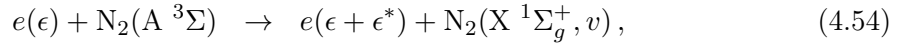
83

Figure 4.9: (a) eedf at two times during the discharge; (b) full range eedf during the post-discharge for the four models.

excited states, *i.e.*:

$$e(\epsilon) + N_2(A\ ^3\Sigma) \quad \rightarrow \quad e(\epsilon + \epsilon^*) + N_2(X\ ^1\Sigma_g^+, v)\,, \tag{4.54}$$

$$e(\epsilon) + N_2(B\ ^3\Pi) \quad \rightarrow \quad e(\epsilon + \epsilon^*) + N_2(X\ ^1\Sigma_g^+, v)\,, \tag{4.55}$$

$$e(\epsilon) + N_2(C\ ^3\Pi) \quad \rightarrow \quad e(\epsilon + \epsilon^*) + N_2(X\ ^1\Sigma_g^+, v)\,, \tag{4.56}$$

where ϵ^* is the threshold energy of the corresponding transition, that are, relative to the ground state respectively 6.17 eV, 7.35 eV and 11.03 eV. At $t = 10$ ns these processes are responsible of the peak at $\epsilon \approx 6$ eV, while the second peak at $\epsilon \approx 12$ eV is due to electrons in the peak at $\epsilon \approx 6$ eV subjected to another superelastic collision. It should be noted that the peaks are quite large due to the superposition of the different superelastic collisions. The effect of transition from the C $^3\Pi$ state are visible as small shoulders around 10 eV and 20 eV. These maxima are strongly smoothed by the model C due to the higher mean electron energy, which hides the role of superelastic collisions. Similar results are observed for $t = 1$ μs, where only the contribution of the A$^3\Sigma$ state is clearly evident.

These results clearly demonstrate that the use of complete sets of cross sections, as well as the coupling between vibrationally and electronically excited states, is very important. This is especially true in the post-discharge phase. Neglecting these aspects will lead to non-negligible errors in any model. The results in Fig. 4.9 warns on the use of the Maxwell distribution function for calculating electron-molecule rate coefficients. The results reported in Ref. [37] can be used only for particular conditions *i.e.* at very high ionization degree when electron-electron Coulomb collisions dominate.

Conclusions et perspectives

Ce mémoire d'HDR porte sur les travaux que j'ai mené pendant les dernières années, dédiés à la dynamique quantique moléculaire *ab initio*. Ces travaux sont concentrés sur les études théoriques des processus élémentaires, résolus sur les états moleculaires internes, pour les collisions réactives à impact électronique impliquant des molécules et des ions excités vibrationnellement et rotationellement. En particulier, mon travail consiste dans le calcul des sections efficaces et des coefficients de vitesse correspondant à l'excitation vibrationnelle, l'attachement dissociatif électronique, la recombinaison dissociative et l'excitation dissociative. Ces résultats représentent les données d'entre pour la construction des modèles cinétiques collisionnels-radiatifs pour les plasmas moléculaires froids, 'hors-équilibre', où les dégrés internes des molécules, et souvent même les électrons, ne suivent pas la distribution de Maxwell-Boltzmann et il est, donc, indispensable d'étudier les propriétés thermodynamiques dans une approche 'état-par-état'.

Les applications de ces modèles sont très vastes : ils vont de l'astrochimie - la modélisation du milieu interstellaire et la formation des proto-étoiles - à l'ingénierie aérospatiale - la modélisation des flux hypersoniques et de l'onde de choc qui arrivent à la rentrée des navettes aérospatiales dans les atmosphères planétaires - et à l'énergétique - la modélisation du plasma dans les réacteurs à fusion magnétique contrôlée ou les procédés de combustion assistés par les plasmas. Dans ce cadre, je me suis occupé des molécules d'azote et d'oxygène, étant les principaux composants l'atmosphère de la Terre, de la molécule de CO, qui est le principal constituant l'atmosphère de Mars, et des ions moléculaires BeH^+ and He_2^+, intervenant dans les plasmas de fusion.

Comme extension future du travaille présent, et avec le but d'avoir des modelés qui sont le plus complets possible et qui puissent reproduire les données expérimentales, il est nécessaire d'étudier les états électroniques excitées des molécules. En particulier, pour la molécule d'oxygène il faut prendre en compte les états électroniques $^1\Delta$ et $^1\Sigma$ qui sont très proches de l'état fondamental (environs un eV au-dessus) et qui peuvent donnée des contributions non négligeable.

Enfin, dans l'avenir proche, je m'occuperai de la molécule de CO_2 pour laquelle j'ai déjà fait des calculs préliminaires. Il me semble que cette étude est très importante, car il n'existe pas aujourd'hui dans la littérature des calculs approfondis. Il est indispensable, à

mon avis, d'étudier les surfaces d'énergie potentielle par des méthodes de chimie quantique et, en suite, considérer les processus de dissociation par impact des électrons, en particulier, le processus d'attachement dissociatif vers la molécule de CO. La connaissance de ces données est fortement nécessaire pour l'étude de la pollution environnementale, en particulier pour les modèles qui visent à comprendre la création/destruction de la molécule de CO_2.

Bibliography

[1] M. Capitelli, C. M. Ferreira, B. F. Gordiets, and A. I. Osipov. *Plasma Kinetics in Atmospheric Gases*. Springer Series on Atomic, Optical, and Plasma Physics. Springer, 2000.

[2] A. Fridman and L.A. Kennedy. *Plasma Physics and Engineering, Second Edition*. Taylor & Francis, 2011.

[3] A. Fridman. *Plasma Chemistry*. Cambridge University Press, 2008.

[4] P. Stubbe and W.S. Varnum. Electron energy transfer rates in the ionosphere. *Planetary and Space Science*, 20(8):1121 – 1126, 1972.

[5] A Dalgarno. Molecular processes in the early universe. *Journal of Physics: Conference Series*, 4(1):10, 2005.

[6] Chul Park. *Nonequilibrium hypersonic Aerothermodynamics*. Waley, 1990.

[7] J.S. Shang and S.T. Surzhikov. Nonequilibrium radiative hypersonic flow simulation. *Progress in Aerospace Sciences*, 53:46 – 65, 2012.

[8] Peter A. Gnoffo. Planetary-entry gas dynamics. *Annual Review of Fluid Mechanics*, 31(1):459–494, 1999.

[9] S M Starikovskaia. Plasma assisted ignition and combustion. *Journal of Physics D: Applied Physics*, 39(16):R265, 2006.

[10] O. Motojima. The iter project construction status. *Nuclear Fusion*, 55(10):104023, 2015.

[11] K. Ikeda. Progress in the iter physics basis. *Nuclear Fusion*, 47(6), 2007.

[12] N Barekzi and M Laroussi. Dose-dependent killing of leukemia cells by low-temperature plasma. *Journal of Physics D: Applied Physics*, 45(42):422002, 2012.

[13] Michael Keidar, Alex Shashurin, Olga Volotskova, Mary Ann Stepp, Priya Srinivasan, Anthony Sandler, and Barry Trink. Cold atmospheric plasma in cancer therapy. *Physics of Plasmas*, 20(5):057101, 2013.

[14] Mario Capitelli, editor. *Non-equilibrium vibrational kinetics Topics in Current Physics*, volume 36 of *39*. Springer-Verlag, 1986.

[15] M Capitelli, I Armenise, D Bruno, M Cacciatore, R Celiberto, G Colonna, O De Pascale, P Diomede, F Esposito, C Gorse, K Hassouni, A Laricchiuta, S Longo, D Pagano, D Pietanza, and M Rutigliano. Non-equilibrium plasma kinetics: a state-to-state approach. *Plasma Sources Science and Technology*, 16(1):S30, 2007.

[16] J N Bardsley and F Mandl. Resonant scattering of electrons by molecules. *Reports on Progress in Physics*, 31(2):471, 1968.

[17] George J. Schulz. Resonances in electron impact on diatomic molecules. *Rev. Mod. Phys.*, 45(3):423–486, Jul 1973.

[18] S. Trajmar, D. F. Register, and A. Chutjian. Electron scattering by molecules ii. experimental methods and data. *Physics Reports*, 97(5):219 – 356, 1983.

[19] Michael J. Brunger and Stephen J. Buckman. Electron–molecule scattering cross-sections. i. experimental techniques and data for diatomic molecules. *Physics Reports*, 357(3-5):215 – 458, 2002.

[20] A. Chutjian, A. Garscadden, and J.M. Wadehra. Electron attachment to molecules at low electron energies. *Physics Reports*, 264(6):393 – 470, 1996.

[21] W. Domcke. Theory of resonance and threshold effects in electron-molecule collisions: The projection-operator approach. *Physics Reports*, 208(2):97 – 188, 1991.

[22] L. Dubé and A. Herzenberg. Absolute cross sections from the "boomerang model" for resonant electron-molecule scattering. *Phys. Rev. A*, 20(1):194–213, Jul 1979.

[23] U. Fano. Effects of configuration interaction on intensities and phase shifts. *Phys. Rev.*, 124:1866–1878, Dec 1961.

[24] E. S. Chang and U. Fano. Theory of electron-molecule collisions by frame transformations. *Phys. Rev. A*, 6:173–185, Jul 1972.

[25] J N Bardsley. Configuration interaction in the continuum states of molecules. *Journal of Physics B: Atomic and Molecular Physics*, 1(3):349, 1968.

[26] A Giusti. A multichannel quantum defect approach to dissociative recombination. *Journal of Physics B: Atomic and Molecular Physics*, 13(19):3867, 1980.

[27] V Sidis and H Lefebvre-Brion. A 'quasi-diabatic' representation for inelastic collisions application to the scattering of he + by ne. *Journal of Physics B: Atomic and Molecular Physics*, 4(8):1040, 1971.

[28] Ch. Jungen and O. Atabek. Rovibronic interactions in the photoabsorption spectrum of molecular hydrogen and deuterium: An application of multichannel quantum defect methods. *The Journal of Chemical Physics*, 66(12):5584–5609, 1977.

[29] Ngassam V., Florescu A., Pichl L., Schneider I. F., Motapon O., and Suzor-Weiner A. The short-range reaction matrix in mqdt treatment of dissociative recombination and related processes. *Eur. Phys. J. D*, 26(2):165–171, 2003.

[30] U. Fano. Quantum defect theory of l uncoupling in H_2 as an example of channel-interaction treatment. *Phys. Rev. A*, 2:353–365, Aug 1970.

[31] Vâlcu, B., Schneider, I. F., Raoult, M., Strömholm, C., Larsson, M., and Suzor-Weiner, A. Rotational effects in low energy dissociative recombination of diatomic ions. *Eur. Phys. J. D*, 1(1):71–78, 1998.

[32] M J Seaton. Quantum defect theory. *Reports on Progress in Physics*, 46(2):167, 1983.

[33] Jonathan Tennyson. Electron-molecule collision calculations using the R-matrix method. *Physics Reports*, 491(2-3):29 – 76, 2010.

[34] J. M. Carr, P. G. Galiatsatos, J. D. Gorfinkiel, A. G. Harvey, M. A. Lysaght, D. Madden, Z. Masin, M. Plummer, J. Tennyson, and H. N. Varambhia. Ukrmol: a low-energy electron- and positron-molecule scattering suite. *The European Physical Journal D*, 66(3):58, Mar 2012.

[35] N. F. Lane. The theory of electron-molecule collisions. *Rev. Mod. Phys.*, 52:29–119, Jan 1980.

[36] Mary Shugard and Andrew U. Hazi. Theory of electron-molecule scattering: Comments on the adiabatic-nuclei approximation. *Phys. Rev. A*, 12:1895–1902, Nov 1975.

[37] V Laporta, R Celiberto, and J M Wadehra. Theoretical vibrational-excitation cross sections and rate coefficients for electron-impact resonant collisions involving rovibrationally excited N_2 and NO molecules. *Plasma Sources Science and Technology*, 21(5):055018, 2012.

[38] Vincenzo Laporta and Roberto Celiberto. Resonant electron–molecule vibrational excitation cross sections and rate coefficients for atmospheric plasmas. *Journal of Physics: Conference Series*, 388(5):052036, 2012.

[39] V Laporta, D A Little, R Celiberto, and J Tennyson. Electron-impact resonant vibrational excitation and dissociation processes involving vibrationally excited N_2 molecules. *Plasma Sources Science and Technology*, 23(6):065002, 2014.

[40] V Laporta, R Celiberto, and J Tennyson. Resonant vibrational-excitation cross sections and rate constants for low-energy electron scattering by molecular oxygen. *Plasma Sources Science and Technology*, 22(2):025001, 2013.

[41] V. Laporta, R. Celiberto, and J. Tennyson. Dissociative electron attachment and electron-impact resonant dissociation of vibrationally excited O_2 molecules. *Phys. Rev. A*, 91:012701, Jan 2015.

[42] V. Laporta, R. Celiberto, and J. Tennyson. Rate coefficients for dissociative attachment and resonant electron-impact dissociation involving vibrationally excited O_2 molecules. *AIP Conference Proceedings*, 1628:939–942, 2014.

[43] V Laporta, C M Cassidy, J Tennyson, and R Celiberto. Electron-impact resonant vibration excitation cross sections and rate coefficients for carbon monoxide. *Plasma Sources Science and Technology*, 21(4):045005, 2012.

[44] V Laporta, J Tennyson, and R Celiberto. Carbon monoxide dissociative attachment and resonant dissociation by electron-impact. *Plasma Sources Science and Technology*, 25(1):01LT04, 2016.

[45] V Laporta, J Tennyson, and R Celiberto. Calculated low-energy electron-impact vibrational excitation cross sections for CO_2 molecule. *Plasma Sources Science and Technology*, 25(6):06LT02, 2016.

[46] R Celiberto, K L Baluja, R K Janev, and V Laporta. Electron-impact dissociation cross sections of vibrationally excited He_2^+ molecular ion. *Plasma Physics and Controlled Fusion*, 58(1):014024, 2016.

[47] V Laporta, K Chakrabarti, R Celiberto, R K Janev, J Zs Mezei, S Niyonzima, J Tennyson, and I F Schneider. Theoretical resonant electron-impact vibrational excitation, dissociative recombination and dissociative excitation cross sections of rovibrationally excited BeH^+ ion. *Plasma Physics and Controlled Fusion*, 59(4):045008, 2017.

[48] F J Gordillo-Vázquez. Air plasma kinetics under the influence of sprites. *Journal of Physics D: Applied Physics*, 41(23):234016, 2008.

[49] V. Laporta and D. Bruno. Electron-vibration energy exchange models in nitrogen-containing plasma flows. *The Journal of Chemical Physics*, 138(10):104319, 2013.

[50] K. L. Heritier, R. L. Jaffe, V. Laporta, and M. Panesi. Energy transfer models in nitrogen plasmas: Analysis of $N_2(X\,^1\Sigma_g^+)$-$N(^4S_u)$-e interaction. *The Journal of Chemical Physics*, 141(18):184302, 2014.

[51] Arnaud Bultel and Julien Annaloro. Elaboration of collisional–radiative models for flows related to planetary entries into the earth and mars atmospheres. *Plasma Sources Science and Technology*, 22(2):025008, 2013.

[52] Julien Annaloro and Arnaud Bultel. Vibrational and electronic collisional-radiative model in air for earth entry problems. *Physics of Plasmas*, 21(12):123512, 2014.

[53] Odile Dutuit, Nathalie Carrasco, Roland Thissen, Véronique Vuitton, Christian Alcaraz, Pascal Pernot, Nadia Balucani, Piergiorgio Casavecchia, André Canosa, Sébastien Le Picard, Jean-Christophe Loison, Zdenek Herman, Jan Zabka, Daniela Ascenzi, Paolo Tosi, Pietro Franceschi, Stephen D. Price, and Panayotis Lavvas. Critical review of N, N^+, N_2^+, N^{++} and N_2^{++} main production processes and reactions of relevance to titan's atmosphere. *The Astrophysical Journal Supplement Series*, 204(2):20, 2013.

[54] G. J. Schulz. Vibrational excitation of nitrogen by electron impact. *Phys. Rev.*, 125(1):229–232, Jan 1962.

[55] G. J. Schulz. Vibrational excitation of N_2, CO, and H_2 by electron impact. *Phys. Rev.*, 135(4A):A988–A994, Aug 1964.

[56] M Vicic, G Poparic, and D S Belic. Large vibrational excitation of N_2 by low-energy electrons. *Journal of Physics B: Atomic, Molecular and Optical Physics*, 29(6):1273, 1996.

[57] M. Ristić, G.B. Poparić, and D.S. Belić. Rate coefficients for resonant vibrational excitation of N_2. *Chemical Physics*, 331(2):410 – 416, 2007.

[58] J Comer and F H Read. Electron impact studies of a resonant state of N_2^-. *Journal of Physics B: Atomic and Molecular Physics*, 4(8):1055, 1971.

[59] C. F. Wong and J. C. Light. Application of R-matrix theory to resonant reactive electron-molecule scattering: Vibrational excitation and dissociative attachment of N_2 and F_2. *Phys. Rev. A*, 30:2264–2273, Nov 1984.

[60] M Allan. Excitation of vibrational levels up to $v=17$ in N_2 by electron impact in the 0-5 eV region. *J. Phys. B: At. Mol. Opt. Phys.*, 18(22):4511, 1985.

[61] M Allan. Electron collisions with NO: elastic scattering, vibrational excitation and $^2\Pi_{1/2}\ ^2\Pi_{3/2}$ transitions. *J. Phys. B: At. Mol. Opt. Phys.*, 38(5):603, 2005.

[62] Christopher J. Sweeney and Tong W. Shyn. Measurement of absolute differential cross sections for the vibrational excitation of molecular nitrogen by electron impact in the $^2\Pi_g$ shape resonance region. *Phys. Rev. A*, 56:1384–1392, Aug 1997.

[63] Weiguo Sun, Michael A. Morrison, William A. Isaacs, Wayne K. Trail, Dean T. Alle, R. J. Gulley, Michael J. Brennan, and Stephen J. Buckman. Detailed theoretical and experimental analysis of low-energy electron-N_2 scattering. *Phys. Rev. A*, 52:1229–1256, Aug 1995.

[64] B. I. Schneider, M. Le Dourneuf, and Vo Ky Lan. Resonant vibrational excitation of N_2 by low-energy electrons: An ab initio r-matrix calculation. *Phys. Rev. Lett.*, 43(26):1926–1929, Dec 1979.

[65] Michael Berman, Hernán Estrada, L. S. Cederbaum, and W. Domcke. Nuclear dynamics in resonant electron-molecule scattering beyond the local approximation: The 2.3-eV shape resonance in N_2. *Phys. Rev. A*, 28(3):1363–1381, Sep 1983.

[66] W. M. Huo, V. McCoy, M. A. P. Lima, and T. L. Gibson. Electron-nitrogen molecule collisions in high temperature nonequilibrium air. In J. N. Moss and C. D. Scott, editors, *Thermochemical Aspects of Re-entry Flows*, volume 103 of *Progress in Astronautics and Aeronautics*, pages 152–196. AIAA, New York, 1986.

[67] A A Mihajlov, V D Stojanovic, and Z Lj Petrovic. Resonant vibrational excitation/de-excitation of $N_2(v)$ by electrons. *Journal of Physics D: Applied Physics*, 32(20):2620, 1999.

[68] Karel Houfek, T. N. Rescigno, and C. W. McCurdy. Probing the nonlocal approximation to resonant collisions of electrons with diatomic molecules. *Phys. Rev. A*, 77:012710, Jan 2008.

[69] Karel Houfek, Martin Čížek, and Jiří Horáček. On irregular oscillatory structures in resonant vibrational excitation cross-sections in diatomic molecules. *Chemical Physics*, 347(1):250 – 256, 2008. Ultrafast Photoinduced Processes in Polyatomic Molecules.

[70] Yukikazu Itikawa. Cross sections for electron collisions with nitrogen molecules. *Journal of Physical and Chemical Reference Data*, 35(1):31–53, 2006.

[71] Hans-Joachim Werner, Peter J. Knowles, Gerald Knizia, Frederick R. Manby, and Martin Schütz. Molpro: a general-purpose quantum chemistry program package. *Wiley Interdisciplinary Reviews: Computational Molecular Science*, 2(2):242–253, 2012.

[72] Alexandre Faure, Jimena D Gorfinkiel, Lesley A Morgan, and Jonathan Tennyson. Gtobas: fitting continuum functions with gaussian-type orbitals. *Computer Physics Communications*, 144(2):224 – 241, 2002.

[73] Lesley A. Morgan, Jonathan Tennyson, and Charles J. Gillan. The UK molecular R-matrix codes. *Computer Physics Communications*, 114(1–3):120 – 128, 1998.

[74] Jonathan Tennyson. R -matrix calculation of rydberg states of CO. *Journal of Physics B: Atomic, Molecular and Optical Physics*, 29(24):6185, 1996.

[75] Robert J. Le Roy, Yiye Huang, and Calvin Jary. An accurate analytic potential function for ground-state N_2 from a direct-potential-fit analysis of spectroscopic data. *The Journal of Chemical Physics*, 125(16):–, 2006.

[76] B K Sarpal, S E Branchett, J Tennyson, and L A Morgan. Bound states using the R-matrix method: Rydberg states of HeH. *Journal of Physics B: Atomic, Molecular and Optical Physics*, 24(17):3685, 1991.

[77] D. Spence and G. J. Schulz. Vibrational excitation and compound states in NO. *Phys. Rev. A*, 3(6):1968–1976, Jun 1971.

[78] D Teillet-Billy and F Fiquet-Fayard. *Journal of Physics B: Atomic and Molecular Physics*, 10(4):L111, 1977.

[79] Regina de Vivie and Sigrid D. Peyerimhoff. Theoretical spectroscopy of the NO radical. i. potential curves and lifetimes of excited states. *The Journal of Chemical Physics*, 89(5):3028–3043, 1988.

[80] M. Jelisavcic, R. Panajotovic, and S. J. Buckman. Absolute collision cross sections for low energy electron scattering from NO: The role of resonances in elastic scattering and vibrational excitation. *Phys. Rev. Lett.*, 90(20):203201, May 2003.

[81] L. Josic, T. Wróblewski, Z. Lj. Petrovic, J. Mechlinska-Drewko, and G. P. Karwasz. Influence of resonant scattering on electron-swarm parameters in NO. *Chemical Physics Letters*, 350(3-4):318 – 324, 2001.

[82] C. S. Trevisan, K. Houfek, Z. Zhang, A. E. Orel, C. W. McCurdy, and T. N. Rescigno. Nonlocal model of dissociative electron attachment and vibrational excitation of NO. *Phys. Rev. A*, 71(5):052714, May 2005.

[83] C. J. Noble, K. Higgins, G. Wöste, P. Duddy, P. G. Burke, P. J. O. Teubner, A. G. Middleton, and M. J. Brunger. Resonant mechanisms in the vibrational excitation of ground state O_2. *Phys. Rev. Lett.*, 76(19):3534–3537, May 1996.

[84] M. Krauss, D. Neumann, A. C. Wahl, G. Das, and W. Zemke. Excited electronic states of O_2^-. *Phys. Rev. A*, 7(1):69–77, Jan 1973.

[85] Carl S. Ewig and Joel Tellinghuisen. Ab initio study of the electronic states of O_2^- in vacuo and in simulated ionic solids. *The Journal of Chemical Physics*, 95(2):1097–1106, 1991.

[86] C. J. Noble and P. G. Burke. R-matrix calculations of low-energy electron scattering by oxygen molecules. *Phys. Rev. Lett.*, 68(13):2011–2014, Mar 1992.

[87] K Higgins, C J Noble, and P G Burke. Low energy electron scattering by oxygen molecules. *Journal of Physics B: Atomic, Molecular and Optical Physics*, 27(14):3203, 1994.

[88] K Higgins, C J Gillan, P G Burke, and C J Noble. Low-energy electron scattering by oxygen molecules. ii. vibrational excitation. *Journal of Physics B: Atomic, Molecular and Optical Physics*, 28(15):3391, 1995.

[89] J.W. McConkey, C.P. Malone, P.V. Johnson, C. Winstead, V. McKoy, and I. Kanik. Electron impact dissociation of oxygen-containing molecules-a critical review. *Physics Reports*, 466(1-3):1 – 103, 2008.

[90] Donald Rapp and Donald D. Briglia. Total cross sections for ionization and attachment in gases by electron impact. ii. negative-ion formation. *The Journal of Chemical Physics*, 43(5):1480–1489, 1965.

[91] G. J. Schulz. Cross sections and electron affinity for electron impact. *Phys. Rev.*, 128:178–186, Oct 1962.

[92] L. G. Christophorou, R. N. Compton, G. S. Hurst, and P. W. Reinhardt. Determination of electron-capture cross sections with swarm-beam techniques. *The Journal of Chemical Physics*, 43(12):4273–4281, 1965.

[93] Thomas Jaffke, Martina Meinke, Reza Hashemi, Loucas G. Christophorou, and Eugen Illenberger. Dissociative electron attachment to singlet oxygen. *Chemical Physics Letters*, 193(1-3):62 – 68, 1992.

[94] P. C. Cosby. Electron-impact dissociation of oxygen. *The Journal of Chemical Physics*, 98(12):9560–9569, 1993.

[95] Yukikazu Itikawa. Cross sections for electron collisions with oxygen molecules. *Journal of Physical and Chemical Reference Data*, 38(1):1–20, 2009.

[96] M Allan. Measurement of absolute differential cross sections for vibrational excitation of O_2 by electron impact. *Journal of Physics B: Atomic, Molecular and Optical Physics*, 28(23):5163, 1995.

[97] S. F. Wong, M. J. W. Boness, and G. J. Schulz. Vibrational excitation of O_2 by electron impact above 4 eV. *Phys. Rev. Lett.*, 31(16):969–972, Oct 1973.

[98] Vaibhav S Prabhudesai, Dhananjay Nandi, and E Krishnakumar. *Journal of Physics B: Atomic, Molecular and Optical Physics*, 39(14):L277, 2006.

[99] Eric B. Burgh, Kevin France, and Stephan R. McCandliss. Direct measurement of the ratio of carbon monoxide to molecular hydrogen in the diffuse interstellar medium. *The Astrophysical Journal*, 658(1):446, 2007.

[100] L. Campbell, M. Allan, and M. J. Brunger. Electron impact vibrational excitation of carbon monoxide in the upper atmospheres of mars and venus. *J. Geophys. Res.*, 116(A9):A09321–, September 2011.

[101] G.N. Haddad and H.B. Milloy. Cross sections for electron carbon monoxide collisions in the range 1-4 eV. *Aust. J. Phys.*, 36(4):473, 1983.

[102] C. Gorse, M. Cacciatore, and M. Capitelli. Kinetic processes in non-equilibrium carbon monoxide discharges. i. vibrational kinetics and dissociation rates. *Chemical Physics*, 85(2):165 – 176, 1984.

[103] C. Gorse and M. Capitelli. Kinetic processes in non-equilibrium carbon monoxide discharges. ii. self-consistent electron energy distribution functions. *Chemical Physics*, 85(2):177 – 187, 1984.

[104] M. Allan. Electron collisions with CO: Elastic and vibrational excitation cross sections. *Phys. Rev. A*, 81:042706, Apr 2010.

[105] G. B. Poparić, D. S. Belić, and M. D. Vićić. Resonant vibrational excitation of CO by low-energy electrons. *Phys. Rev. A*, 73:062713, Jun 2006.

[106] Jennifer C Gibson, Lesley A Morgan, Robert J Gulley, Michael J Brunger, Christoph T Bundschu, and Stephen J Buckman. Low energy electron scattering from CO: absolute cross section measurements and R-matrix calculations. *Journal of Physics B: Atomic, Molecular and Optical Physics*, 29(14):3197, 1996.

[107] Yukikazu Itikawa. Cross sections for electron collisions with carbon monoxide. *Journal of Physical and Chemical Reference Data*, 44(1):–, 2015.

[108] L A Morgan. Low-energy electron scattering by CO. *Journal of Physics B: Atomic, Molecular and Optical Physics*, 24(21):4649, 1991.

[109] L A Morgan and J Tennyson. Electron impact excitation cross sections for CO. *Journal of Physics B: Atomic, Molecular and Optical Physics*, 26(15):2429, 1993.

[110] Fabian Grätz, Daniel P. Engelhart, Roman J. V. Wagner, Gerard Meijer, Alec M. Wodtke, and Tim Schäfer. Co quenching at a metal surface: Evidence of an electron transfer mediated mechanism. *The Journal of Chemical Physics*, 141(4):044712, 2014.

[111] Mario Capitelli, Gianpiero Colonna, Giuliano D'Ammando, Vincenzo Laporta, and Annarita Laricchiuta. Nonequilibrium dissociation mechanisms in low temperature nitrogen and carbon monoxide plasmas. *Chemical Physics*, 438(0):31 – 36, 2014.

[112] Tomáš Kozák and Annemie Bogaerts. Evaluation of the energy efficiency of CO_2 conversion in microwave discharges using a reaction kinetics model. *Plasma Sources Science and Technology*, 24(1):015024, 2015.

[113] Gustavo E. Scuseria, Michael D. Miller, Frank Jensen, and Jan Geertsen. The dipole moment of carbon monoxide. *The Journal of Chemical Physics*, 94(10):6660–6663, 1991.

[114] K. Kirby-Docken and B. Liu. Theoretical study of molecular dipole moment functions. i. the $X\,^1\Sigma^+$ state of CO. *The Journal of Chemical Physics*, 66(10):4309–4316, 1977.

[115] Jonathan Tennyson, P.G. Burke, and K.A. Berrington. The generation of continuum orbitals for molecular R-matrix calculations using lagrange orthogonalisation. *Computer Physics Communications*, 47(2-3):207 – 212, 1987.

[116] Jonathan Tennyson and Cliff J. Noble. RESON a program for the detection and fitting of breit-wigner resonances. *Computer Physics Communications*, 33(4):421 – 424, 1984.

[117] S Salvini, P G Burke, and C J Noble. Electron scattering by polar molecules using the R-matrix method. *Journal of Physics B: Atomic and Molecular Physics*, 17(12):2549, 1984.

[118] Wim Klopper, Rafa A. Bachorz, David P. Tew, and Christof Hättig. Sub-mev accuracy in first-principles computations of the ionization potentials and electron affinities of the atoms h to ne. *Phys. Rev. A*, 81:022503, Feb 2010.

[119] O Taylan and H Berberoglu. Dissociation of carbon dioxide using a microhollow cathode discharge plasma reactor: effects of applied voltage, flow rate and concentration. *Plasma Sources Sci. Technol.*, 24:015006, 2015.

[120] Adelbert P.H. Goede, Waldo A. Bongers, Martijn F. Graswinckel, Richard M.C.M van de Sanden, Martina Leins, Jochen Kopecki, Andreas Schulz, and Mathias Walker.

Production of solar fuels by CO_2 plasmolysis. *EPJ Web of Conferences*, 79:01005, 2014.

[121] Annemie Bogaerts, Christophe Bie, Ramses Snoeckx, and Tomas Kozák. Plasma based CO_2 and CH_4 conversion: A modeling perspective. *Plasma Processes and Polymers*, 14(6), 9 2016.

[122] L.D. Pietanza, G. Colonna, V. Laporta, R. Celiberto, G. D'Ammando, A. Laricchiuta, and M. Capitelli. Influence of electron molecule resonant vibrational collisions over the symmetric mode and direct excitation-dissociation cross sections of CO_2 on the electron energy distribution function and dissociation mechanisms in cold pure CO_2 plasmas. *The Journal of Physical Chemistry A*, 120(17):2614–2628, 2016. PMID: 27064438.

[123] Andrea Lombardi, Noelia Faginas-Lago, Leonardo Pacifici, and Alessandro Costantini. Modeling of energy transfer from vibrationally excited CO_2 molecules: Cross sections and probabilities for kinetic modeling of atmospheres, flows, and plasmas. *The Journal of Physical Chemistry A*, 117(45):11430–11440, 2013. PMID: 24117231.

[124] Tomáš Kozák and Annemie Bogaerts. Splitting of CO_2 by vibrational excitation in non-equilibrium plasmas: a reaction kinetics model. *Plasma Sources Science and Technology*, 23(4):045004, 2014.

[125] André Janeco, Nuno R. Pinhão, and Vasco Guerra. Electron kinetics in $He/CH_4/CO_2$ mixtures used for methane conversion. *The Journal of Physical Chemistry C*, 119(1):109–120, 2015.

[126] Michael A. Morrison, Neal F. Lane, and Lee A. Collins. Low-energy electron-molecule scattering: Application of coupled-channel theory to e-CO_2 collisions. *Phys. Rev. A*, 15:2186–2201, Jun 1977.

[127] I Cadez, F Gresteau, M Tronc, and R I Hall. Resonant electron impact excitation of CO_2 in the 4 eV region. *Journal of Physics B: Atomic and Molecular Physics*, 10(18):3821, 1977.

[128] M. Allan. Selectivity in the excitation of fermi-coupled vibrations in CO_2 by impact of slow electrons. *Phys. Rev. Lett.*, 87:033201, Jun 2001.

[129] L. A. Morgan. Virtual states and resonances in electron scattering by CO_2. *Phys. Rev. Lett.*, 80:1873–1875, Mar 1998.

[130] J. Tennyson and L. A. Morgan. Electron collisions with polyatomic molecules using the R–matrix method. *Philosophical Transactions of the Royal Society of London A: Mathematical, Physical and Engineering Sciences*, 357(1755):1161–1173, 1999.

[131] Stephane Mazevet, Michael A Morrison, Lesley A. Morgan, and Robert K. Nesbet. Virtual-state effects on elastic scattering and vibrational excitation of CO_2 by electron impact. *Phys. Rev. A*, 64:040701, Sep 2001.

[132] Yukikazu Itikawa. Cross sections for electron collisions with carbon dioxide. *Journal of Physical and Chemical Reference Data*, 31(3):749–767, 2002.

[133] H. Estrada, L. S. Cederbaum, and W. Domcke. Vibronic coupling of short-lived electronic states. *The Journal of Chemical Physics*, 84(1):152–169, 1986.

[134] R. Celiberto, V. Laporta, A. Laricchiuta, J. Tennyson, and J.M. Wadehra. Molecular physics of elementary processes relevant to hypersonics: Electron-molecule collisions. *The Open Plasma Physics Journal, 2014, 7, (Suppl 1: M2) 33-47*, 7, (Suppl 1: M2):33–47, 2014.

[135] T. N. Rescigno, W. A. Isaacs, A. E. Orel, H.-D. Meyer, and C. W. McCurdy. Theoretical study of resonant vibrational excitation of CO_2 by electron impact. *Phys. Rev. A*, 65:032716, Feb 2002.

[136] C. W. McCurdy, W. A. Isaacs, H.-D. Meyer, and T. N. Rescigno. Resonant vibrational excitation of CO_2 by electron impact: Nuclear dynamics on the coupled components of the $^2\Pi_u$ resonance. *Phys. Rev. A*, 67:042708, Apr 2003.

[137] Gerhard Herzberg. *Molecular Spectra and Molecular Structure III. Electronic Spectra and Electronic Structure od Polyatomic Molecules.* 1966.

[138] G. B. Poparić, M. M. Ristić, and D. S. Belić. Electron energy transfer rate coefficients of carbon dioxide. *The Journal of Physical Chemistry A*, 114(4):1610–1615, 2010. PMID: 20043664.

[139] C Szmytkowski, M Zubek, and J Drewko. Calculation of cross sections for vibrational excitation and de-excitation of CO_2 by electronic collisions. *Journal of Physics B: Atomic and Molecular Physics*, 11(12):L371, 1978.

[140] Kinga Kutasi, Péter Hartmann, and Zoltán Donkó. Self-consistent modelling of helium discharges: investigation of the role of He_2^+ ions. *Journal of Physics D: Applied Physics*, 34(23):3368, 2001.

[141] P C. Stancil. Continuous absorption by He_2^+ and H_2^+ in cool white dwarfs. *The Astrophysical Journal*, 430:360–370, 06 1994.

[142] A. A. Mihajlov, Lj. M. Ignjatović, M. S. Dimitrijević, and Z. Djurić. Symmetrical chemi-ionization and chemi-recombination processes in low-temperature layers

of helium-rich db white dwarf atmospheres. *The Astrophysical Journal Supplement Series*, 147(2):369, 2003.

[143] B.J. Braams. Atomic and molecular data for the state-resolved modelling of hydrogen and helium and their isotopes in fusion plasma. Technical report, International Atomic Energy Agency, Vienna, Austria Vienna International Centre, P.O. Box 100, A-1400 Vienna, Austria, 2013.

[144] J. Royal and A. E. Orel. Resonant dissociative excitation and vibrational excitation of He_2^+. *Phys. Rev. A*, 75:052706, May 2007.

[145] Junkai Xie, Bill Poirier, and Gregory I. Gellene. Accurate, two-state ab initio study of the ground and first-excited states of He_2^+, including exact treatment of all born–oppenheimer correction terms. *The Journal of Chemical Physics*, 122(18):184310, 2005.

[146] Aristophanes Metropoulos, Yan Li, Gerhard Hirsch, and Robert J. Buenker. *Chemical Physics Letters*, 198(3):266 – 272, 1992.

[147] Wei-Cheng Tung, Michele Pavanello, and Ludwik Adamowicz. Very accurate potential energy curve of the He_2^+ ion. *The Journal of Chemical Physics*, 136(10):104309, 2012.

[148] D Nishijima, R P Doerner, M J Baldwin, G De Temmerman, and E M Hollmann. Properties of bed molecules in edge plasma relevant conditions. *Plasma Physics and Controlled Fusion*, 50(12):125007, 2008.

[149] R.P. Doerner, M.J. Baldwin, D. Buchenauer, G. De Temmerman, and D. Nishijima. The role of beryllium deuteride in plasma-beryllium interactions. *Journal of Nuclear Materials*, 390–391:681 – 684, 2009. Proceedings of the 18th International Conference on Plasma-Surface Interactions in Controlled Fusion DeviceProceedings of the 18th International Conference on Plasma-Surface Interactions in Controlled Fusion Device.

[150] C Björkas, K Vörtler, K Nordlund, D Nishijima, and R Doerner. Chemical sputtering of be due to d bombardment. *New Journal of Physics*, 11(12):123017, 2009.

[151] S. Brezinsek, A. Widdowson, M. Mayer, V. Philipps, P. Baron-Wiechec, J.W. Coenen, K. Heinola, A. Huber, J. Likonen, P. Petersson, M. Rubel, M.F. Stamp, D. Borodin, J.P. Coad, A.G. Carrasco, A. Kirschner, S. Krat, K. Krieger, B. Lipschultz, Ch. Linsmeier, G.F. Matthews, K. Schmid, and JET contributors. Beryllium migration in jet iter-like wall plasmas. *Nuclear Fusion*, 55(6):063021, 2015.

[152] C. Björkas, D. Borodin, A. Kirschner, R.K. Janev, D. Nishijima, R. Doerner, and K. Nordlund. Multiscale modeling of bed release and transport in pisces-b. *Journal of Nuclear Materials*, 438, Supplement:S276 – S279, 2013. Proceedings of the

20th International Conference on Plasma-Surface Interactions in Controlled Fusion Devices.

[153] R Celiberto, R K Janev, and D Reiter. State-to-state electron impact cross sections for BeH$^+$ molecular ions in iter-like fusion edge plasmas with be walls. *Plasma Physics and Controlled Fusion*, 54(3):035012, 2012.

[154] K. Chakrabarti and J. Tennyson. Electron collisions with the BeH$^+$ molecular ion in the R-matrix approach. *The European Physical Journal D*, 66(1):1–7, 2012.

[155] J. B. Roos, M. Larsson, Å. Larson, and A. E. Orel. Dissociative recombination of BeH$^+$. *Phys. Rev. A*, 80:012501, Jul 2009.

[156] S. Niyonzima, S. Ilie, N. Pop, J. Zs. Mezei, K. Chakrabarti, V. Morel, B. Peres, D.A. Little, K. Hassouni, Å. Larson, A.E. Orel, D. Benredjem, A. Bultel, J. Tennyson, D. Reiter, and I.F. Schneider. Low-energy collisions between electrons and BeH$^+$: Cross sections and rate coefficients for all the vibrational states of the ion. *Atomic Data and Nuclear Data Tables*, 115–116:287 – 308, 2017.

[157] S. Niyonzima, F. Lique, K. Chakrabarti, Å. Larson, A. E. Orel, and I. F. Schneider. Multichannel-quantum-defect-theory treatment of reactive collisions between electrons and BeH$^+$. *Phys. Rev. A*, 87:022713, Feb 2013.

[158] J Zs Mezei, S Niyonzima, D Backodissa, N Pop, F O Waffeu Tamo, K Chakrabarti, O Motapon, A Wolf, J Robert, O Dulieu, ÅLarson, A E Orel, A Bultel, and I F Schneider. Electronic and photonic reactive collisions in edge fusion plasma and interstellar space: Application to H$_2$ and BeH systems. *Journal of Physics: Conference Series*, 576:012005, 2015.

[159] O Motapon, S Niyonzima, K Chakrabarti, J Zs Mezei, D Backodissa, S Ilie, M D Epee Epee, B Peres, M. Lanza, T Tchakoua, N Pop, F Argoubi, M Telmini, O Dulieu, A Bultel, J Robert, ÅLarson, A E Orel, and I F Schneider. Advances in the MQDT approach of electron/molecular cation reactive collisions: High precision extensive calculations for applications. *EPJ Web of Conferences*, 84:02003, 2015.

[160] P. S. Bagus, C. M. Moser, P. Goethals, and G. Verhaegen. Accurate ab initio calculation of the beh molecule. i. the X and a states. *The Journal of Chemical Physics*, 58(5):1886–1897, 1973.

[161] C.J. Noble and R.K. Nesbet. Cfasym, a program for the calculation of the asymptotic solutions of the coupled equations of electron collision theory. *Computer Physics Communications*, 33(4):399 – 411, 1984.

[162] K Chakrabarti and Jonathan Tennyson. R-matrix calculation of bound and resonant states of BeH. *Journal of Physics B: Atomic, Molecular and Optical Physics*, 48(23):235202, 2015.

[163] M Capitelli, R Celiberto, F Esposito, A Laricchiuta, K Hassouni, and S Longo. Elementary processes and kinetics of H_2 plasmas for different technological applications. *Plasma Sources Science and Technology*, 11(3A):A7, 2002.

[164] M. Capitelli, M. Cacciatore, R. Celiberto, O. De Pascale, P. Diomede, F. Esposito, A. Gicquel, C. Gorse, K. Hassouni, A. Laricchiuta, S. Longo, D. Pagano, and M. Rutigliano. Vibrational kinetics, electron dynamics and elementary processes in H_2 and D_2 plasmas for negative ion production: modelling aspects. *Nuclear Fusion*, 46(6):S260, 2006.

[165] M. Cacciatore, M. Capitelli, and C. Gorse. Non-equilibrium dissociation and ionization of nitrogen in electrical discharges: The role of electronic collisions from vibrationally excited molecules. *Chemical Physics*, 66(1-2):141 – 151, 1982.

[166] C. Gorse, M. Cacciatore, M. Capitelli, S. De Benedictis, and G. Dilecce. Electron energy distribution functions under N_2 discharge and post-discharge conditions: A self-consistent approach. *Chemical Physics*, 119(1):63 – 70, 1988.

[167] J Loureiro, C M Ferreira, M Capitelli, C Gorse, and M Cacciatore. Non-equilibrium kinetics in nitrogen discharges: a comparative analysis of two theoretical approaches. *Journal of Physics D: Applied Physics*, 23(11):1371, 1990.

[168] G. Colonna, C. Gorse, M. Capitelli, R. Winkler, and J. Wilhelm. *Chemical Physics Letters*, 213(1-2):5 – 9, 1993.

[169] V. Guerra, P. A. Sá, and J. Loureiro. Kinetic modeling of low-pressure nitrogen discharges and post-discharges. *The European Physical Journal - Applied Physics*, 28:125–152, 11 2004.

[170] J Loureiro, V Guerra, P A Sá, C D Pintassilgo, and M Lino da Silva. Non-equilibrium kinetics in N_2 discharges and post-discharges: a full picture by modelling and impact on the applications. *Plasma Sources Science and Technology*, 20(2):024007, 2011.

[171] I A Kossyi, A Yu Kostinsky, A A Matveyev, and V P Silakov. Kinetic scheme of the non-equilibrium discharge in nitrogen-oxygen mixtures. *Plasma Sources Science and Technology*, 1(3):207, 1992.

[172] Christophe O. Laux, Laurent Pierrot, and Richard J. Gessman. State-to-state modeling of a recombining nitrogen plasma experiment. *Chemical Physics*, 398(0):46 –

55, 2012. Chemical Physics of Low-Temperature Plasmas (in honour of Prof Mario Capitelli).

[173] M Lino da Silva, V Guerra, and J Loureiro. A review of non-equilibrium dissociation rates and models for atmospheric entry studies. *Plasma Sources Science and Technology*, 18(3):034023, 2009.

[174] P Supiot, D Blois, S De Benedictis, G Dilecce, M Barj, A Chapput, O Dessaux, and P Goudmand. Excitation of $N_2(b\,^3\Pi_g)$ in the nitrogen short-lived afterglow. *Journal of Physics D: Applied Physics*, 32(15):1887, 1999.

[175] P Macko, G Cunge, and N Sadeghi. *Journal of Physics D: Applied Physics*, 34(12):1807, 2001.

[176] Richard Jaffe, David Schwenke, Galina Chaban, and Winifred Huo. Vibrational and rotational excitation and relaxation of nitrogen from accurate theoretical calculations. Aerospace Sciences Meetings. American Institute of Aeronautics and Astronautics, January 2008.

[177] Galina Chaban, Richard Jaffe, David Schwenke, and Winifred Huo. Dissociation cross sections and rate coefficients for nitrogen from accurate theoretical calculations. Aerospace Sciences Meetings. American Institute of Aeronautics and Astronautics, January 2008.

[178] Richard Jaffe, David Schwenke, and Galina Chaban. Theoretical analysis of N_2 collisional dissociation and rotation-vibration energy transfer. Aerospace Sciences Meetings. American Institute of Aeronautics and Astronautics, January 2009.

[179] Richard Jaffe, David Schwenke, and Galina Chaban. Vibration-rotation excitation and dissociation in N_2-N_2 collisions from accurate theoretical calculations. Fluid Dynamics and Co-located Conferences. American Institute of Aeronautics and Astronautics, June 2010.

[180] Marco Panesi, Richard L. Jaffe, David W. Schwenke, and Thierry E. Magin. *The Journal of Chemical Physics*, 138(4):044312, 2013.

[181] M. Panesi, A. Munafò, T. E. Magin, and R. L. Jaffe. Nonequilibrium shock-heated nitrogen flows using a rovibrational state-to-state method. *Phys. Rev. E*, 90:013009, Jul 2014.

[182] L. S. Polak, P. A. Sergeev, D. I. Slovetskii, and R. D. Todesaite. In *Proceedings 12th Int. Conference on Phenomena in Ionized Gases, Part 1, Eindhoven 1975*. J. G. A. Holscher and D. C. Schram (Eds.), 1975.

[183] P.A. Sergeev and D.I. Slovetsky. Vibrationally excited molecules and mechanisms of chemical and physical processes in non-equilibrium plasmas. *Chemical Physics*, 75(2):231 – 241, 1983.

[184] Capitelli, M. and Dilonardo, M. Non-equilibrium dissociation of nitrogen. *Rev. Phys. Appl. (Paris)*, 13(3):115–123, 1978.

[185] M. Capitelli, C. Gorse, and G.D. Billing. V-V pumping up in non-equilibrium nitrogen: Effects on the dissociation rate. *Chemical Physics*, 52(3):299 – 304, 1980.

[186] M. Capitelli and M. Dilonardo. Nonequilibrium vibrational populations of diatomic species in electrical discharges: Effects on the dissociation rates. *Chemical Physics*, 24(3):417 – 427, 1977.

[187] I. Armenise, M. Capitelli, R. Celiberto, G. Colonna, C. Gorse, and A. Laganà. The effect of $N + N_2$ collisions on the non-equilibrium vibrational distributions of nitrogen under reentry conditions. *Chemical Physics Letters*, 227(1):157 – 163, 1994.

[188] F. Esposito, I. Armenise, and M. Capitelli. N–N_2 state to state vibrational-relaxation and dissociation rates based on quasiclassical calculations. *Chemical Physics*, 331(1):1 – 8, 2006.

[189] F. Esposito and M. Capitelli. Qct calculations for the process $N_2(v) + N \rightarrow N_2(v') + N$ in the whole vibrational range. *Chemical Physics Letters*, 418(4):581 – 585, 2006.

[190] M. Capitelli, I. Armenise, E. Bisceglie, D. Bruno, R. Celiberto, G. Colonna, G. D'Ammando, O. De Pascale, F. Esposito, C. Gorse, V. Laporta, and A. Laricchiuta. Thermodynamics, transport and kinetics of equilibrium and non-equilibrium plasmas: A state-to-state approach. *Plasma Chemistry and Plasma Processing*, 32:427–450, 2012. 10.1007/s11090-011-9339-7.

[191] P. C. Cosby. Electron-impact dissociation of nitrogen. *The Journal of Chemical Physics*, 98(12):9544–9553, 1993.

[192] C Park. Rate Parameters for Electronic Excitation of Diatomic Molecules 1. Electron-Impact Processes. *AIAA paper*, 2008-1206, 2008.

[193] Mario Capitelli, Gianpiero Colonna, Giuliano D'Ammando, Vincenzo Laporta, and Annarita Laricchiuta. The role of electron scattering with vibrationally excited nitrogen molecules on non-equilibrium plasma kinetics. *Physics of Plasmas*, 20(10):101609, 2013.

[194] V Guerra, E Galiaskarov, and J Loureiro. Dissociation mechanisms in nitrogen discharges. *Chemical Physics Letters*, 371(5):576 – 581, 2003.

[195] N. A. Dyatko, Yu. Z. Ionikh, A. V. Meshchanov, A. P. Napartovich, and K. A. Barzilovich. Specific features of the current-voltage characteristics of diffuse glow discharges in Ar:N$_2$ mixtures. *Plasma Physics Reports*, 36(12):1040–1064, Dec 2010.

[196] A. Bourdon and P. Vervisch. Analytical models for electron-vibration coupling in nitrogen plasma flows. *Journal of Thermophysics and Heat Transfer*, 14(4):489–495, 2000.

[197] C. Gorse, M. Capitelli, and A. Ricard. On the coupling of electron and vibrational energy distributions in H$_2$, N$_2$, and CO post discharges. *The Journal of Chemical Physics*, 82(4):1900–1906, 1985.

[198] G. Colonna and M. Capitelli. Electron and vibrational kinetics in the boundary layer of hypersonic flow. *Journal of Thermophysics and Heat Transfer*, 10(3):406–412, July 1996.

[199] G. Colonna and M. Capitelli. Self-consistent model of chemical, vibrational, electron kinetics in nozzle expansion. *Journal of Thermophysics and Heat Transfer*, 15(3):308–316, July 2001.

[200] G Colonna and M Capitelli. The influence of atomic and molecular metastable states in high-enthalpy nozzle expansion nitrogen flows. *Journal of Physics D: Applied Physics*, 34(12):1812, 2001.

[201] A. D'Angola, G. Coppa, M. Capitelli, C. Gorse, and G. Colonna. *Computer Physics Communications*, 181(7):1204 – 1211, 2010.

[202] A Lo, A Cessou, P Boubert, and P Vervisch. Space and time analysis of the nanosecond scale discharges in atmospheric pressure air: I. gas temperature and vibrational distribution function of N$_2$ and O$_2$. *Journal of Physics D: Applied Physics*, 47(11):115201, 2014.

[203] Igor V Adamovich and Walter R Lempert. Challenges in understanding and predictive model development of plasma-assisted combustion. *Plasma Physics and Controlled Fusion*, 57(1):014001, 2015.

V. Laporta

Collisions entre électrons et molécules : Mécanismes réactionnels, modèles théoriques et applications aux plasmas hors-équilibre

Le 'fil rouge' qui a caractérisé la plupart de ma carrière scientifique a été la détermination des sections efficaces. Le calcul et la mesure d'une section efficace permettent de connaitre en détail la dynamique d'un processus et, en même temps, d'analyser les forces qui interviennent, et donc de tester une théorie physique. Ce mémoire d'HDR porte sur les travaux que j'ai mené pendant les dernières années, dédiés à la dynamique quantique moléculaire *ab initio*. Ces travaux sont concentrés sur les études théoriques des processus élémentaires pour les collisions réactives à impact électronique impliquant des molécules et des ions excités vibrationnellement et rotationellement, résolus sur les états moleculaires internes. En particulier, mon travail consiste dans le calcul des sections efficaces et des coefficients de vitesse correspondant à l'excitation vibrationnelle, l'attachement dissociatif électronique, la recombinaison dissociative et l'excitation dissociative. Les résultats ont été obtenus en utilisant les codes de chimie quantique ab initio MOLPRO et UK-R-Matrix, dans les approches théoriques du modèle du potentiel complexe local, l'approximation nucléaire adiabatique et la théorie du défaut quantique.

Ces résultats représentent les données d'entre pour la construction des modèles cinétiques collisionnels-radiatifs pour les plasmas moléculaires froids, 'hors-équilibre', où les dégrés internes des molécules, et souvent même les électrons, ne suivent pas la distribution de Maxwell-Boltzmann et il est, donc, indispensable d'étudier les propriétés thermodynamiques dans une approche dit 'état-par-état'.

Les applications de ces modèles sont très vastes : ils vont de l'astrochimie - la modélisation du milieu interstellaire et la formation des proto-étoiles - à l'ingénierie aérospatiale - la modélisation des flux hypersoniques et de l'onde de choc qui arrivent à la rentrée des navettes aérospatiales dans les atmosphères planétaires - et à l'énergétique - la modélisation du plasma dans les réacteurs à fusion magnétique contrôlée ou les procédés de combustion assistés par les plasmas.